

2014

Magneto-Optics and Magneto-Transport Studies on Thin Films for Sensor Applications

Kaida Yang

College of William & Mary - Arts & Sciences

Follow this and additional works at: <https://scholarworks.wm.edu/etd>



Part of the [Condensed Matter Physics Commons](#), and the [Materials Science and Engineering Commons](#)

Recommended Citation

Yang, Kaida, "Magneto-Optics and Magneto-Transport Studies on Thin Films for Sensor Applications" (2014). *Dissertations, Theses, and Masters Projects*. Paper 1539623368.
<https://dx.doi.org/doi:10.21220/s2-sey5-vt76>

This Dissertation is brought to you for free and open access by the Theses, Dissertations, & Master Projects at W&M ScholarWorks. It has been accepted for inclusion in Dissertations, Theses, and Masters Projects by an authorized administrator of W&M ScholarWorks. For more information, please contact scholarworks@wm.edu.

**Magneto-Optics and Magneto-Transport Studies
on Thin Films for Sensor Applications**

Kaida Yang

Shanghai, China

Master of Science, the College of William and Mary, 2010

Bachelor of Science, Fudan University, 2007

**A Dissertation presented to the Graduate Faculty
of the College of William and Mary in Candidacy for the Degree of
Doctor of Philosophy**

Department of Applied Science

**The College of William and Mary
May 2014**

©2014
Kaida Yang
All rights reserved.

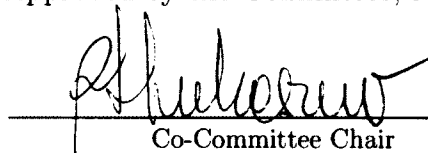
APPROVAL PAGE

This Dissertation is submitted in partial fulfillment of
the requirements for the degree of

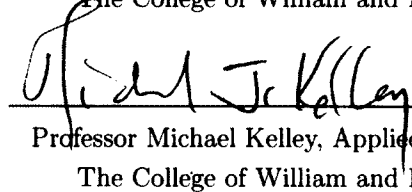
Doctor of Philosophy

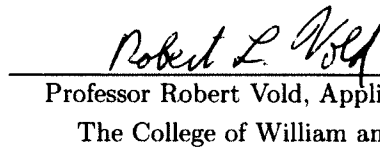

Kaida Yang

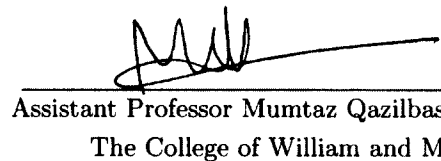
Approved by the Committee, May 2014


Co-Committee Chair

VMEC Distinguished Professor of Physics Rosa A. Lukaszew, Physics
The College of William and Mary


Professor Michael Kelley, Applied Science
The College of William and Mary


Professor Robert Vold, Applied Science
The College of William and Mary


Assistant Professor Mumtaz Qazilbash, Physics
The College of William and Mary

ABSTRACT

Recent progress and interest have brought considerable effort to bear on the synthesis and opportunities of magnetic thin films in different fields. There are applications in many fields, including remote sensing, waveguide applications, hard drive applications, etc. At the College of William and Mary, we have focused on utilizing magnetic thin films in some of these applications and are deeply involved in the optimization process of the thin films.

TABLE OF CONTENTS

Acknowledgments	iv
Dedication	v
List of Tables	vi
List of Figures	vii
CHAPTER	
1 Introduction	2
1.1 Magnetic Properties	2
1.1.1 Magnetic Hysteresis	2
1.1.2 Magnetic-Transport	6
1.2 Applications	9
1.2.1 Spin valves	9
1.2.2 Tunnel Magnetoresistance (TMR) and Magnetic Tunnel Junctions (MTJs)	11
1.2.3 GMR/TMR Magnetic Hysteresis	12
1.3 Magneto-Optical Properties	13
1.3.1 Macroscopic Formalism for Magnetic Multilayers	14
2 Surface Plasmons	17
2.1 Introduction	17
2.2 SPP at Planar Metal Surfaces	18
2.2.1 Total Internal Reflection	18
2.2.2 SPP Excitations	20

2.3	Diffraction Gratings	23
2.4	Applications	26
2.5	Transfer Matrix Formalism	26
2.5.1	Polarized-Dependent Optical Parameters-Transmission and Reflection Coefficients	29
2.5.2	Generalized Ellipsometric Parameters	29
3	Experimental Techniques	32
3.1	Deposition and Fabrication Techniques	32
3.1.1	Direct Current (DC) Magnetron Sputter Deposition	33
3.1.2	Deposition Chambers	34
3.2	Characterization Techniques	35
3.3	Angular-Dependent Surface Plasmon Resonance and MOKE Setup	37
3.3.1	Electromagnet	37
3.3.2	Sample and Sample Stage	41
3.3.3	Incident Arm and Optics	41
3.3.4	Reflected Arm and Optics	42
3.4	MOKE Experimental Setup	42
3.5	Electrical Transport Measurement	44
3.5.1	Four-Point Probe	44
3.5.2	Precision Current Source/Nanovolt Meter Setup and Control	45
4	Magnetic Field Modulation of Intense Surface Plasmon Polaritons on Au/Co/Au Multilayer Thin Films	49
4.1	Introduction	49
4.2	Experimental	52
4.3	Results and discussion	54
4.4	Conclusions	65

5	Magneto-Optics and Magneto-Plasmonics on Au-Co Nanocomposite Thin Films	66
5.1	Introduction	66
5.2	Experiment	68
5.3	Results and Discussion	70
5.3.1	Morphology and Microstructure	70
5.3.2	Optical and Magneto-Optical Characterization	73
5.4	Conclusions	79
6	Magneto-Transport and Non-Linear Magneto-Optics Correlations . . .	81
6.1	Introduction	81
6.2	Experiments	82
6.2.1	Deposition Conditions	82
6.2.2	Crystallinity Analysis—X-Ray Diffraction Measurement . .	83
6.2.3	Magnetic Hysteresis Measurements	87
6.2.4	Magneto-Transport Measurements	87
6.2.5	Non-Linear Magneto-Optical (NOMOKE) Measurement . .	89
6.3	Discussion	92
6.4	Conclusion	95
7	Magnetic Sensor Applications	97
7.1	Co/Pd Ultrathin Multilayer	97
7.1.1	Experiments and Methods	99
7.1.2	Results	100
7.1.3	Conclusion	106
8	Conclusion	107
	Bibliography	109
	Vita	122

ACKNOWLEDGMENTS

I would like to take this opportunity to express my thanks to those who helped me with various aspects of conducting research and the writing of this thesis. First and foremost, Dr. Ale Lukaszew for her guidance, patience and support throughout this research and the writing of this thesis. Her insights and words of encouragement have often inspired me and renewed my hopes for completing my graduate education. This work would not have been possible without the close guidance of Dr. Lukaszew. Her patience and unfailing love for science have forged me into a scientist. Dr. Lukaszew's mentorship and friendship are remembered. I would also like to thank my committee members for their efforts and contributions to this work: Dr. Cesar Clavero and Dr. Jonathan Skuza. I would additionally like to thank Dr. Clavero for his guidance throughout the initial stages of my graduate research.

I present this thesis in honor of my parents, for their love, support and encouragement.

LIST OF TABLES

7.1	RMS roughness analysis of buffer/seed layer Ru (5 nm)/Ta (3 nm)/Si.	100
7.2	RMS roughness analysis of [Co (0.2 nm)/Pd (0.2 nm)] _n	102

LIST OF FIGURES

1.1	Ferromagnetic thin film hysteresis or M-H loop (red solid line) with the initial induction curve (red dashed line). The important loop parameters are denoted, such as the saturation magnetization M_s , remanent magnetization M_r , coercive field H_c and saturation field H_s . [1]	3
1.2	An illustration of a single domain uniaxial magnet subject to an external magnetic field.	4
1.3	An illustration of GMR structure, two ferromagnetic layers separated by a non-magnetic metal layer. The resistance of the sandwich structure depends on the relative magnetization orientation of the two ferromagnetic layers. The resistance is measured with the current perpendicular to the plane.	7
1.4	Illustration of GMR effect	8
1.5	Illustration of a spin valve device	10
1.6	Illustration of the three MOKE configurations; Left: Longitudinal; Center: Polar; Right: Transverse. The magnetization orientation is shown in the corresponding case.	16
2.1	Light beam incident on a prism (inset: Intensity of the reflected light as a function of incident angle θ)	19
2.2	Light beam incident on a prism attached to metal thin film (e.g. Ag) —Krestschmann configuration	20
2.3	Light beam incident on a prism set in close proximity to an metal thin film (e.g. Ag) —Otto Configuration	20
2.4	Intensity of reflected light as a function of incident angle	21

2.5	SPP dispersion relationship[2]	22
2.6	Electric field profiles under the SPP excitation condition in a Kretschmann configuration shown in the inset.[2]	23
2.7	Light incident in a 1D metallic grating	24
2.8	Dispersion relationship of SPP excitation by the grating	25
2.9	Incident, reflected, and transmitted p and s modes of a plane wave with their wave vectors \mathbf{k}_a , \mathbf{k}'_a , \mathbf{k}_f and \mathbf{k}'_f , respectively. D_s and D_p indicate the modes of the back-travelling waves inside the substrate. If the exit medium is anisotropic, there may exist four different wave \mathbf{k}_f	27
3.1	Illustration of DC sputtering	34
3.2	Picture of Perkin-Elmer deposition system	35
3.3	Image of Angular-Dependent Surface Plasmon Resonance and MOKE setup	38
3.4	Configuration of Angular-Dependent Surface Plasmon Resonance and MOKE	39
3.5	Configuration of Angular-Dependent Surface Plasmon Resonance and MOKE-sample part	40
3.6	Schematic of MOKE setup used for measuring the magnetic hysteresis loop of thin films	43
3.7	Illustration of the four-point probe	45
3.8	Image of the four-point probe (top view)	46
3.9	Image of the four-point probe (side view)	46
3.10	Image of Keithley 6220 Precision Current Source and 2182A Nanovolt Meter	47

4.1	(a) Schematic view of momentum matching in the Kretschmann configuration, where far-field radiation couples symmetric leaky SPP modes at the air-metal interface by means of a glass prism. H_y represents the only magnetic component in the TM mode. (b) Dispersion relation for such modes in Co and Au films considering their absorption losses. The dashed line shows the dispersion relation for Au considering no absorption losses. The dispersion relation of Co splits into two branches when external magnetic fields are applied along the y direction.	52
4.2	Schematic view of the SPP excitation in the Kretschmann configuration for the Au(3nm)/Co(dCo)/Au(dAu) trilayers where external magnetic field H_{ext} is applied along y. (a) Reflectivity curves calculated for Co and Au films with critical thickness, (b) SPPs $ H_y $ at the metal-air interface for Co and Au films as a function of the thickness and (c) Transverse magneto-optical Kerr effect R for a single Co film and for Au(3nm)/Co(dCo)/Au(20 nm) trilayers as a function of the Co thickness. The lower row represents calculations of (d) R_{min} , (e) $ H_y _{max}$ and (f) ΔR_{max} for any combination of Au and Co thickness in the Au(3nm)/Co(dCo)/Au(dAu) trilayers.	56
4.3	(a) Experimental and (b) simulated angular dependency of the reflectivity with no external magnetic field applied R_{pp} for the Au(3 nm)/Co(dCo)/Au(20 nm) trilayers with dCo ranging from 2.5 to 10 nm. (c) Real (n) and imaginary (k) parts of the complex refractive index of Co film measured with ellipsometry.	57
4.4	(a) Transverse magneto-optical Kerr effect $\Delta R = R(+H) - R(-H)$ measured in the Kretschmann configuration for the Au(3 nm)/Co(d)/Au (20 nm) trilayers with d ranging from 2.5 to 10 nm. (b) Field dependent variation of the SPP wave vector $\Delta k_{sp} = k_{sp}(+H) - k_{sp}(-H)$. The dashed line represents the energy of the radiation used in the measurements $E=1.96$ eV.	59
4.5	Angular dependence of the relative variation in reflectivity $\Delta R_{pp}/R_{pp}$ for the Au(3 nm)/Co(d)/Au(20 nm) trilayers with d ranging from 2.5 to 10 nm. A maximum value of $\Delta R_{pp}/R_{pp} \sim 3.2$ (relative variation of 320%) is found for the trilayer with $d=2.8$ nm.	60

4.6	Variation with the incidence angle of the reflectivity (left column) and MO response (right column) for the Au/Co/Au trilayers with Co positioned at 3 nm (up), 11.5 nm (middle) and 23 nm (down) to the upper air-Au interface using (a) p-polarized light, (b) light rotated 45° from the s (and p) axis and a polarization analyzer oriented at 45° , (c) same as (b) but inserting a quarter wave plate with its fast axis along p and (d) using s-polarized light.	63
4.7	(a) Modulus of the product of the TM electric components $E_x E_z$ normalized to the incident intensity at the position in which the ferromagnetic film is placed in each case for the Au/Co/Au trilayers with Co positioned at 3 nm (up), 11.5 nm (middle) and 23 nm (down) to the upper Au-air interface. The dashed line represents the estimated value of $E_x E_z$ at the air-metal interface. (b) $E_x E_z$ is represented as a function of incidence angle and distance to the upper Au-air interface.	64
5.1	Illustration for Au:Co co-deposition	69
5.2	SEM image for 50 nm thick Co:Au films with a concentration ratio of 50:50 and grown at RT, 300°C and 600°C respectively. This work was carried out at ORNL by our collaborator M. Varela.	71
5.3	STEM Z-contrast images, EEL spectra and Co composition maps based on EELS/STEM (insets) for two nano-composite samples. (a) Sample grown at 300 °C with Co 5% Au 95% and EELS spectrum. The white rectangle shows the region where an EELS spectrum image of 71 x 12 pixels in size was acquired. Inset: STEM Co compositional map. (b) STEM Z-contrast image of the sample grown at 600 °C with Co 40% Au 60% and EELS spectrum. The white rectangle shows the region where an EELS spectrum image of 80 x 20 pixels in size was acquired. Inset: Co compositional map. The right panels show single pixel EEL spectra corresponding to the Co $L_{2,3}$ edge after background subtraction for both samples (the acquisition time was 1 s per pixel). PCA was applied to remove random noise to the spectrum image in (a). The Co maps were obtained through spectrum imaging after subtracting the background using a power law fit and integrating a window 20 eV wide below the Co $L_{2,3}$ edge around 779 eV. Note: The grayscales on both Co maps are not the same.	72

5.4	Optical constants (left column: n , right column: k) for Co:Au nano-composite films with composition ratio of (a) 10:90, (b) 30:70 and (c) 50:50. The optical constants of bulk Co and Au are plotted for comparison, along with the optical constants for nano-composite films with identical concentrations calculated using Maxwell-Garnett and Bruggeman effective medium approximations.	75
5.5	Angular dependence of the reflectivity in the Kretschmann configuration for Co-Au nano-composite films grown at RT, 300°C and 600°C with concentration ratios of (a) 10:90, (b) 30:70 and (c) 50:50. Experimental data are shown in the left column whereas simulations are shown in the right column.	77
5.6	Angular dependence of the Magneto-Optical Kerr Effect in the transversal configuration Eq.5.3 $\Delta R = R(H^+) - R(H^-)$ for (a) Co:Au nano-composite films with concentration ratio of 10:90 and grown at different temperatures and (b) nano-composite films grown at 300 °C with different Co concentrations.	78
6.1	Theta-2Theta XRD scans on composite Au-Co thin films with varied Co:Au composition; Top: Co 10% Au 90%; Center: Co 30% Au 70%; Bottom: Co 50% Au 50%	84
6.2	Lattice constant and domain size analysis on composite Au-Co thin films	86
6.3	Hysteresis loops obtained using SQUID magnetometry for selected nanocomposite films with different Co concentration and deposition temperatures; Top: Room Temperature; Center: 300°C ; Bottom: 600°C	88
6.4	RT magneto-resistance data vs applied magnetic field for nanocomposite thin films with the composition indicated	89
6.5	SHG magnetic hysteresis loop as a function of Co concentration	90
6.6	The corresponding saturation magnetization obtained from the magnetic hysteresis loops as a function of Co content.	91

6.7	SHG Magnetic contrast (top); magnetoresistance (bottom) vs Co content. The dashed line indicates that the local maximum in NOMOKE correlates well with the GMR maximum. Inset. SHG hysteresis loops for selected samples	93
6.8	Similar results to those in Fig.6.7 previously reported for Co-Ag granular thin films in Ref.[3]	94
7.1	Thin film structure of $[\text{Co/Pd}]_n$ multilayer on Ru 5 nm/Ta 3 nm buffer/seed layer.	99
7.2	AFM images of annealing treatment effects on the buffer layer: (a) Ta 3 nm on Si, (b) annealing Ta 3 nm at 300°C for 30 min, (c) Ru 5 nm on annealed Ta 3 nm.	101
7.3	Magnetic hysteresis measurement of $[\text{Co} (0.2 \text{ nm})/\text{Pd} (0.2 \text{ nm})]_{20}$ on Ru (5 nm) /Ta (3 nm)/Si sample with in-plane and out of plane configuration.	104
7.4	Magnetic hysteresis measurement of $[\text{Co} (0.4 \text{ nm})/\text{Pd} (0.4 \text{ nm})]_{10}$ on Ru (5 nm) /Ta (3 nm)/Si sample with in-plane and out of plane configuration.	105

MAGNETO-OPTICS AND MAGNETO-TRANSPORT STUDIES ON THIN
FILMS FOR SENSOR APPLICATIONS

CHAPTER 1

Introduction

This thesis focuses on nanostructured materials for novel magnetic sensors. In what follows, concepts and hypotheses which were used throughout the project are expanded and magnetic, optical, magneto-optical and magneto-transport properties and possible techniques to test them are covered as needed for the applications discussed.

1.1 Magnetic Properties

1.1.1 Magnetic Hysteresis

One of the most common and important measurements for virtually any magnetic device is a hysteresis measurement. A hysteresis measurement is a measurement of the magnetization response to the applied magnetic field, or so-called “M-H” loop measurement, where M represents the magnetization and H represents the applied magnetic field.

For a hysteresis measurement, different directions of the applied magnetic field may yield different magnetization properties. The Stoner-Wohlfarth model is often

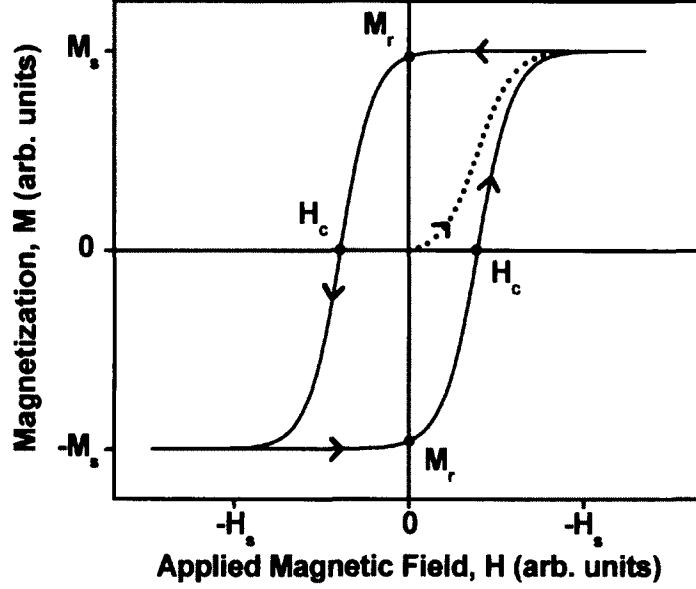


FIG. 1.1: Ferromagnetic thin film hysteresis or M-H loop (red solid line) with the initial induction curve (red dashed line). The important loop parameters are denoted, such as the saturation magnetization M_s , remanent magnetization M_r , coercive field H_c and saturation field H_s . [1]

used to describe a single-domain uniaxial magnet with an anisotropy energy parameter K_u and a volume V . When the magnetic field is applied at an angle θ to the easy axis direction while the magnetization is at an angle ϕ to the easy axis as shown in Fig.1.2, the total magnetic energy is:

$$E = -K_u V \cos^2 \phi - \mu_0 M H V \cos(\theta - \phi) \quad (1.1)$$

The magnetization angle ϕ should be obtained by minimizing the energy expression in Eq.1.1, namely:

$$\frac{\partial E}{\partial \phi} = K_u V \sin 2\phi + \mu_0 M H V \sin(\phi - \theta) = 0 \quad (1.2)$$

$$\frac{\partial^2 E}{\partial \phi^2} = 2K_u V \cos 2\phi + \mu_0 M H V \cos(\phi - \theta) > 0 \quad (1.3)$$

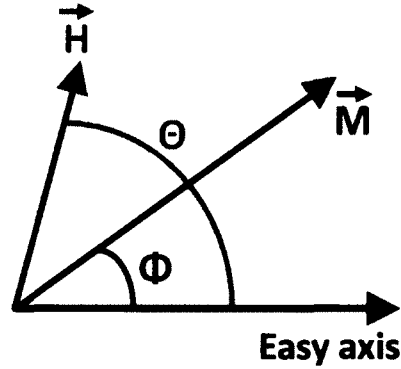


FIG. 1.2: An illustration of a single domain uniaxial magnet subject to an external magnetic field.

From Eq.1.2, it is easy to see that when the applied field is small $H \rightarrow 0$, the magnetization direction will be along the easy axis direction since $\sin 2\theta$ should be zero. And when the applied field is large, the magnetization direction will be along the applied field direction since $\sin(\phi - \theta)$ should be zero. There are two special situations: $\theta = 0$ and $\theta = \pi/2$, where the former is called the “easy axis loop” and the latter the “hard axis loop”. For $\theta = 0$, the solution for ϕ is:

$$\phi = \begin{cases} 0 & \text{if } H > \frac{2K_u}{\mu_0 M}, & (1.4a) \\ 0 \text{ or } \pi & \text{if } -\frac{2K_u}{\mu_0 M} \leq H \leq \frac{2K_u}{\mu_0 M}, & (1.4b) \\ \pi & \text{if } H < -\frac{2K_u}{\mu_0 M} & (1.4c) \end{cases}$$

the magnetization direction will always be along the easy axis direction. The region where ϕ has two stable values is called the “bi-stable” region due to the fact that the magnetization is stable in both directions along the easy axis. The actual magnetization direction depends on the history. The magnetization will keep the same direction as that when it enters the “bi-stable” region in the absence of noise or thermal fluctuation. Sweeping a magnetic field from a larger value to a smaller value is called a “sweep down” and sweeping magnetic field from a smaller value to

a larger value a “sweep up”. Therefore, if one starts with a large enough positive field, such that the magnetization direction is alined at $\phi = 0$, and sweep down the magnetic field to negative field, the magnetization will change direction to $\phi = \pi$ at $H_{0 \rightarrow \pi} = -\frac{2K_u}{\mu_0 M}$. Then if one sweeps the magnetic field up to a large positive field, the magnetization will change direction back to $\phi = 0$ at $H_{\pi \rightarrow 0} = \frac{2K_u}{\mu_0 M}$. Therefore, the “M-H” curve would look like two step functions at two different fields ($H_{0 \rightarrow \pi}$ and $H_{\pi \rightarrow 0}$). The coercive field is defined as half the value of the difference between the two switching fields, i.e. $H_c = \frac{1}{2} |H_{\pi \rightarrow 0} - H_{-0 \rightarrow \pi}|$. In the case of uniaxial anisotropy single-domain magnetization, $H_c = \frac{2K_u}{\mu_0 M}$.

One thing worth noting is the difference between the anisotropy field H_k and the coercive field H_c . The anisotropy field H_k comes from the anisotropy energy E_k , i.e. $H_k = \frac{\partial E_k}{\partial M}$, whereas the coercive field H_c is a measured value and often changes with temperature and the shape and microstructure of the sample. When no other effects are considered, the value of the coercive field is equal to the anisotropy field. However, in room temperature measurements, these two values are not equal since thermal fluctuations, etc. will influence the measured coercive field.

For $\theta = \frac{\pi}{2}$, the solution for ϕ becomes:

$$\phi = \begin{cases} \frac{\pi}{2} & \text{if } H > \frac{2K_u}{\mu_0 M}, \\ \sin^{-1} \left(\frac{\mu_0 M H}{2K_u} \right) & \text{if } -\frac{2K_u}{\mu_0 M} \leq H \leq \frac{2K_u}{\mu_0 M}, \\ -\frac{\pi}{2} & \text{if } H < -\frac{2K_u}{\mu_0 M} \end{cases} \quad (1.5a)$$

$$\text{if } -\frac{2K_u}{\mu_0 M} \leq H \leq \frac{2K_u}{\mu_0 M}, \quad (1.5b)$$

$$\text{if } H < -\frac{2K_u}{\mu_0 M} \quad (1.5c)$$

One can still get the anisotropy field value by sweeping the field and determining when the magnetization direction aligns with the field direction (i.e. when $H = H_k$).

1.1.2 Magnetic-Transport

An electron has an intrinsic spin of $1/2$. Therefore a flow of electrons is not only a flow of charges, i.e. a charge current, but also a possible flow of spin angular momentum, i.e. a spin current, if the electrons have a predominant spin direction. When magnetic moments interact with magnetic materials, especially ferromagnets, spin alignment gives rise to their magnetization.

Giant Magnetoresistance

The discovery of Giant Magnetoresistance (GMR) marks the birth of spintronics. It was discovered independently by Albert Fert's group [4] from Université Paris-Sud and Peter Gruber [5] from Festkörperforschung Jülich. The Nobel Prize in Physics in 2007 was granted to both for the discovery of GMR.

In the GMR effect, two ferromagnetic layers are separated by a non-magnetic metal layer as shown in Figure 1.3. The resistance reaches its maximum value when the magnetization directions in two separated ferromagnetic layers are aligned antiparallel (AP) with each other, while it reaches its minimum value when the two magnetization directions are parallel (P). The MR ratio can be defined as:

$$MR = \frac{R_{AP} - R_P}{R_P} \quad (1.6)$$

where R_{AP} is the resistance for the AP configuration and R_P is the resistance for the P configuration.

The resistance of the GMR structure can be measured with current both in the layer plane and perpendicular to the plane. GMR can be observed in both configurations. Figure 1.3 shows the resistance measured with current perpendicular to plane (CPP) geometry. The CPP configuration generally has a higher MR ratio than that of the current-in-plane configuration and therefore is more commonly used

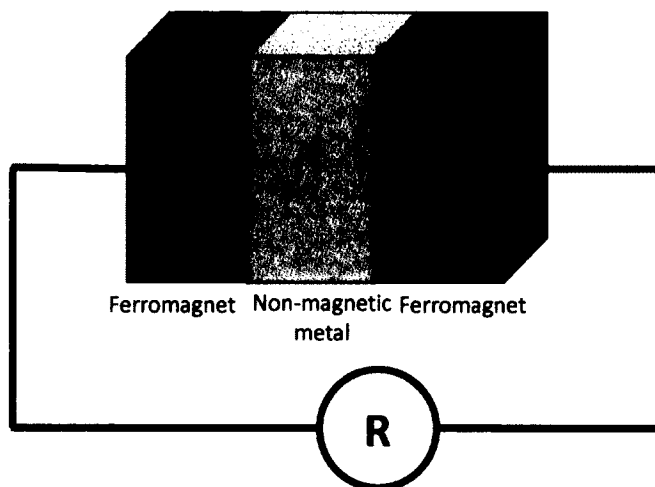


FIG. 1.3: An illustration of GMR structure, two ferromagnetic layers separated by a non-magnetic metal layer. The resistance of the sandwich structure depends on the relative magnetization orientation of the two ferromagnetic layers. The resistance is measured with the current perpendicular to the plane.

for GMR devices. For typical GMR structures, the MR ratio ranges from 1-80% at low temperature.

A two-channel conduction model can be used to understand the GMR effect.[6] In ferromagnetic conductors, the energy bands for itinerant electrons with spin directions parallel and anti-parallel with the magnetization directions are different. The electrons with magnetic moments aligned parallel with the magnetization are called "majority electrons" due to the fact that there are more of this kind of electrons than the "minority electrons", whose magnetic moments are aligned anti-parallel with the magnetization directions. As a result, after passing through a ferromagnetic layer, a "normal" electrical current, where the number of electron spins are the same for the two directions, becomes spin-polarized, where the majority of the electrons have magnetic moment directions the same as the magnetization direction of the ferromagnetic layer, as shown in Figure 1.4. When a current with the same amount of spin up and spin down go through the first ferromagnetic layer, there are more spin down than spin up electrons.

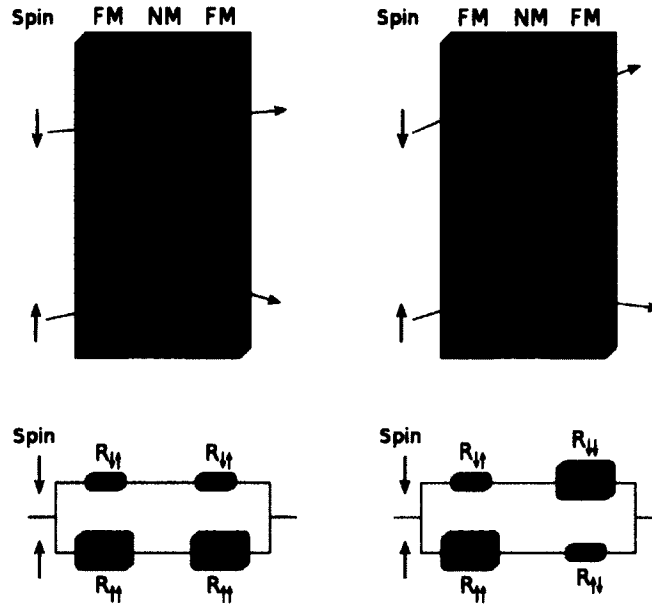


FIG. 1.4: Illustration of GMR effect

The spin-polarized electrons go through the non-magnetic layer as shown in Figure 1.3. The electrons scatter with the lattice with a length scale related to their mean free path, which induces resistivity. When electrons scatter in the non-magnetic layers, it turns out [6] that not all the scattering events influence the spin orientation, yet the electrons can lose or change their spin orientation by spin-orbit interaction, magnon and phonon scattering. The distance in which the electrons keep their original spin orientations is called the "spin-diffusion length", which is determined by the spin-orbit coupling, impurity spin flip scattering and the temperature of the material. In order to observe any spin-dependent phenomenon, the spin-diffusion length of the metal layer must generally be larger than the thickness of the layer[7][8].

For the second ferromagnetic layer, if its magnetization is aligned anti-parallel (AP) with the first layer magnetization, the majority electrons after passing through the first layer now become the minority electrons in the second layer. However, if the

second layer magnetization is aligned parallel (P) with the first layer magnetization, the majority electrons of the first layer are still the majority electrons in the second layer. Therefore more electrons will pass through the whole structure in the P configuration than the AP configuration. The resistivity in the P configuration is smaller than the AP configuration.

1.2 Applications

1.2.1 Spin valves

The "spin valve", a commonly used structure in spin-transfer phenomenon, is similar to the GMR structure previously discussed on Page 6. A spin valve structure consists of two ferromagnetic layers separated by a non-magnetic metal layer as shown in Figure 1.5. One of the ferromagnetic layers is designed to be switched by a magnetic field, spin-polarized current or other effects. This layer is called the "free layer". A typical free layer will have two preferred magnetization directions along its easy axis where the magnetic energy is a minimum.

The other ferromagnetic layer is the "reference layer". It is designed to maintain a fixed magnetization direction while the free layer magnetization changes. One way to achieve fixed magnetization for the reference layer is to make its anisotropy and coercivity much larger than those of the free layer. Therefore when switching is induced in the free layer, there are no changes to the reference layer magnetization. Another way to achieve a fixed magnetization for the reference layer is to incorporate the reference layer into an exchange bias system such that the coercivity of the reference layer magnetization is biased outside the range of the free layer magnetization coercivity.

Since the magnetization direction of the reference layer is fixed, any resistance

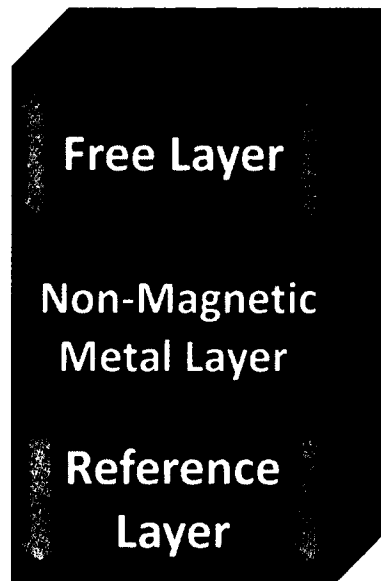


FIG. 1.5: Illustration of a spin valve device

change of the total system is due to the change of the free layer magnetization, measured through the GMR effect, when current is applied across the layers and the voltage is measured between the free and reference layer. By directly measuring the resistance of a spin valve, the free layer magnetization configuration can be fully understood, e.g. for a simple "two-state" spin valve, the resistance from a DC electrical measurement will indicate whether the free layer magnetization is parallel or anti-parallel to the reference layer magnetization. For a uniformly magnetized free layer, the resistance represents the angle between the free and reference layer magnetization.

The non-magnetic metal layer between the two ferromagnetic layers needs to have a long spin diffusion length, larger than the thickness of the layer, so that the spin-polarized current keeps its polarization between the reference and free layer. The typical thickness of the spacer is only several nanometers, and thus spin polarization loss can be ignored[9].

1.2.2 Tunnel Magnetoresistance (TMR) and Magnetic Tunnel Junctions (MTJs)

Tunnel Magnetoresistance (TMR) is found in magnetic tunnel junctions (MTJs), whose basic structures are similar to that of a spin valve. Instead of separating the free and reference layers by a non-magnetic metal layer, the MTJ uses a thin insulating layer. Electrons will tunnel through the insulating layer between the two ferromagnetic layers, where the rate of tunneling depends on the electron spin polarization and the magnetization directions of the ferromagnets. Therefore, similar to spin valves, as long as the magnetization of the reference layer of an MTJ remains unchanged during a stimulus, the reference layer can serve as a polarizer to the tunneling current and readout of the free layer magnetization[10].

TMR was discovered in 1975[11], much earlier than the GMR. However, it did not attract much attention at that time because the measurement was done at low temperature and the MR was small. A significant TMR at room temperature was later found for amorphous aluminum oxide barriers[12][13]. Nowadays, the most commonly used insulating barrier is crystalline MgO, theoretically predicted in 2001[14][15] to lead to larger TMR. Experiments[16][17][18] [19]then followed, where more than 200% TMRs was achieved at room temperature. A typical ferromagnetic material for the electrodes is CoFeB, and the overall amorphous CoFeB/MgO/CoFeB structure after deposition can achieve (001) crystal texture after annealing. Furthermore, the magnetic anisotropy at the CoFeB-MgO interface is found to be perpendicular. Therefore an all-perpendicular MTJ structure can be realized with thin CoFeB layers[20][21].

The TMR ratio has a simple relation with the spin polarizations inside the two ferromagnetic layers[11]:

$$\text{TMR} = \frac{2P_1 - P_2}{1 - P_1P(2)} \quad (1.7)$$

where P_1 and P_2 represent the spin polarization of the first and second ferromagnetic layers. For typical ferromagnetic materials, the spin polarizations are measured to be 44% for Fe, 34% for Co and 11% for Ni, which explains the TMR ratio between 10% to 50% from the early experiments[22].

1.2.3 GMR/TMR Magnetic Hysteresis

In a GMR/TMR system, there is often more than one magnetic layer. Each layer will respond to the applied magnetic field and the total magnetization configuration as well as the resistance of the system can have a complicated dependence on the applied field. In a simple two-layer system, there are two different types of hysteresis measurements for applying an easy axis magnetic field. One is called the “major-loop” where the range of the applied magnetic field is usually larger and both the free and reference layers will change their magnetization directions during the measurement. Typically the system will show the P state resistance for both positive and negative fields with large absolute values, corresponding to both the free and reference layers aligned with the applied magnetic field direction. For smaller absolute values of the applied field, there may be a region that shows the AP state resistance of the system due to the different coercivities between the free and reference layers.

The other easy axis hysteresis measurement is called a “minor loop”, corresponding to when the applied magnetic field range is chosen to only change the magnetization direction for one of the layers, i.e. the free layer, and leave the other layer, usually the reference layer, unchanged. In this case, the physics is the same as for the single magnetic layer system mentioned before. The reference layer can be used to determine the free layer magnetization response through the GMR/TMR effects.

1.3 Magneto-Optical Properties

Ferromagnetic materials also exhibit magneto-optical properties. The Magneto-Optical Kerr Effect (MOKE) describes the changes to light reflected from a magnetized surface, which can be used to extract the magnetization structure of the materials. MOKE was discovered by Kerr[23], who found a slight rotation (typically $\ll 1^\circ$) of the plane of polarization of a light beam reflects a magnetized surface. Both polarization and reflected intensity can be changed when light reflected from magnetized surface. This is similar to the Faraday Effect, where the polarization of a light beam is altered upon transmission through a magnetic material, while the Kerr Effect describes changes to the light reflected from a magnetic surface.

The plane-polarized light reflected from a magnetic film with non-zero magnetization \mathbf{M} will have its major axis polarization changed, where the rotation depends on the magnetization \mathbf{M} of the thin film sample relative to the plane of incidence of the light beam.

Some non-linear magneto-optical effects are associated with surfaces and interfaces in magnetic media, i.e. nonlinear second-harmonic Kerr Effects, have also been predicted and detected. Although second-harmonic generation is forbidden in materials with an inversion center, and most widely encountered materials (Fe, Co, Ni, FeNi, etc.) are such, space-inversion symmetry is broken at a surface or an interface. Time-reversal symmetry is also broken in magnets. The breaking of these symmetries leads to the appearance of second-harmonic magneto-optical phenomena, which have been found to significantly surpass the corresponding linear effects in magnitude. This thesis addresses such effects in nano-composite magnetic-non-magnetic thin films through a collaborative effort with Professor T. Murzina from Moscow State University.

1.3.1 Macroscopic Formalism for Magnetic Multilayers

The macroscopic description of the magneto-optical effect is based on an analysis of the dielectric properties of a medium[24]. Two circularly polarized modes gain different phase shifts due to their different propagating velocities when propagating through magnetic media, resulting in a rotation of the polarization plane, which induces the conventional Faraday rotation. Moreover, the different absorption rates of the medium for the two circularly polarized modes affects the ellipticity. In general, both effects exist in a magnetized medium.

A 3×3 dielectric tensor describes a magnetic medium, with $\epsilon_{i,j}$ with $i, j = 1, 2, 3$, and it can be decomposed into a symmetric part and an asymmetric part, $\epsilon_{i,j} = (\epsilon_{i,j} + \epsilon_{j,i})/2 + (\epsilon_{i,j} - \epsilon_{j,i})/2$. The symmetric part can be diagonalized by an appropriate rotation of the coordinate system, giving no contribution to the Faraday effect. The dielectric tensor is:

$$\tilde{\epsilon} = \epsilon \begin{pmatrix} 1 & iQ_z & -iQ_y \\ -iQ_z & 1 & iQ_x \\ iQ_y & -iQ_x & 1 \end{pmatrix} \quad (1.8)$$

Two normal modes for left-circularly polarized light with refraction index $\theta_L = n(1 - \frac{1}{2}\mathbf{Q} \cdot \hat{\mathbf{k}})$ and right-circularly polarized light with refraction index $\theta_L = n(1 + \frac{1}{2}\mathbf{Q} \cdot \hat{\mathbf{k}})$, where $n = \sqrt{\epsilon}$ is the average refraction index and \mathbf{Q} is the Voigt vector can be described.

Most magnetic materials strongly absorb light. This leads to a convenient way to experimentally measure the reflected light in order to probe the magneto-optic effect. For a given magnetic multilayer, the tensor for each layer can be expressed by a 3×3 matrix[25][26]. Considering a multilayer structure that consists of N individual layers, after multiple reflections, there will be a reflected beam

backscattered into the initial medium i and a transmitted beam that emerges from the bottom layer into the final medium f . The Kerr rotation ϕ' and ellipticity ϕ'' for s- and p-polarized light are given by

$$\phi_s = \phi'_s + i\phi''_s = \frac{r_{ps}}{r_{ss}} \quad (1.9)$$

and

$$\phi_p = \phi'_p + i\phi''_p = \frac{r_{sp}}{r_{pp}} \quad (1.10)$$

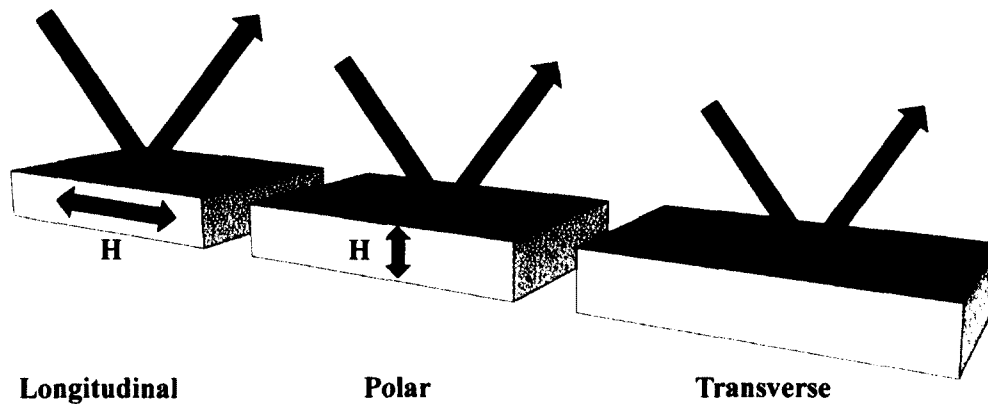
With the ultrathin films approximation where the optical thickness of the film is much less than the wavelength of the incident light, the reflection coefficients are[24]:

$$r_{ss} = \frac{n_i \cos\theta_i - n_f \cos\theta_f}{n_i \cos\theta_i + n_f \cos\theta_f} \quad (1.11)$$

$$r_{pp} = \frac{n_f \cos\theta_i - n_i \cos\theta_f}{n_f \cos\theta_i + n_i \cos\theta_f} \quad (1.12)$$

$$r_{ps} = -\frac{4\pi}{\lambda} \frac{n_i \cos\theta_i}{(n_i \cos\theta_i + n_f \cos\theta_f)(n_f \cos\theta_i + n_i \cos\theta_f)} \times \left(\cos\theta_f \sum_m d_m n_m^2 Q_z^{(m)} - n_f n_i \sin\theta_i \sum_m d_m Q_y^{(m)} \right) \quad (1.13)$$

$$r_{ps} = -\frac{4\pi}{\lambda} \frac{n_i \cos\theta_i}{(n_i \cos\theta_i + n_f \cos\theta_f)(n_f \cos\theta_i + n_i \cos\theta_f)} \times \left(\cos\theta_f \sum_m d_m n_m^2 Q_z^{(m)} + n_f n_i \sin\theta_i \sum_m d_m Q_y^{(m)} \right) \quad (1.14)$$



Longitudinal

Polar

Transverse

FIG. 1.6: Illustration of the three MOKE configurations; Left: Longitudinal; Center: Polar; Right: Transverse. The magnetization orientation is shown in the corresponding case.

CHAPTER 2

Surface Plasmons

2.1 Introduction

Surface plasmons are collective oscillations of free electrons localized at surfaces of metallic structures[27]. When surface plasmons are excited, fluctuations of the electric charge are induced, accompanied by electromagnetic oscillations[2]. Therefore, the surface plasmons are also called surface plasmon polaritons (SPPs), which represent coupled oscillations of electromagnetic waves and oscillations of charged particles[28][29].

SPPs are thus the coupled modes of surface plasmons and light[30]. The SPPs enhance the electromagnetic fields localized at the surface of metallic structures compared with the excitation field. The enhancement localization of the EM fields has led to many applications in the new field of "plasmonics". For example, the localization of the fields enables nano-optics beyond the diffraction limit of light waves[31].

2.2 SPP at Planar Metal Surfaces

In general, there are two different types of surface plasmons: those propagating along a planar dielectric–metal interface, which are usually called surface plasmon polaritons (SPPs)[28][2], and those localized at metallic nanoparticles[32], which is usually called localized surface plasmons (LSPs). SPPs and LSPs are of the same physical origin. Both of them exhibit electromagnetic fields localized at metallic surfaces and significantly enhanced with respect to the excitation fields. An optical method for exciting SPPs using a prism, called the attenuated total reflection (ATR) method, was demonstrated by Otto and also by Kretschmann and Raether[28] in 1968. In this chapter, we summarize the fundamental characteristics of SPPs.

2.2.1 Total Internal Reflection

A light beam is incident on a glass prism (e.g. triangular prism) surrounded by air, as shown in Fig.2.1. The dielectric constant of the prism is defined as ϵ_p and of the surrounding medium (air) as ϵ_m , with the condition $\epsilon_p > \epsilon_m$. Light incident at the boundary between two media as a function of incident angle θ follows the well-known phenomena of reflection and refraction. When the incident angle from denser media is larger than a certain angle, called the critical angle of total reflection, it is well-known that light is totally reflected at the interface between the denser and the lighter media. The critical angle of total reflection is defined as:

$$\theta_c = \arcsin \left(\frac{\sqrt{\epsilon_m}}{\sqrt{\epsilon_p}} \right) \quad (2.1)$$

Since metals are not perfect reflectors, evanescent waves are generated at the interface and penetrate into the medium. For the incident electric field to satisfy Maxwell's equations, $k^2 = k_x^2 + k_z^2 = (\omega/c)^2 \epsilon_p$ should hold.

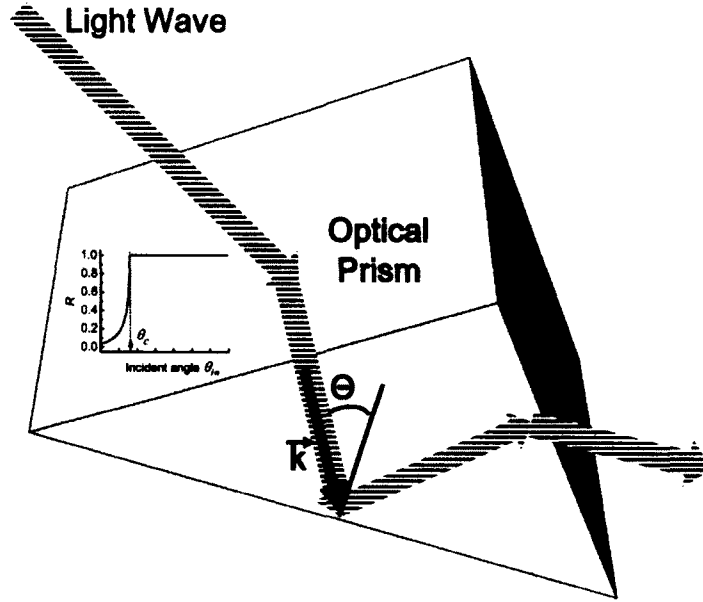


FIG. 2.1: Light beam incident on a prism (inset: Intensity of the reflected light as a function of incident angle θ)

The wavevector of the incident light is given by:

$$k_x = (\omega/c)\sqrt{\epsilon_p}\sin(\theta_{in}) \quad (2.2)$$

Under the condition of total reflection, the wavevector of the medium, $k_m^2 = k_{mx}^2 + k_{mz}^2 = (\omega/c)^2\epsilon_m$, should also hold. The boundary condition at the prism-medium interface requires continuity of the x-component of the wavevector, i.e. $k_{mx} = k_x = (\omega/c)\sqrt{\epsilon_p}\sin(\theta_{in})$. The electric field can be written as:

$$E_m = E_{m0}e^{i(k_{mx}x - \omega t)}e^{-\gamma z} \quad (2.3)$$

where $k_{mz} = i\gamma$.

This indicates that an evanescent wave propagates along the x-direction with its amplitude decaying exponentially away from the interface. Even if there is no energy flow into the adjacent medium, the evanescent electric fields penetrate into

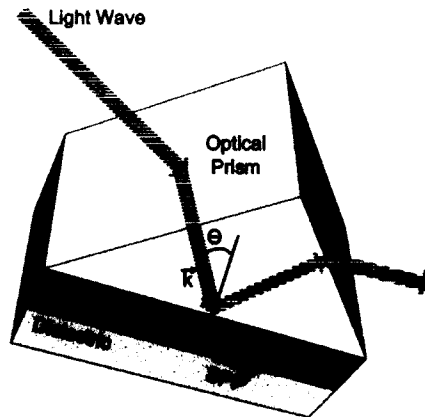


FIG. 2.2: Light beam incident on a prism attached to metal thin film (e.g. Ag) — Kretschmann configuration

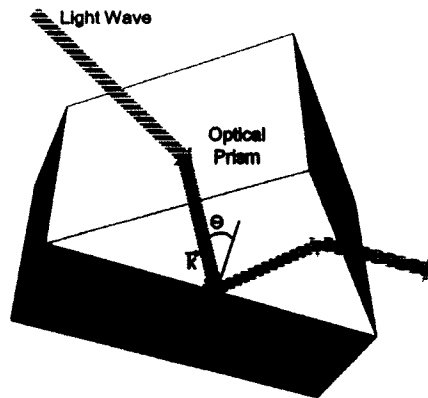


FIG. 2.3: Light beam incident on a prism set in close proximity to an metal thin film (e.g. Ag) — Otto Configuration

the medium and have nonzero amplitudes.

2.2.2 SPP Excitations

A prism is attached to metal thin films, as shown in Fig.2.2 in the Kretschmann configuration. The Otto configuration is shown in Fig.2.3

The intensity of the reflected light as a function of the incident angle leads to a dip in reflectivity due to light absorption at the angle which is larger than θ_c , as shown in Fig.2.4. The dip is attributed to the excitation of SPPs at the metal-air

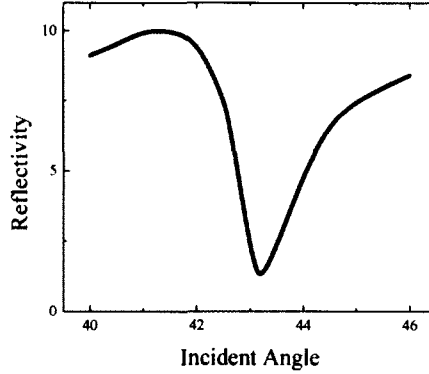


FIG. 2.4: Intensity of reflected light as a function of incident angle

interface.

The electric fields associated with the SPPs can be written as[28][29]:

$$E_j = (E_x^j, 0, E_z^j)e^{i(k_{SPP}x - \omega t)} e^{-\alpha_j|z|} \quad (2.4)$$

with $j = d$ for the dielectric and $j = m$ for the metal. The magnetic fields H_j are written in a similar way. Thus SPPs are classified as a transverse magnetic (TM) mode and can be excited only by p-polarized light.

The SPP dispersion relationship between k_{SPP} and ω is given by

$$k_{SPP} = \frac{\omega}{c} \sqrt{\frac{\epsilon(\omega)\epsilon_m}{\epsilon(\omega) + \epsilon_m}} \quad (2.5)$$

where $\epsilon(\omega)$ is the dielectric function of the metal.

In general, Eq.2.5 is valid for a material for which the real part of $\epsilon(\omega)$ takes negative values and the imaginary part is not very large. Thus, the condition is satisfied by good metals such as Ag and Au in the visible range.

A typical SPP dispersion relationship is schematically shown in Fig.2.5. The curve starts at $\omega = 0$ and $k_c = 0$ and approaches a horizontal line $\omega = \omega_{SP}$ for large k_x , where ω_{SP} is the frequency satisfying $\epsilon(\omega_{SP}) = -\epsilon_m$. For small k_x , the SPP

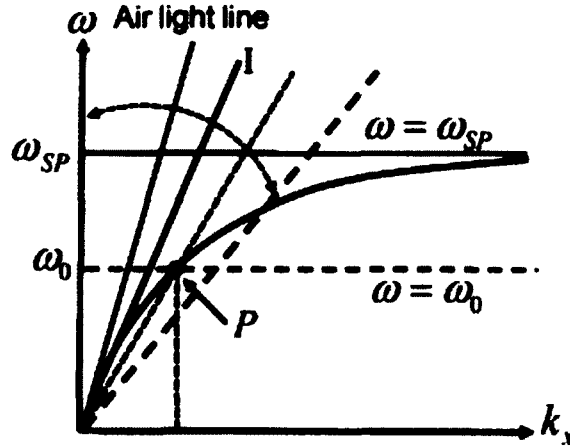


FIG. 2.5: SPP dispersion relationship[2]

dispersion curve approaches a line given by $k_x = (\omega/c)\sqrt{\epsilon_m}$. The SPP dispersion curve is located in the nonradiative region and SPPs can not interact directly with light propagating in air.

The dispersion curve of the evanescent wave generated from the prism is given by Eq.2.2 and represented by the solid line I in Fig.2.5. The slope of the line changes depending on θ_{in} . An evanescent wave generated by incident light with a frequency ω and an incident angle θ_{in} is characterized by a point P on I. The excitation of SPPs in the ATR configuration can be explained by the crossing of line I with the SPP dispersion curve.

As shown in Fig.2.6, the electric field localized in the vicinity of the metal surface and the electric field enhancement are the most important features of SPP excitation. In the figure, the square of the electric field amplitude $|E_{(z)}|^2$ is normalized to the incident light $|E_{(0)}|^2$, referred to as the electric field enhancement factor. The contributions of z- and x- components of the electric field to $|E_{(z)}|^2$ are shown by broken and dotted lines, respectively.

Fig.2.6 clearly shows that under SPP excitation condition, a very strong electric field, mainly normal to the interface (z-component), is generated at the metal-air

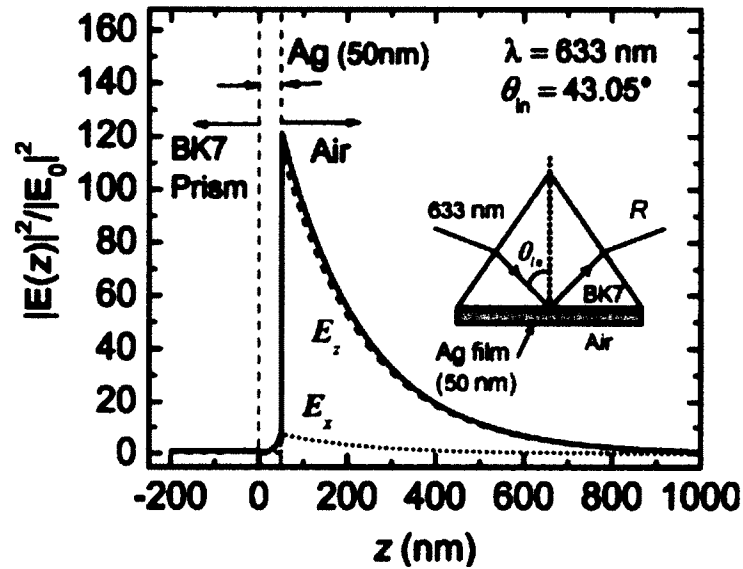


FIG. 2.6: Electric field profiles under the SPP excitation condition in a Kretschmann configuration shown in the inset.[2]

interface and decays exponentially away from the interface. The region of the strong electric field is confined to within a few hundred nanometers of the interface. The generation of the enhanced and localized electric fields in the vicinity of the metal surface offers the possibility of many potential applications.

2.3 Diffraction Gratings

The ATR configuration described in the previous sections can be used to excite SPPs, however it is sometimes difficult to miniaturize. An alternative technique is a grating coupler method, in which periodic structures are introduced on metal surfaces to diffract incident light into SPPs.

Fig.2.7 shows a metallic surface corrugated with periodic grooves, a one-dimensional (1D) grating, and monochromatic light incident on the surface at an angle θ_{in} . The grating induces diffracted light of various orders in addition to the reflected light. In optics, a diffraction grating is an optical component with a regular pattern, which

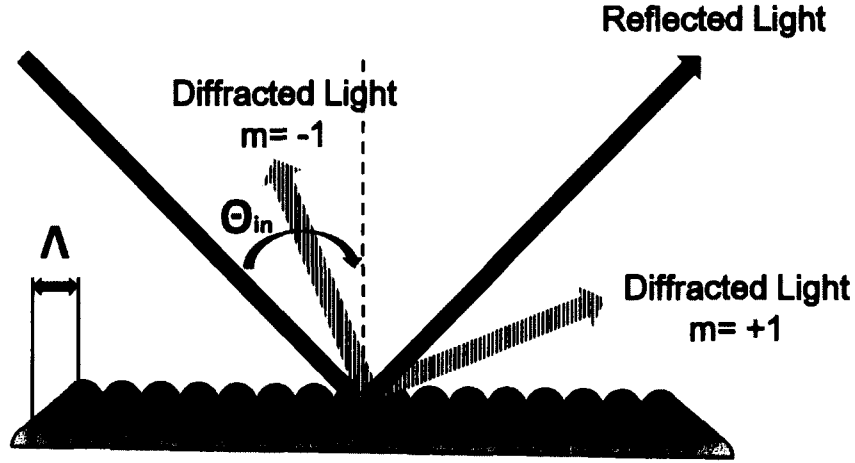


FIG. 2.7: Light incident in a 1D metallic grating

splits and diffracts light into several beams travelling in different directions. The directions of these beams depend on the spacing of the grating and the wavelength (λ) of the incident light. An idealized diffraction gratings is composed of parallel and infinitely long narrow slits of spacing Λ .

As shown in Fig.2.8, a reflection dip very similar to Fig.2.4 can be observed provided that the spacing between the grooves (grating pitch Λ) is appropriately chosen[33][34]. The dip appears for p-polarized incident light but not for s-polarized incident light. The dip can be attributed to the excitation of SPPs, and the energy of the incident light is transferred to SPPs at the dip angle angle.

The momentum of an optical wave can be increased to match that of surface plasma by gratings. The wavevector \mathbf{k} of the diffracted light parallel to the interface is altered as:

$$k_{\text{SPP}} = k_{x\text{in}} + \Delta k_x \quad (2.6)$$

with:

$$\Delta k_x = m \left(\frac{2\pi}{\Lambda} \right), m = \pm 1, \pm 2, \dots \quad (2.7)$$

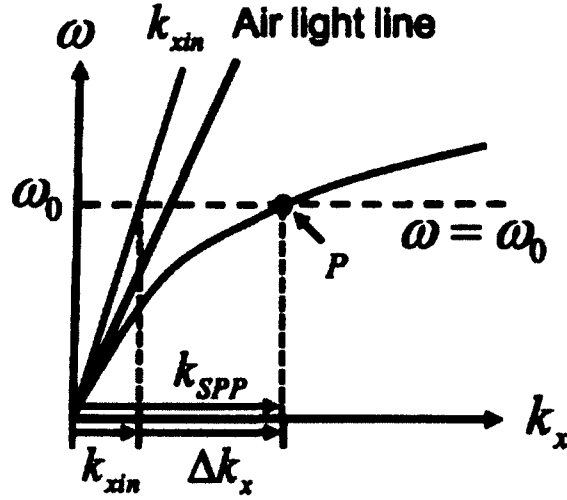


FIG. 2.8: Dispersion relationship of SPP excitation by the grating

and:

$$k_{xin} = (\omega/c) \sqrt{\epsilon_m} \sin\theta_{in} \quad (2.8)$$

where m is an interger and, k_x is the component of the wave vector of the incident light along the grating surface. Eq.2.6 represents the x-component of the wavevector of the m th order of diffracted light. Eq.2.6 implies that the excitation of SPPs is possible when the incident light is diffracted into SPPs. The grating can add a quasi-wavevector of $m\frac{2\pi}{\Lambda}$ to the incident light wavevector k_{xin} to be compatible with k_{SPP} , as shown in Fig.2.8

The relationship between m and the incident angle θ is:

$$n_a \sin\theta + m\frac{\lambda}{a} = \pm \sqrt{\frac{\epsilon_{mr} n_a^2}{\epsilon_{mr} + n_a^2}} \quad (2.9)$$

where θ is the angle of incident beam, n_a is refractive index of dielectric, and ϵ_{mr} is the real part of metal's dielectric constant. When the formula is satisfied, surface plasmon polaritons are excited.

2.4 Applications

Surface plasmons are essentially light waves trapped at the surface because of their interaction with the free electrons of the conductor. In this interaction, the free electrons respond collectively by oscillating in resonance with the light wave[28]. These evanescent waves excited at the boundary of the metal and the medium are very sensitive to any dielectric change at this boundary, such as the adsorption of molecules to the metal surface. Thus, optical sensors, based on SPPs at planar gold surfaces, are fast becoming a preferred method for many sensing applications. Biosensors based on surface plasmon resonance (SPR) possess desirable characteristics such as refractive index sensitivity on the order of one part in 10^5 – 10^6 corresponding to a real mass sensitivity in the picogram per square millimeter range, although for some biosensing applications—particularly biohazards and defense applications—this may not be sufficient[35]. The question that we have addressed in this work is whether or not it is possible to further enhance the sensitivity of SPR based biosensors.

2.5 Transfer Matrix Formalism

We use a general transfer matrix formalism to simulate ellipsometric properties using bulk values for the dielectric constants[36], which is useful to compare with experimental ellipsometric measurements.

For the general transfer matrix, considering a layered system with plane parallel interfaces, assume an incident light wave with wave vector \mathbf{k}_a coming from the incident medium (ambient, index a , $-\infty < z < \infty$, complex index of refraction n_a) at an angle of incidence Φ_a (Fig.2.9). Then the wave vector of the wave reflected from the plane of incidence will be \mathbf{k}'_a . Let A_p , A_s and B_p , B_s denote the complex

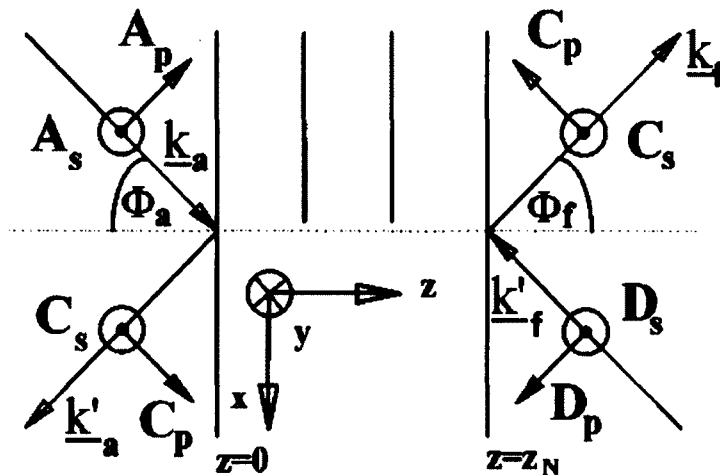


FIG. 2.9: Incident, reflected, and transmitted p and s modes of a plane wave with their wave vectors \mathbf{k}_a , \mathbf{k}'_a , \mathbf{k}_f and \mathbf{k}'_f , respectively. D_s and D_p indicate the modes of the back-travelling waves inside the substrate. If the exit medium is anisotropic, there may exist four different wave \mathbf{k}_f .

amplitudes of the p and s mode of the incident and reflected waves, respectively. The exit medium (substrate, index f , $Z_N < z < \infty$) does not include a back side. Hence there are only two amplitudes for the transmitted p and s mode, C_p and C_s , respectively. A Cartesian laboratory coordinate system is then defined when the plane of incidence coincides with the x - z plane, where the origin is set at the interface.

Without loss of generality the wave vector \mathbf{k}_a does not have a component parallel to the y -direction. In order to connect the four wave amplitudes inside the incident medium (left side of the structure in Fig.2.9) with the two transmitted amplitudes inside the exit medium (right side of Fig.2.9), a general transfer matrix can be defined for any given layered structure:

$$\begin{pmatrix} A_s \\ B_s \\ A_p \\ B_p \end{pmatrix} = \mathbf{T} \begin{pmatrix} C_s \\ D_s \\ C_p \\ D_p \end{pmatrix} = \begin{pmatrix} T_{11} & T_{12} & T_{13} & T_{14} \\ T_{21} & T_{22} & T_{23} & T_{24} \\ T_{31} & T_{32} & T_{33} & T_{34} \\ T_{41} & T_{42} & T_{43} & T_{44} \end{pmatrix} \begin{pmatrix} C_s \\ 0 \\ C_p \\ 0 \end{pmatrix} \quad (2.10)$$

The tangential components of the electric and magnetic field vectors are continuous across the interface between the two media (if the surface current density \mathbf{K} and the surface charge density σ vanish). Thus a 4×4 matrix algebra that describes the propagation of monochromatic plane waves through the entire layered system can be introduced. If d_i is the thickness of the i th layer, a partial transfer matrix \mathbf{T}_{ip} that connects the in-plane wave components at the interface at $z = z_i$ with those at the next interface at $z = z_i + d_i$ can be defined for both isotropic and anisotropic layers. Hence the ordered product of all partial matrices from all N layers transfer the in-plane components at the first interface at $z = 0$ to the last interface at $z = z_N$. Likewise, the incident matrix \mathbf{L}_a projects the in-plane wave components of the incident and reflected waves through to the first interface. The exit matrix \mathbf{L}_f projects the transmitted amplitudes from the last interface through to the exit medium that may be isotropic or anisotropic. The general transfer matrix \mathbf{T} as defined in Eq.2.10 is then most easily obtained from the product of all inverted matrices \mathbf{T}_{ip} for each layer, as well as the incident and exit matrices in the order of their appearance:

$$\mathbf{T} = \mathbf{L}_a^{-1} \prod_{i=1}^N [\mathbf{T}_{ip}(d_i)]^{-1} \mathbf{L}_f = \mathbf{L}_a^{-1} \prod_{i=1}^N \mathbf{T}_{ip}(-d_i) \mathbf{L}_f \quad (2.11)$$

Note that due to the symmetry of the coordinate systems the inversion of \mathbf{T}_p that is indicated in Eq.2.11 does not require a matrix inversion calculation.

2.5.1 Polarized-Dependent Optical Parameters-Transmission and Reflection Coefficients

The measurable polarization-dependent optical parameters can be obtained immediately from the general transfer matrix and therefore through the algebra discussed here.

The transmission and reflection coefficients of layered systems are traditionally defined as the ratios of the amplitudes of the incident and reflected or transmitted waves, respectively. They can be expressed in terms of the elements of the general transfer matrix \mathbf{T} . Consider Eq.2.10 as a system of four linear relations between the p and s components on the left and right sides of Fig.2.9. As an example, one might choose the Jones reflection and transmission coefficients r_{ss} and t_{sp} , respectively. Inside the substrate only transmitted waves are allowed. Therefore the ratios can be found as follows:

$$\begin{aligned} r_{ss} &= \left(\frac{B_s}{A_s} \right)_{A_p=0} = \frac{T_{21}T_{33} - T_{23}T_{31}}{T_{11}T_{33} - T_{13}T_{31}} \\ t_{sp} &= \left(\frac{C_p}{A_s} \right)_{A_p=0} = \frac{-T_{31}}{T_{11}T_{33} - T_{13}T_{31}} \end{aligned} \quad (2.12)$$

Note that all eight conceivable quotients of the incident and emerging wave parts can be expressed in terms of elements of the matrix \mathbf{T} .

2.5.2 Generalized Ellipsometric Parameters

The complex reflectance ratio ρ has been traditionally defined as

$$\rho \equiv \tan\Psi e^{i\Delta} \equiv \left(\frac{B_p}{A_p} \right) \left(\frac{B_s}{A_s} \right)^{-1} \quad (2.13)$$

and can be expressed through the ratios of the amplitudes of the incident and reflected waves. Let χ be the ratio of the incident modes A_p and A_s ; then the ellipsometric ratio is obtained from Eq.2.10 as follows:

$$\frac{1}{\rho} = \frac{1}{\chi} \frac{t_{41}(T_{33} - \chi T_{13}) + t_{43}(\chi T_{11} - T_{31})}{t_{21}(T_{33} - \chi T_{13}) + t_{23}(\chi T_{11} - T_{31})}, \chi \equiv \frac{A_p}{A_s} \quad (2.14)$$

or, using the expression for the transmission and reflection coefficients derived from **T**:

$$\rho = [r_{pp} + R_{rp}(\chi)^{-1}](r_{ss} + r_{ps}\chi)^{-1} \quad (2.15)$$

or, in a slightly different form:

$$\rho = \left[\frac{r_{pp}}{r_{ss}} + \frac{r_{sp}}{r_{ss}}(\chi)^{-1} \right] \left(1 + \frac{r_{pp} r_{ps}}{r_{ss} r_{pp}} \chi \right)^{-1} \quad (2.16)$$

As seen in the latter equation the complex reflectance ratio ρ is then a combination of three ratios formed by the elements of the Jones reflection matrix, and depends on the ratio of the incident wave amplitudes A_p and A_s . The basis of generalized ellipsometry is to define and determine three linear independent normalized reflection matrix elements.

Defining a set of those normalized elements:

$$\frac{r_{pp}}{r_{ss}} \equiv R_{pp}, \frac{r_{ps}}{r_{pp}} \equiv R_{ps}, \frac{r_{sp}}{r_{ss}} \equiv R_{sp}, \quad (2.17)$$

results in Eq.2.16:

$$\rho = [R_{pp} + R_{sp}](\chi)^{-1}(1 + R_{pp}R_{ps}\chi)^{-1} \quad (2.18)$$

Eq.2.10 simplifies in cases where only isotropic materials are included in the

layered system or in some special cases where, for example the Cartesian principal axes of the material layers are all oriented parallel to the axes of the laboratory coordinate system. In this case the ellipsometric ratio holds:

$$\rho^{is} = \frac{T_{43}T_{11}}{T_{33}T_{21}}, R_s = \frac{T_{21}}{T_{11}}, R_p = \frac{T_{43}}{T_{33}} \quad (2.19)$$

These coefficients can be experimentally measured.

CHAPTER 3

Experimental Techniques

In this chapter, detailed experimental techniques and instruments used for the work presented are discussed. The thin film deposition and fabrication used and also thin film characterization techniques are included in this chapter. Also, custom-made instruments including the angular-dependent surface plasmon resonance (SPR) / Magneto-Optical Kerr Effect (MOKE) setup and the electrical transport measurement setups are described.

3.1 Deposition and Fabrication Techniques

In this dissertation, a thin film deposition chamber with ultra-high-vacuum (UHV) was used. The pressure of the UHV chamber can be as low as 10^{-10} Torr to achieve the least interaction between the residual gas and thin film growth as well as surface characterization process.

3.1.1 Direct Current (DC) Magnetron Sputter Deposition

Direct current (DC) sputter deposition is one of the most common methods of physical vapor deposition (PVD) techniques used to deposit conducting thin films[37].

Sputtering is a method of physical vapor deposition of thin films of one material onto another material or substrate. This thin film deposition technique is amply used in scientific and industrial applications. The most common sputter deposition methods used are ion beam sputtering, diode sputtering and DC magnetron sputtering.

General Description

A schematic representation of a vacuum chamber used for DC magnetron sputter deposition is shown in Fig.3.1.

Sputtering occurs in a vacuum chamber, where a substance is bombarded with ionized gas molecules that displace atoms. The process involves ejecting material from a “target”, which is a source, onto a “substrate”.

In order to remove contaminations, i.e. gas impurities, the vacuum chamber is evacuated to the lowest achievable pressure or base pressure, typically in the ultra-high vacuum (UHV) regime ($\sim 10^{-9}$ Torr), using different kind of vacuum pumps, including roughing pumps, turbo-molecular and cryo-pumps, according to different pumping ranges.

Magnetrons are used in the sputtering process to help control the path of the displaced atoms that fly randomly around the vacuum chamber and also help lower the pressure needed to sputter the conducting materials. The vacuum chamber is filled with ultra-high purity inert gas such as Argon (Ar) gas (99.999%). Magnetron sputtering sources can be used in the range of 10^{-3} Torr Ar gas to create a plasma.

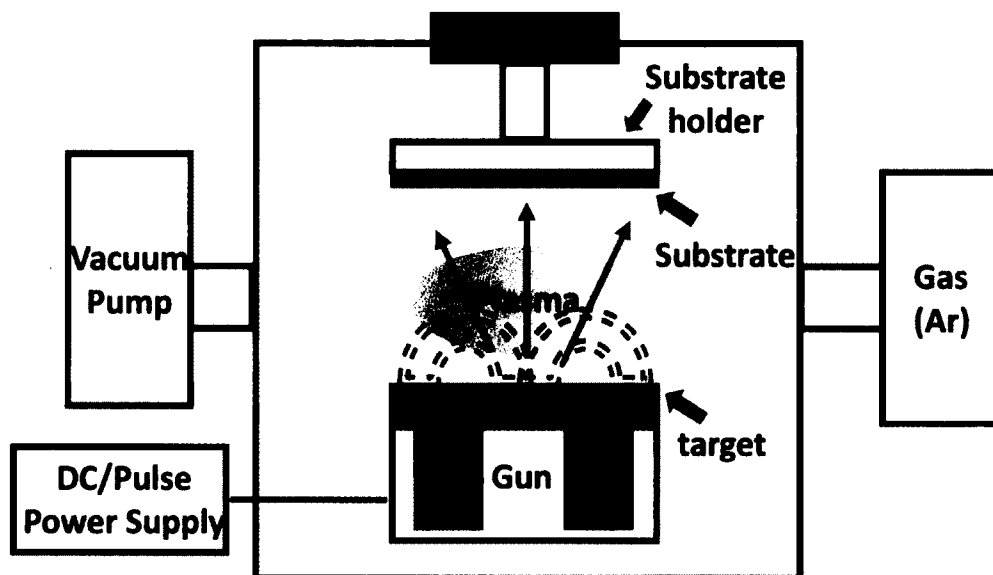


FIG. 3.1: Illustration of DC sputtering

A high negative DC voltage is applied to the target while the sample is grounded. Ions from the plasma are accelerated towards the target due to the high negative DC potential. More ions and electrons are created in the process through an avalanche leading to a self-sustainable plasma. The ejected neutral target atoms fly through some distance and then are deposited onto the surface of the substrate. These atoms hit the substrate and bond to the surface at an atomic level and form a thin film.

3.1.2 Deposition Chambers

Fig.3.2 shows a photograph of the UHV deposition chamber that was used to deposit the DC magnetron sputtered thin films throughout this project. The system has two chambers, the loadlock—used for sample entry purposes— and also the deposition chamber, separated by a gate valve. Four DC magnetron sputter sources are installed in the deposition chamber. The deposition chamber has a surface characterization instrument—reflection high-energy electron diffraction (RHEED)—and also one ion-gun for surface modification purposes.

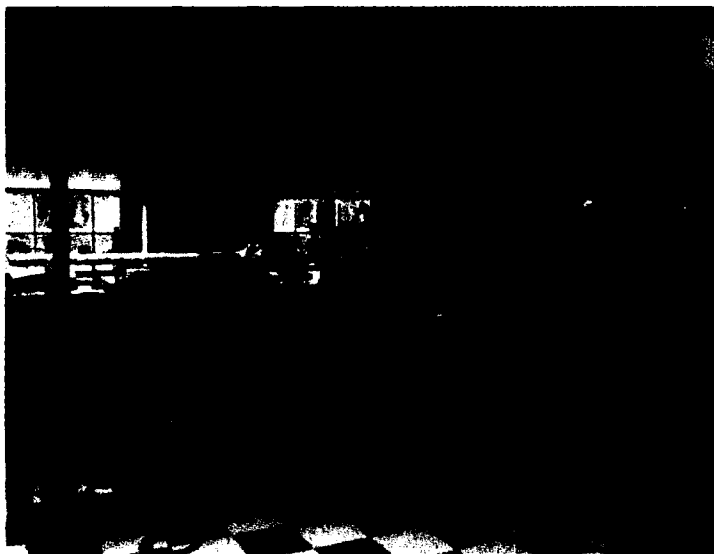


FIG. 3.2: Picture of Perkin-Elmer deposition system

3.2 Characterization Techniques

Several thin film characterization techniques are used in this dissertation. A brief description of the thin film characterization techniques are mentioned in this section, including structural characterization [X-ray diffraction(XRD)]; surface characterization[atomic force microscopy(AFM)] ; magnetic characterization [superconducting quantum interference device (SQUID) magnetometry.

X-Ray Diffraction (XRD) and X-Ray Reflectivity (XRR) The crystal structure and the thickness of the layers was monitored using *ex-situ* x-ray diffraction (XRD) and x-ray reflectivity (XRR) carried out using a standard four-circle diffractometer with Cu K_{α} radiation ($=1.5418\text{\AA}$) in the Bragg-Brentano configuration and with $1/32^{\circ}$ slits. We used PANalytical X'Pert XRD instrument to characterize thin film microstructures. Aspects of our work were carried out using the X'Pert instrument facilitated by NSU through the ARC consortium.

Ellipsometry Variable angle spectroscopic ellipsometry (VASE) is an M-44 VASE J. A. Woollam Co. instrument. VASE provided the actual optical constants in the spectral range of 1.5 to 3 eV.

Scanning Electron Microscopy (SEM) The surface morphology was characterized with scanning electron microscopy (SEM, Hitachi 4700 Scanning Electron Microscope with Energy-Dispersive X-Ray Spectroscopy).

Scanning Transmission Electron Microscopy (STEM) The microstructure of the samples was investigated using scanning transmission electron microscopy (STEM). The specimens were observed with a VG Microscope HB501UX operated at 100 kV and equipped with a Nion 3rd-order aberration corrector and a Gatan Enfina electron energy loss spectrometer capable of providing atomic resolution in both imaging and spectroscopy. Specimens for STEM observations were prepared by conventional thinning, grinding, dimpling and Ar ion milling. Principal component analysis (PCA) was applied to the EELS images to remove random noise. This work was done by Maria Varela from Oak Ridge National Laboratory.

Atomic Force Microscopy (AFM) and Magnetic Force Microscopy (MFM) The surface morphology was investigated using atomic force microscopy (AFM). The AFM experiments were conducted using a Nanotec Electronica Scanning Probe Microscopy (SPM), with AFM/MFM cantilever. We use WSxM program made by Nanotec for Data Acquisition and Processing SPM. The AFM/MFM images were measured under ambient pressure and room temperature.

Superconducting Quantum Interference Device (SQUID) magnetometers Magnetic Property Measurement System(MPMS) SQUID made by Quantum Design was used to measure magnetic hysteresis loops. The MPMS SQUID can achieve 7

Tesla magnet with the temperature range 1.8 —400K.

3.3 Angular-Dependent Surface Plasmon Resonance and MOKE Setup

To realize an experiment that relates surface plasmon resonance and the corresponding response of the angular-dependent Magneto-Optical Kerr Effect(MOKE), a custom-built setup containing all the required laboratory instrumentation is needed. Fig.3.4 shows the setup built to do all these measurements. A custom-made high-precision surface plasmon resonance and transverse MOKE setup was designed to measure optical reflectivity as well as the transverse MOKE signal. The setup uses a goniometer with of 1 thousands of a degree ($1/1000^\circ$) precision. The two arms shown in Fig.3.4 can move independently/dependently and also automatically, controlled by a computer. The arms of the goniometer can only perform x-y plane rotational motion. An image of the setup is shown in Fig.3.3.

There are four main components for the experimental setup: the incident arm and optics, the magnet, the sample and sample stage, and the reflected arm and optics.

3.3.1 Electromagnet

We used a solenoid wrapped around an iron core (pole) to apply the external magnetic field. The solenoid is wound 50 turns around an iron core to amplify the magnetic field, and current can be applied. The solenoid is air-cooled and thus, due to the heating of the solenoid and iron core, the maximum voltage (AC) is around 42 Volts and the corresponding magnetic field is around 800-1000 Oe, which proved sufficient for this work. Due to heating of the solenoid, the resis-

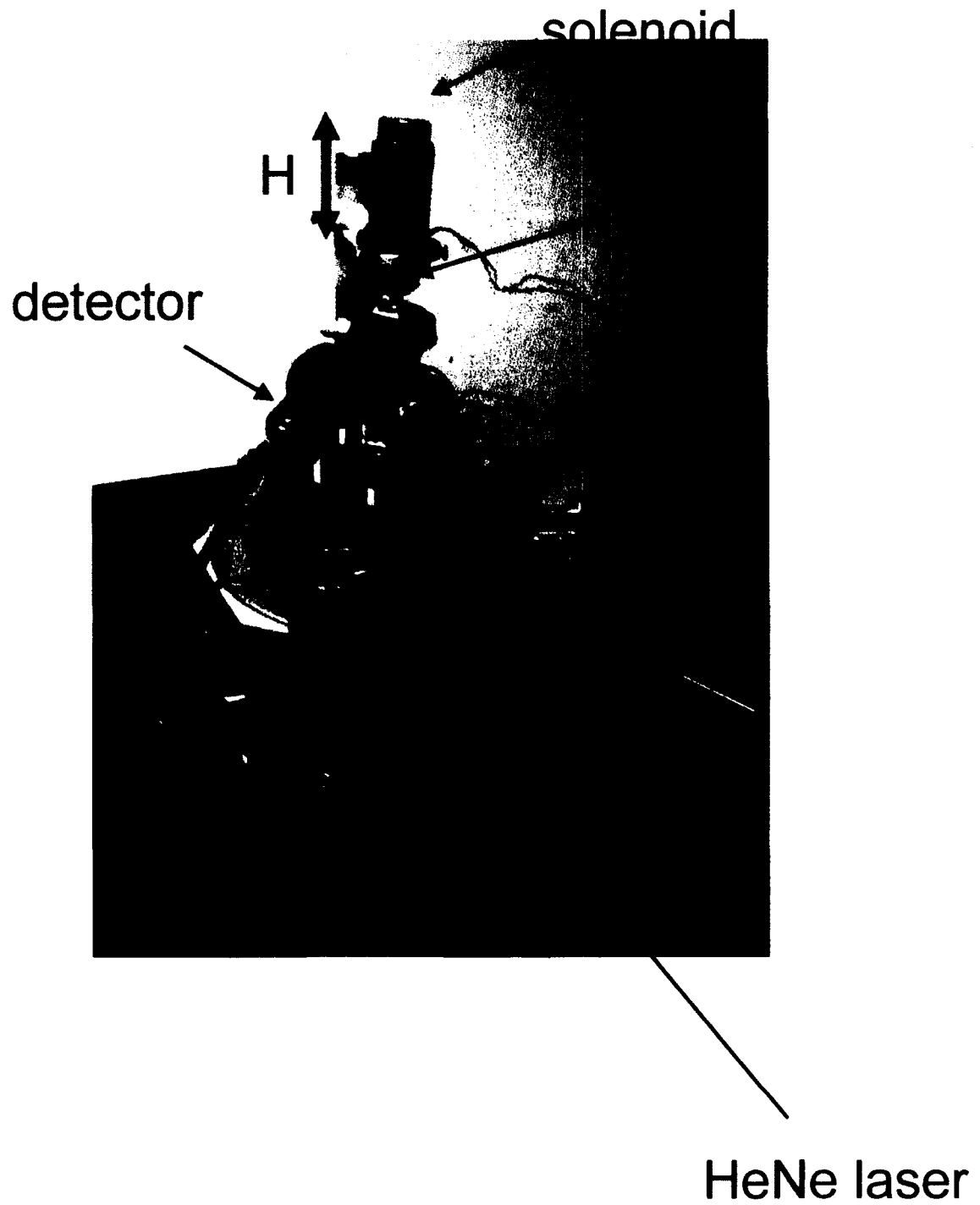


FIG. 3.3: Image of Angular-Dependent Surface Plasmon Resonance and MOKE setup

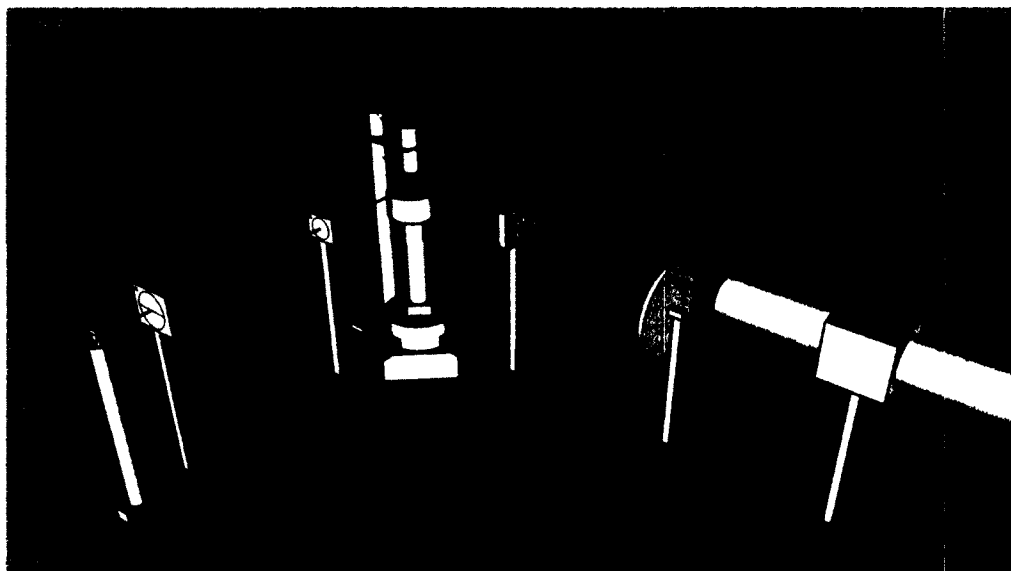


FIG. 3.4: Configuration of Angular-Dependent Surface Plasmon Resonance and MOKE

tance/current slightly changes due to temperature. We recommend to continue the measurement/experiment until the temperature of the solenoid/iron core is stabilized.

A custom-made mount is attached to the electromagnet to keep the electromagnet at a fixed position. The mount can be modified to position the electromagnet in different orientations, e.g. transverse, longitudinal and polar, depending on the configuration desired. For example, in the transverse configuration (shown in Fig.3.4), the electromagnet is placed vertically, with the magnetic field perpendicular to the optical plane and parallel to the sample surface. In order to optimize the magnetic field on the sample, another small coil (not shown) is applied below the optics plane. The small coil is placed coaxial with the electromagnetic solenoid.

We choose to use a Hall probe to fine-calibrate the electromagnet.

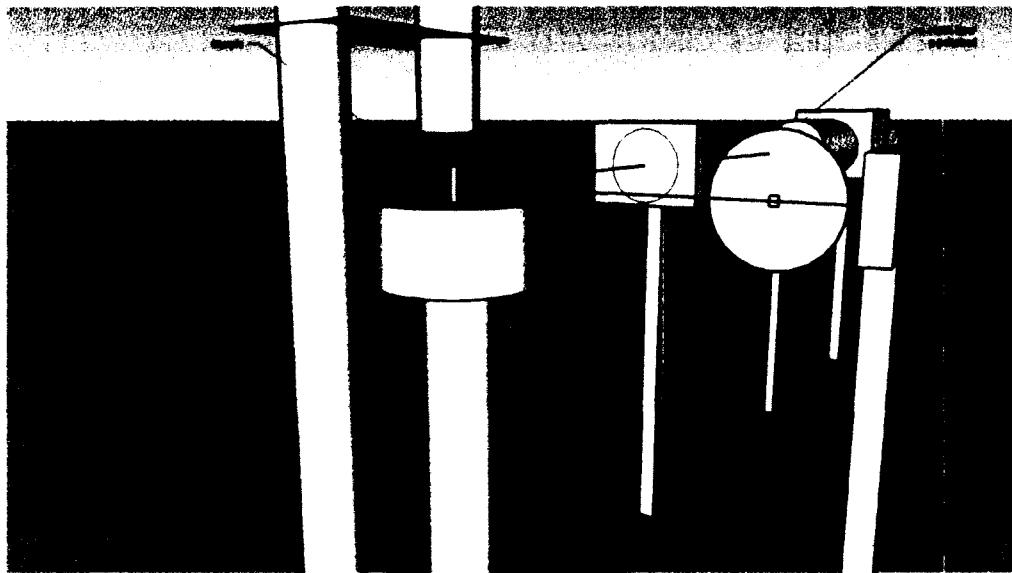


FIG. 3.5: Configuration of Angular-Dependent Surface Plasmon Resonance and MOKE-sample part

Determining the Applied Magnetic Field on Sample

In order to obtain accurate applied magnetic field values on the sample, we conducted measurements of the applied magnetic field with the Hall probe and mapped the field. We first measured the field according to the applied voltage/current and then the distance. It is worth mentioning that the alignment of the top surface of the electromagnet with respect to the position of the sample (the area illuminated by the laser) is crucial to the accuracy of the experiment. Both the x-y position and the orientation of the electromagnet will determine the actual value of the magnetic field applied. Thus, in the experiment, we mounted the top surface of the electromagnet (iron core) parallel to the top surface of a half-cylinder prism and the center of the electromagnet (iron core) just above the center of the illuminated area, in order to obtain accurate magnetic field values.

3.3.2 Sample and Sample Stage

The sample is attached to the half-cylinder prism using matching refractive index liquids. The flat and transparent side of the substrate (soda-lime) is attached to the flat side of the half-cylinder prism using minimum amount of refractive index liquids. The volume of the refractive index liquids needs to be minimal in order to prevent liquid leaks through the bottom of the sample. The spacial gap between the substrate and half-cylinder prism is around 100 microns. After the refractive index liquid fully fills the gap between the substrate and half-cylinder prism, reflection from the back side of the substrate and also the back side of the half-cylinder prism should not be observed.

The sample stage has x, y and z motion with respect to the goniometer, which can be adjusted using a micrometer. There is another rotation attached to the x, y and z stage such that the sample stage could rotate in the x-y plane, with the capability to rotate full turns and also be controlled with a high-precision micrometer. The distance between the top surface of the sample (dependant on the side of the sample) and the electromagnet is kept at a minimum, 5-10 millimeters, to achieve the largest magnetic field possible.

3.3.3 Incident Arm and Optics

The incident arm optics includes HeNe laser (632nm), neutral density (ND) filter, polarizer (optional), half-wave plate/quarter-wave plate (optional) and focus lens. The HeNe laser is mounted in the p-polarized direction and the laser beam is aligned parallel to the goniometer plane/optics plane and also parallel to the incident arm. The height of the laser should be close to the sample height. Depending on the configuration, the wave plate can be mounted to modify the polarization of the incident light. The lens can be used to focus the laser to a specific illuminated area

on the sample surface (radius of the laser spot $\phi \sim 0.5$ millimeter).

3.3.4 Reflected Arm and Optics

The reflected arm and optics are composed of a detector, polarizer (analyzer), and focus lens. A Si (or Ge) detector is used to measure the reflected light intensity.

3.4 MOKE Experimental Setup

An experimental MOKE setup has the advantage of simplicity. If a p-polarized light is incident on a ferromagnetic sample, the reflection consists of an s component (E_s) and a p component, with E_s/E_p being the Kerr rotation. The measurement of the s component could be achieved by adding a linear polarizer (analyzer) in front of the photodetector to eliminate the p component. However, this geometry has disadvantages. First, because the photodetector measures light intensity ($\sim |E_s|^2$), the measured intensity is proportional to the square of the magnetization. Second, it is difficult to quantify the absolute value of the Kerr rotation.

By setting the polarizer (analyzer) at a small angle (δ) from the p axis, the above disadvantages can be solved, as shown in Fig. 3.6. In this method, the intensity measured by the photodetector is:

$$I = |E_p \sin \delta + E_s \cos \delta|^2 \approx |E_p \delta + E_s|^2 \quad (3.1)$$

The equation can also be written as:

$$I = I_0 \left(I + \frac{2\phi'}{\delta} \right) \quad (3.2)$$

with:

$$I_0 = |E_p|^2 \delta^2 \quad (3.3)$$

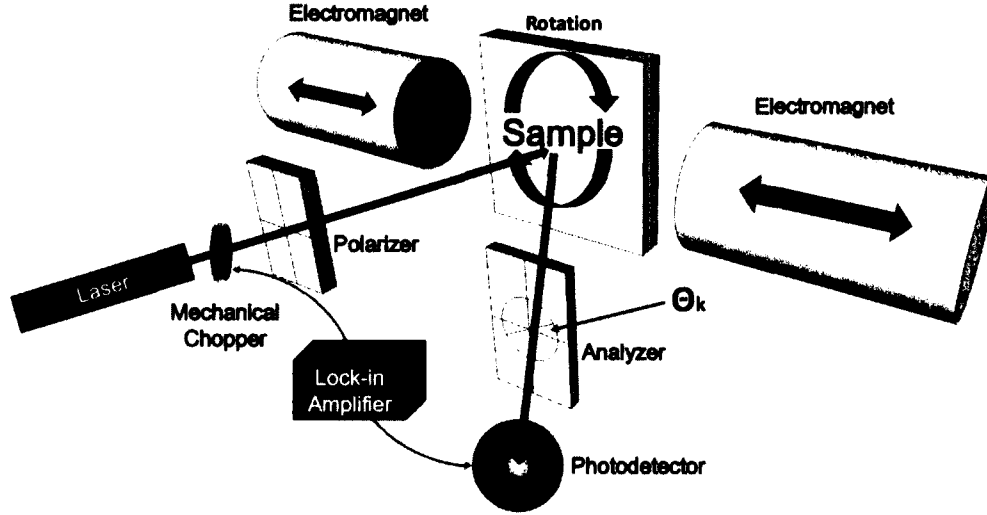


FIG. 3.6: Schematic of MOKE setup used for measuring the magnetic hysteresis loop of thin films

representing the intensity at zero Kerr rotation.

Both ϕ' and ϕ'' are linearly related to the magnetization, thus the measured intensity as a function of H yields a magnetic hysteresis or M-H- loop.

The saturation Kerr rotation ϕ'_m can be determined by the relative change of the Kerr intensity ΔI obtained upon reversing a field value that is equal to or greater than its saturation value:

$$\phi'_m = \frac{\delta}{4} \cdot \frac{\Delta I}{I_0} \quad (3.4)$$

In the experimental setup, intensity-stabilized laser (e.g. He-Ne laser with wavelength of 632 nm) is usually used as a light source. A lens can be used to focus the light beam into a small spot on the sample surface. The sample can be mounted on a rotational stage located between two electromagnets, which allows the magnetic field to be applied along different crystallographic directions (azimuthal directions).

Lock-in detection techniques can be used to improve the signal/noise ratio.

Hysteresis loops can be collected by means of a photodiode and use of an incident beam whose polarization is modulated by a commercial photoelastic modulator or a mechanical chopper to enable lock-in detection.

3.5 Electrical Transport Measurement

A Quantum Design MPMS SQUID (Superconducting Quantum Interference Device) system that can provide accurate measurement of magnetic moments with intense external magnetic fields (maximum 7 Tesla) and temperature (minimum 2K) was used. With the installation of an external device control (EDC) option, the MPMS system can also use other external equipment to conduct other measurements, such as the measurement of electrical transport with Keithley nanovolt and micro-amp meters controlled by computer using a programmable sequence in conjunction with MPMS Multivu software. A custom-built electrical transport measurement setup was designed for measuring the electrical (DC) conductivity/resistivity under a strong applied magnetic field, and also under low temperature (cryogenic). Both the material and the structure of the core part of the system—the four-point probe—was designed for that purpose.

3.5.1 Four-Point Probe

In order to measure precise resistance under an applied magnetic field (7 Tesla maximum) and cryogenic conditions (up to 20K), the materials of the custom-made four-point probe were selected. An oxygen-free high thermal conductivity (OFHC) copper (Cu) plate was used to hold and support the substrate. We used Tungsten (W) as a pin material to minimize thermal effects and the magnetic response. We chose Teflon to secure the four-probe pin, in order to minimize the electrical conductivity and the cryogenic response. Single-strand cryogenic wire made of Phosphor

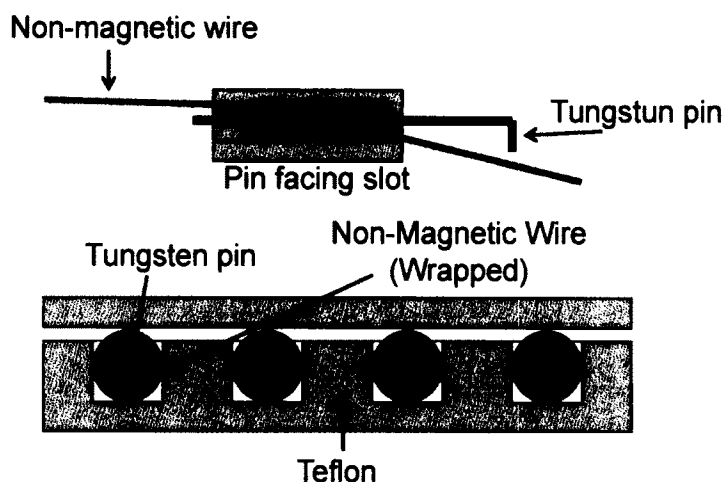


FIG. 3.7: Illustration of the four-point probe

bronze, which is non-ferromagnetic, was used for the connection between the pin and electronics. The wire has a relatively low temperature dependence of its resistance from room temperature to liquid helium temperatures. Polyimide insulation covers the non-magnetic cryogenic wire.

The custom-made four-point probe can provide precise measurements of resistance under the desired environment ($H=1$ Tesla and $T=20$ K).

Fig.3.8 and Fig.3.9 show images of the four-point probe described. The pin-pin distance is 0.5". The four-point probe is mounted with the four pins facing a Cu plate. The pins are designed to touch the measurement area of the sample to guarantee the precise measurement of resistance.

3.5.2 Precision Current Source/Nanovolt Meter Setup and Control

A Keithley 6220 Precision Current Source, with corresponding positive and negative electrodes and grounding, is shown on top in Fig.3.8; a Keithley 2182A Nanovolt Meter, with just the corresponding positive and negative electrodes, is

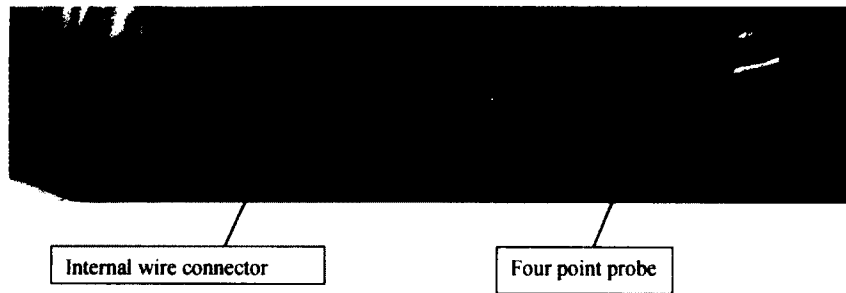


FIG. 3.8: Image of the four-point probe (top view)

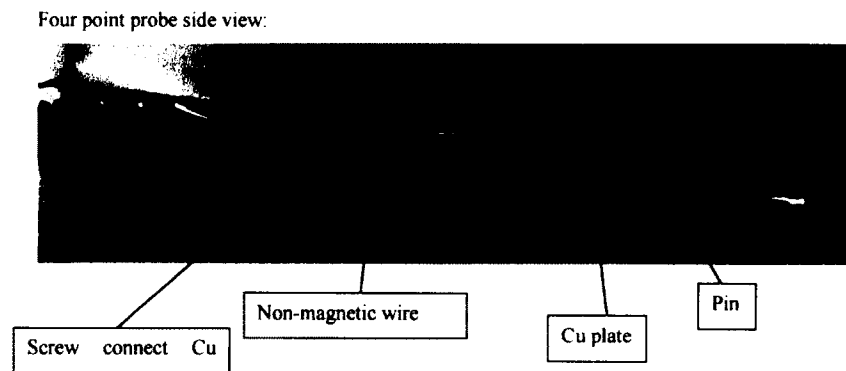


FIG. 3.9: Image of the four-point probe (side view)

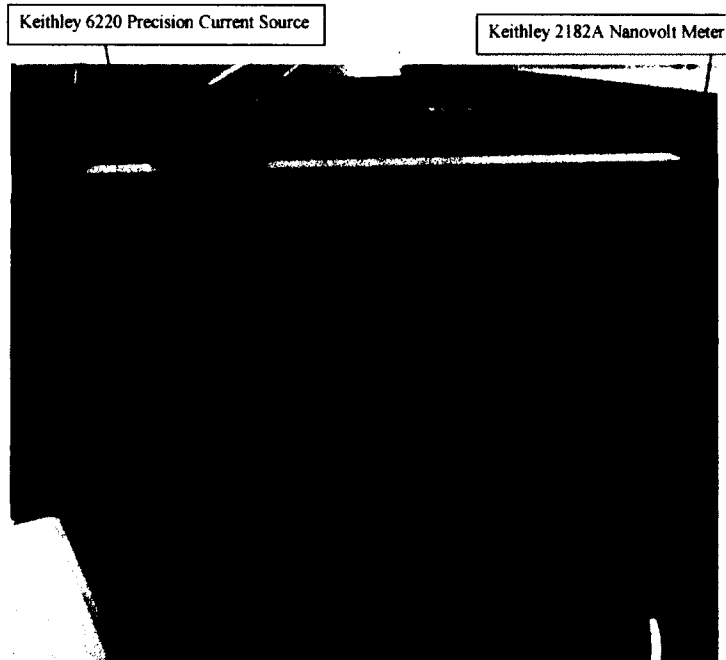


FIG. 3.10: Image of Keithley 6220 Precision Current Source and 2182A Nanovolt Meter

shown below it. The Keithley 2182A Nanovolt meter has only the corresponding positive and negative electrode. The two electrodes are connected to Channel 1 (maximum 10V) due to high voltage when the current source switching on and off.

The EDC program is a programmable file which can operate external devices (like the 6220, 2182A, etc.) with the control of the SQUID and SQUID Multivu software. The EDC program can be used by Multivu to operate the custom-made four-point probe described in Page44. With the precision current source, current from 1nA to 1 mA can be applied.

The current applied to the four point probe can dramatically change the resistance measured. A smaller current (1 nA minimum) will introduce less disturbance including heat, electric density, etc. to the sample surface, but will have more noise in the background and signal.

A larger current (normally larger than 100 μ A) will introduce dramatically-

localized heat accumulation and electric density changing between the film and substrate, thus making thermal/electrical drift with resistance measured with the nanovolt meter. The current depends on the 1) thickness of the film, 2) contact of the pins and 3) temperature, and may vary from sample to sample. Careful selection of current applied to the four-point probe needs to be experimentally determined.

CHAPTER 4

Magnetic Field Modulation of Intense Surface Plasmon Polaritons on Au/Co/Au Multilayer Thin Films

4.1 Introduction

Surface plasmon polaritons (SPPs) are transverse magnetic (TM) surface waves propagating along the interface between two materials with dielectric constants of opposite sign, generally a metal and a dielectric[28]. They result from the interactions between an illuminating wave and the free electrons of the conductor, generating highly confined electromagnetic (EM) fields at the interface. SPPs have been extensively studied and used in a number of applications, including biosensors [35], optical modulators and switches[38], and new generation plasmonic devices[38]. SPP technology is an attractive platform for the development of nanoscale optical

integrated circuits with passive and active devices, achieving and controlling light propagation in sub-wavelength geometries[39]. Thus, the control of SPPs by external magnetic fields has led to striking results, such as the manipulation of optical transmission through magneto-plasmonic crystals with external magnetic fields[40][41] or the control of terahertz SPPs on semiconductor surfaces by applying an external static magnetic field[42]. As a consequence, a number of technological applications have appeared in the last few years, including magneto-plasmonic optical modulators[43], optical isolators[44] and magneto-plasmonic sensors[45]. Nevertheless, for many applications it is important to achieve high intensity SPPs that also exhibit strong dependence on externally applied magnetic fields.

Previous reports have indicated that the SPP dispersion relation can be affected by applying magnetic fields perpendicular to the propagation vector of the SPP and along the surface, i.e. in the so called transverse configuration[46], in single layered magnetic materials[47], giving rise to field-dependent variations of the SPP wave vector k_{sp} . This effect has been observed for bounded SPP modes in which the electromagnetic field generated by the SPPs in the metallic film decays exponentially in the surrounding dielectric films[48] and for symmetric leaky SPP modes in which the electromagnetic field decays in the dielectric with lower refractive index and radiates towards the dielectric of higher refractive index[47][Fig.4.1(a)]. The leaky modes are of special interest, since they generate very intense localized EM fields, and thus they are very sensitive to the interface conditions, giving rise to applications as sensors and for signal transmission in integrated circuits. These modes can be excited in the Kretschmann configuration[49][50], where the metallic films are optically coupled to a prism and far-field light is angled through the prism such that the in-plane wave vector $k_{||} = K_0 n_{prism} \sin\theta$ matches the associated SPP propagation constant k_{sp}^1 [Fig.4.1(a)], where $k_0 = \omega/c$ is the wave number in vacuum, θ is the incidence angle and n_{prism} is the refractive index of the prism.

Unlike the bounded modes, these modes lose energy not only due to the inherent absorption inside the metal, but also due to leakage radiation emitted into the prism. Thus, in the Kretschmann configuration a minimum in the reflected intensity is obtained at a critical incidence angle θ_c due to destructive interference between the leakage radiation emitted by the excited SPPs and the incoming light at the boundary with the prism[28]. This minimum actually vanishes for a critical metal thickness d_c , associated with optimum SPP excitation and thus leading to maximum EM fields. Such critical thickness depends strongly on the absorption losses of the metal. Thus, in this configuration and for magnetic metals, the variation of the SPP wave vector k_{sp} when an external magnetic field is applied [Fig.4.1(b)] gives rise to a change of the SPP excitation condition and thus to a shift of the critical incidence angle θ_c . As a consequence, a strong field-dependent variation of the reflectivity is observed giving rise to a strong enhancement of the transverse magneto-optical Kerr effect (TMOKE)[51][52]. Nevertheless, ferromagnetic metals such as Fe and Co have very high absorption losses compared to noble metals, i.e. Au and Ag, giving rise to overdamped SPP modes associated with low EM fields. Figure 4.1(b) shows the dispersion relation for the symmetric leaky SPP modes in Au and Co illuminated in the Kretschmann configuration using a quartz prism. Due to the high absorption of Co, the SPP dispersion relation is similar to that of light propagating through air. Combined noble-ferromagnetic systems have been proposed as Au/Co/Au trilayers)[51][52][53], giving rise to a system with lower absorption losses and thus higher EM fields but still with sensitivity to external magnetic fields. In their studies, special attention was devoted to the large enhancement of the magneto-optical (MO) activity associated with the SPP excitation[54].

In the present studies, rather than optimizing the MO response, our attention was devoted to optimum excitation of SPPs, leading to maximization of the generated EM fields at the surface without compromising dependence with externally

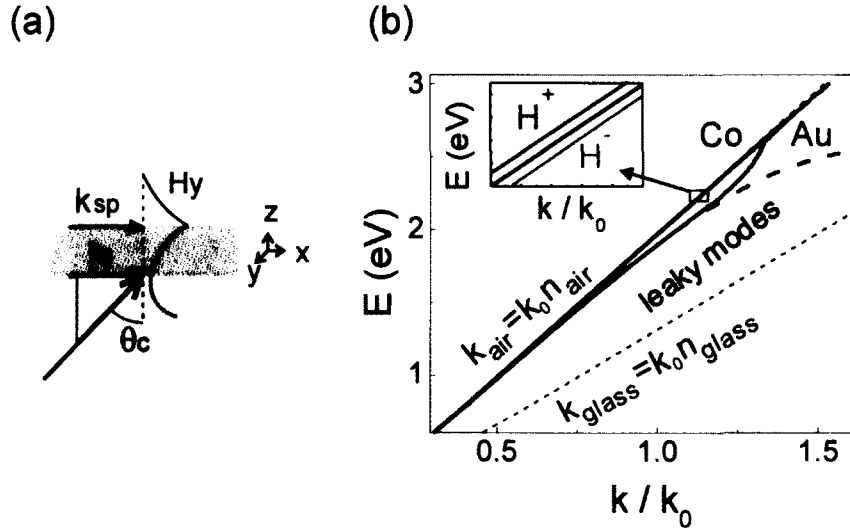


FIG. 4.1: (a) Schematic view of momentum matching in the Kretschmann configuration, where far-field radiation couples symmetric leaky SPP modes at the air-metal interface by means of a glass prism. H_y represents the only magnetic component in the TM mode. (b) Dispersion relation for such modes in Co and Au films considering their absorption losses. The dashed line shows the dispersion relation for Au considering no absorption losses. The dispersion relation of Co splits into two branches when external magnetic fields are applied along the y direction.

applied magnetic fields. To this end, Au/Co/Au trilayers were grown by sputter deposition on glass slides with the Co layers placed at different distances from the surface and with different thickness. We have been able to probe the SPP generated EM fields, and to demonstrate that it is experimentally possible to achieve optimal SPP excitation with strong dependence on external magnetic fields.

4.2 Experimental

Au/Co/Au trilayers were grown on soda-lime glass substrates via magnetron sputtering deposition in an ultra high vacuum (UHV) system under a base pressure in the low 10^{-9} Torr range. Slow deposition rates of 0.066 \AA/s and 0.319 \AA/s for Co and Au respectively allowed accurate thickness control. Soda-lime glass substrates, previously cleaned ultrasonically in successive baths of acetone and methanol, were

UHV annealed at 600°C for 30 minutes in order to planarize the surface[52]. Subsequently, a Au buffer layer was grown at RT and then annealed for 10 minutes at 350°C in order to further planarize the Au surface before Co growth. Co films with thickness ranging from 2.5 to 10 nm were grown at 150°C to favor surface diffusion of the incoming adatoms and thus give rise to a bi-dimensional growth mode with low interfacial roughness. Finally, a 3 nm thick Au capping layer was grown to prevent Co oxidation and to improve the generation and propagation of the SPPs on the upper metal-air interface. The thickness of the different layers was monitored using *ex-situ* x-ray reflectivity (XRR) carried out using a standard four-circle diffractometer with Cu K_α radiation ($=1.5418\text{\AA}$) in the Bragg-Brentano configuration and with $1/32^\circ$ slits. Variable angle spectroscopic ellipsometry provided the actual optical constants for the Au and Co layers in the spectral range of 1.5 to 3 eV.

The optical and MO response of the multilayers under SPP excitation were investigated in the Kretschmann configuration using p-polarized He-Ne laser radiation ($=632.8\text{ nm}$). In this configuration [Fig.4.1(a)], the glass substrate is coupled to a semicylindrical glass prism by a matching refractive index liquid. In our experimental setup the prism was mounted on an automated goniometer allowing illumination in total internal reflection with variable incidence angle θ and angular resolution of 10^{-4} degrees. A Si amplified photodetector preceded by a p-oriented polarizer was used to detect intensity variations in the reflected radiation. The TMOKE was also investigated by applying a 30 mT alternating magnetic field (60 Hz) in the plane of the sample and perpendicular to the incidence plane, intense enough to saturate the Co layers with in-plane magnetization. The TMOKE signal, i.e. the intensity variation of the p-polarized reflected light when applying magnetic fields in opposite directions $\Delta R_{pp} = R(+H) - R(-H)$, was detected and analyzed using lock-in techniques.

4.3 Results and discussion

Maximum SPP-generated EM fields are obtained when illuminating under the critical incidence angle θ_c and for a critical thickness d_c that depends strongly on the dielectric constants of the metal. Fig.4.2 (a) shows reflectivity curves for Co and Au films for which the absorption losses are considerably different and thus their critical thicknesses d_c are 9.7 and 48.2 nm respectively. A much broader reflectivity curve is obtained for Co due to its higher absorption. For these particular thicknesses, maximum EM fields appear at the metal/air interface as shown in Fig.4.2(b). Nevertheless, high absorption losses in Co drastically reduce the SPP-generated EM fields in this metal. On the other hand, Co films alone exhibit maximum TMOKE response ΔR_{pp} , as shown in Fig.4.2(c). Thus, Au-Co multilayered systems are better suited to achieve SPPs with larger localized electromagnetic fields that can also be modulated by externally applied magnetic fields. Several factors have to be taken into account to accomplish this scenario, namely accurate control of the total thickness of the full trilayer, the thickness of the Co layer and its position within the film, as well as the discrepancy between the optical constants in very thin layers with respect to bulk values. In these studies the top Au layer thickness was minimized to 3 nm to allow the Co film to be as close as possible to the excited SPP thus making the trilayer system more sensitive to external magnetic fields. Fig.4.2(d), (e) and (f) show the minimum value of the reflectivity R_{min} , the maximum value of the electromagnetic field $|H_y|_{max}$ and the maximum value of the MO activity ΔR_{max} for Au/Co/Au trilayers with each combination of Co and Au thicknesses calculated using transfer matrix formalism[36][55] and bulk optical constants[56] at 1.96 eV.

The maximum intensity of the SPP generated H_y is obtained for single Au films and decays abruptly when Co is inserted in the structure as shown in Fig.4.2(e). On the other hand, the maximum TMOKE response ΔR is obtained for pure Co

films, decreasing progressively when Au is inserted in the structure. Thus, in order to achieve large EM fields in the upper Au-air interface while keeping sensitivity to external magnetic fields it is necessary to minimize the Co layer thickness. Nevertheless, to maintain the integrity of the trilayer structure, the Co film needs to be thick enough to guarantee its continuity as a full layer. We have estimated that 3 nm is the minimum Co thickness that can yield a continuous Co layer when deposited on the Au buffer[57]. For such Co thickness, and considering a 3 nm thick Au capping layer mentioned previously, the maximum SPP generated EM field is obtained when the buffer layer is 20 nm thick so that the critical thickness is achieved, as shown in Fig.4.2(e) .

Nevertheless, due to the dependence of the optical constants with thickness in thin layers, the critical thickness might not be experimentally achieved for the predicted Au buffer and Co layer thickness. For this reason, a series of Au (3 nm)/Co (dCo)/Au (20 nm)/glass trilayer structures with different Co thickness from dCo =2.5 to 10 nm was prepared. Figure 4.3(a) shows the angular dependency of the p-polarized reflectivity in the Kretschmann configuration R_{pp} for the different trilayers. Evidence of SPP excitation is the characteristic minimum observed in reflectivity around the resonance angle $\theta_R \sim 44.7^\circ$. A minimum reflectivity value as low as 1×10^{-5} was obtained for d Co =2.8 nm. The inset in Figure 4.3(a) illustrates how critical the optimization of the Co layer thickness is to minimize the overall reflectivity of the sample. Indeed, our experimental results show a good agreement with simulations using the transfer matrix formalism as shown in Fig.4.3(b).

Interestingly, direct correlation of the Co optical constants with film thickness is observed [Fig. 4.3(c)]. We note that in previous studies, several other properties have also been reported to be Co-thickness dependent in Au/Co/Au trilayers, e.g. Co lattice parameter[57], magnetic anisotropy[58] or magnetic moment[59][60] to name a few. These changes are primarily due to the misfit between the Co and

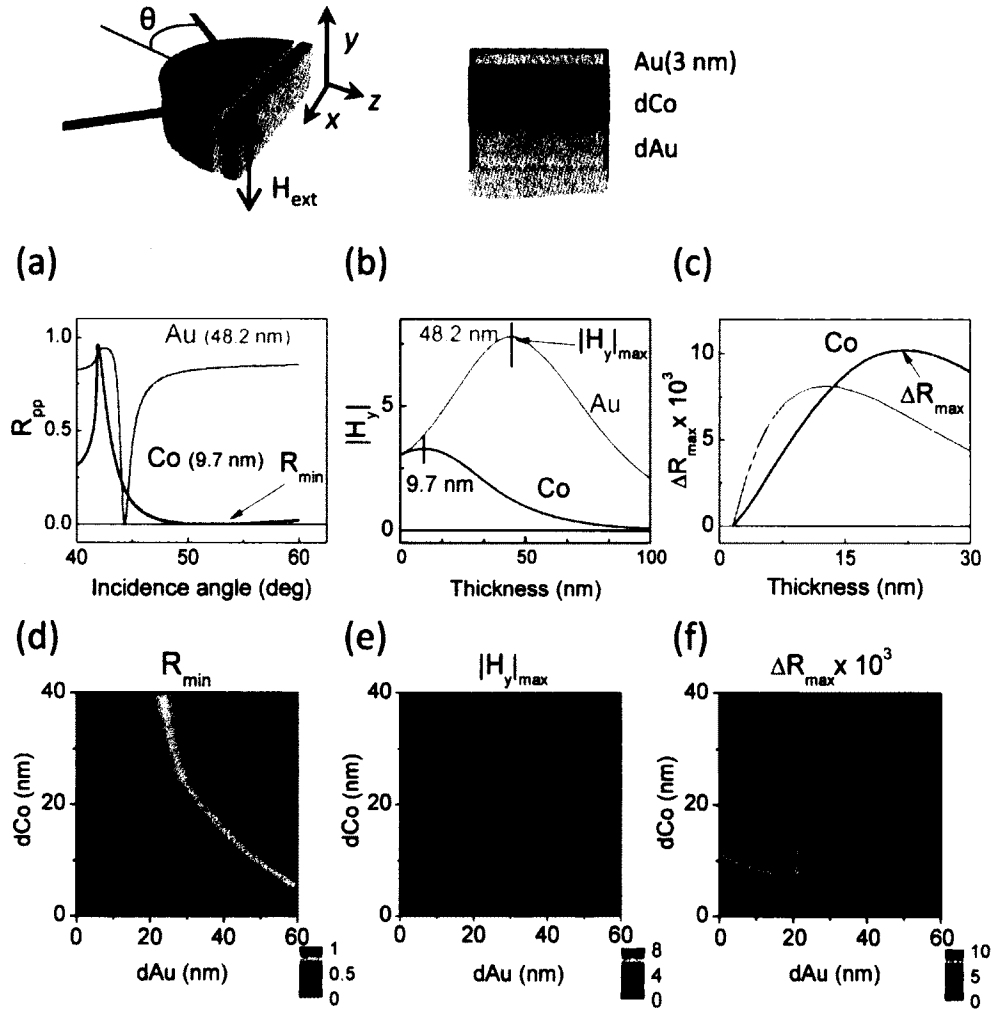


FIG. 4.2: Schematic view of the SPP excitation in the Kretschmann configuration for the Au(3nm)/Co(dCo)/Au(dAu) trilayers where external magnetic field H_{ext} is applied along y . (a) Reflectivity curves calculated for Co and Au films with critical thickness, (b) SPPs $|H_y|$ at the metal-air interface for Co and Au films as a function of the thickness and (c) Transverse magneto-optical Kerr effect R for a single Co film and for Au(3nm)/Co(dCo)/Au(20 nm) trilayers as a function of the Co thickness. The lower row represents calculations of (d) R_{min} , (e) $|H_y|_{max}$ and (f) ΔR_{max} for any combination of Au and Co thickness in the Au(3nm)/Co(dCo)/Au(dAu) trilayers.

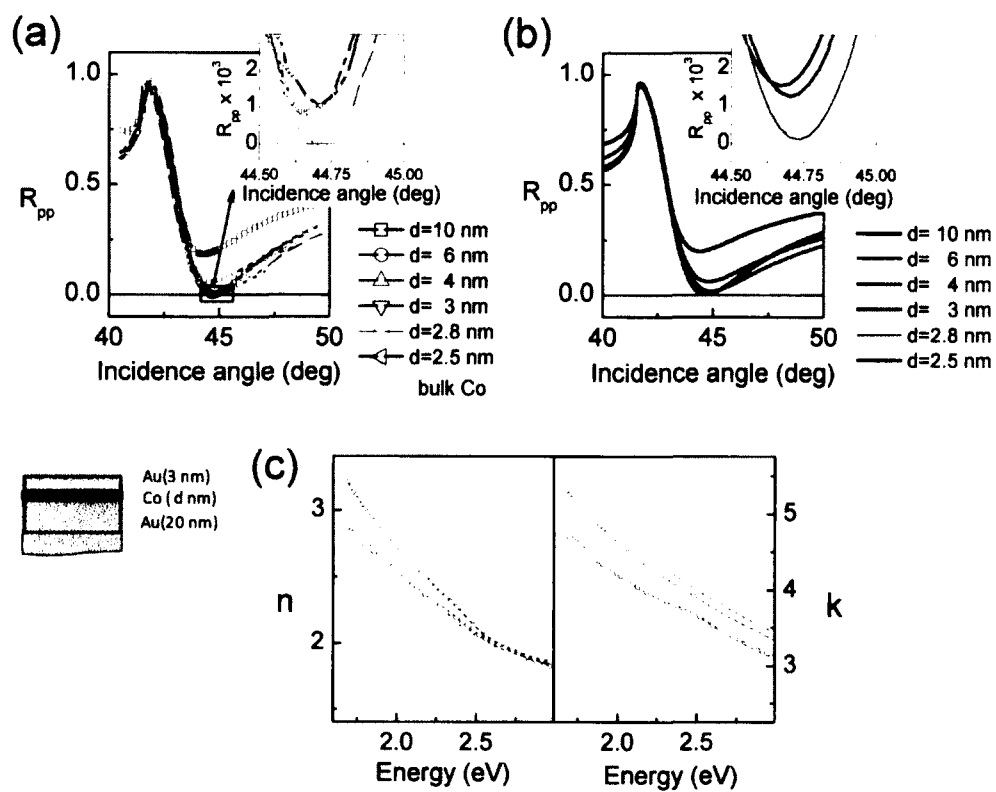


FIG. 4.3: (a) Experimental and (b) simulated angular dependency of the reflectivity with no external magnetic field applied R_{pp} for the Au(3 nm)/Co(d Co)/Au(20 nm) trilayers with d Co ranging from 2.5 to 10 nm. (c) Real (n) and imaginary (k) parts of the complex refractive index of Co film measured with ellipsometry.

Au lattices and also due to confinement effects since the Co thickness approaches a monolayer. In the present case, we find a progressive decrease in the absorption coefficient k as the Co thickness increases approaching the bulk value, while n is nearly constant for all samples but slightly higher than bulk value.

In order to discuss the MO response of these trilayers, we recall that the shift observed in the position of the reflectivity minimum in magnetic materials is due to modification of the SPP wave vector by the external magnetic field. Figure 4.4(a) shows the angular dependency of the MO signal ΔR_{pp} for the Au(3 nm)/Co (d)/Au (20 nm)/glass trilayers with different Co thickness from $d=2.5$ to 10 nm, exhibiting a resonance-like feature associated with SPP excitation around θ_c for all the trilayers. In this case, a maximum value of $\Delta R_{pp} = 7 \times 10^{-3}$ is obtained for the trilayer with Co thickness $d=10$ nm, decreasing for lower and higher Co thicknesses in agreement with the simulations in Fig.4.2(c). The variation of the SPP wave vector $\Delta k_{sp} = k_{sp}(+H) - k_{sp}(-H)$ when magnetic fields are applied in opposite directions along y was simulated using transfer matrix formalism[36][55], and imposing the boundary conditions characteristic of symmetric leaky SPP modes, i.e. an exponential decay of the EM field in the air-metal interface and an exponential increase at the lower Au-prism interface[49]. Figure 4.4(b) shows the calculated Δk_{sp} variation of the SPP k-vector for the Au(3 nm)/Co (d)/Au (20 nm)/glass trilayers with varying Co thickness from $d=2.5$ to 10 nm, where a maximum variation is obtained around the radiation energy used in our experiments (1.96 eV). In addition, we observe that the variation of the SPP k-vector scales with the maximum value of the magneto-optical activity ΔR_{pp}

To continue our discussion on the magneto-optical properties of the trilayers, we consider that the transverse MOKE signal is typically expressed as the normalized variation in reflectivity of the p-polarized light:

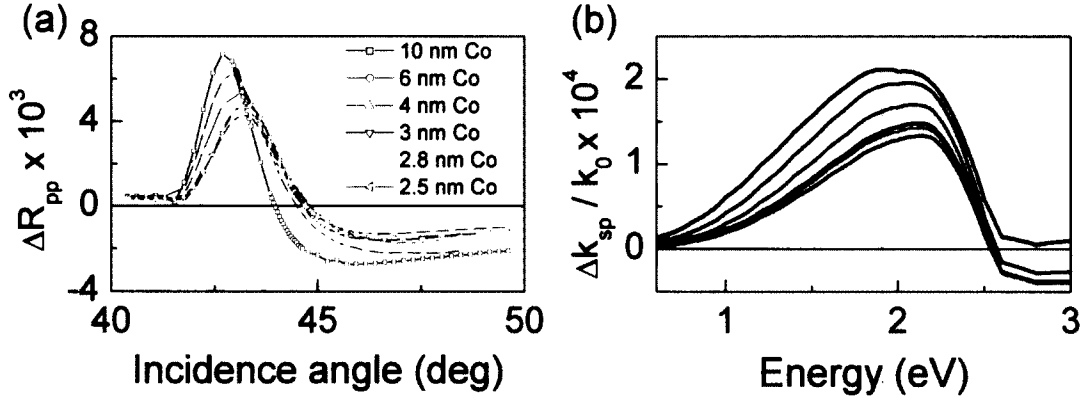


FIG. 4.4: (a) Transverse magneto-optical Kerr effect $\Delta R = R(+H) - R(-H)$ measured in the Kretschmann configuration for the Au(3 nm)/Co(d)/Au (20 nm) trilayers with d ranging from 2.5 to 10 nm. (b) Field dependent variation of the SPP wave vector $\Delta k_{sp} = k_{sp}(+H) - k_{sp}(-H)$. The dashed line represents the energy of the radiation used in the measurements $E=1.96$ eV.

$$\frac{\Delta R_{pp}}{R_{pp}} = \frac{R_{pp}(+H) - R_{pp}(-H)}{R_{pp}(0)} \quad (4.1)$$

The magnitude of this ratio might be misleading in systems illuminated in the Kretschmann configuration since the reflectivity tends to zero in optimized samples whereas the field dependent variation of the reflectivity does not. Nevertheless, this ratio can be used in sensing applications as previously demonstrated[35][45], because the sensitivity is strongly enhanced when the critical thickness is achieved. Figure 4.5 shows $\Delta R_{pp}/R_{pp}$ measured for the Au(3 nm)/Co(d nm)/Au(20 nm) trilayers. A maximum value of $\Delta R_{pp}/R_{pp} \sim 3.2$ (relative variation of 320%) is found for the trilayer with $d=2.8$ nm, which is the highest value ever reported for this system to the best of our knowledge.

Once the critical thickness for this system was experimentally achieved, we analyzed the distribution and intensity of the EM fields within the samples. Hermann et al.[51] showed how the MO response of multilayers incorporating a magnetic thin layer is related to the intensity of the EM fields at the position of the magnetic layer.

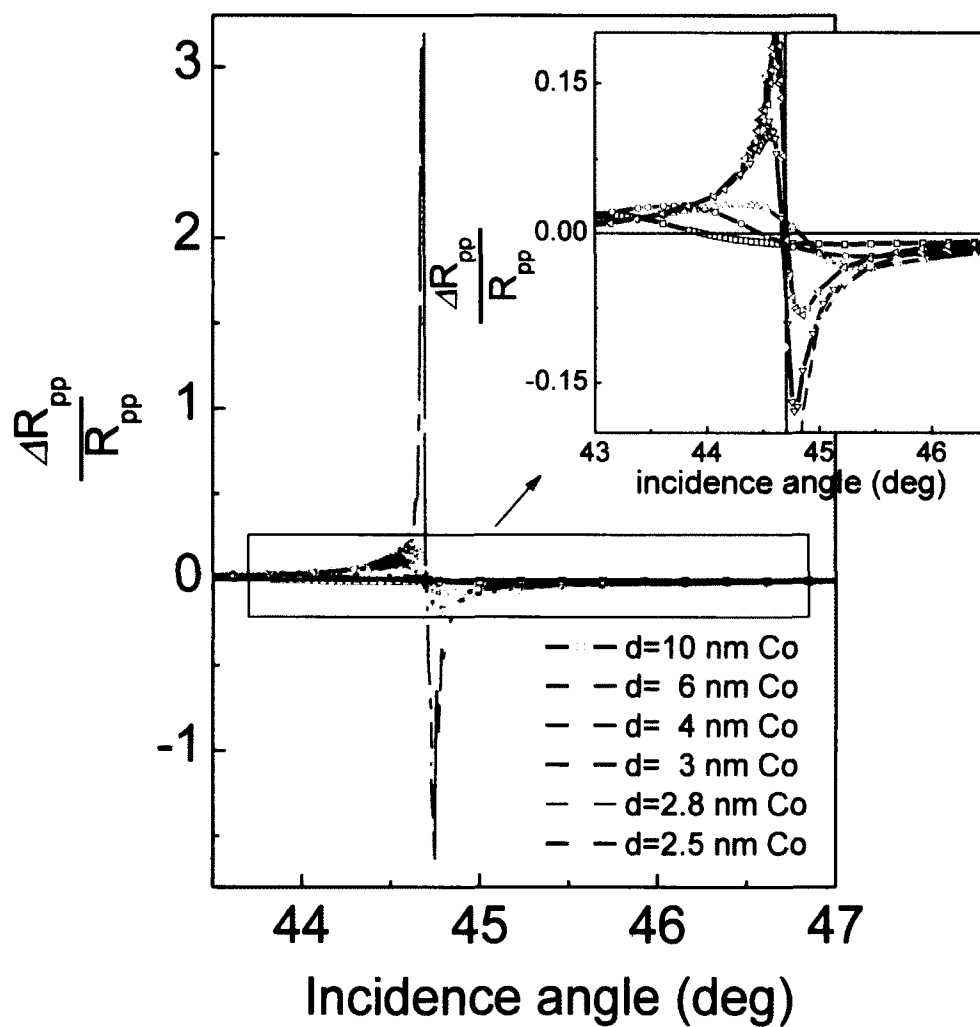


FIG. 4.5: Angular dependence of the relative variation in reflectivity $\Delta R_{pp}/R_{pp}$ for the Au(3 nm)/Co(d)/Au(20 nm) trilayers with d ranging from 2.5 to 10 nm. A maximum value of $\Delta R_{pp}/R_{pp} \sim 3.2$ (relative variation of 320%) is found for the trilayer with $d=2.8$ nm.

They showed that in the TMOKE geometry, the variation of the complex reflection coefficient for p-polarized light Δr_{pp} is directly proportional to the product of the TM electric field components (E_x and E_z) [54] within the magnetic layer, which along with H_y are the only EM fields present in TM modes. In the ultrathin film limit, where the electric fields can be considered constant within the magnetic film, the relationship is [51][61]:

$$\Delta r_{pp} = \frac{ik_0^2}{2\kappa_1 t} \epsilon_{xy} l_m E_x E_z \quad (4.2)$$

where $k_0 = \omega/c$ is the wave number in vacuum, κ_1 is the z component of the incident light wave vector at the first interface, ϵ_{xy} are the MO constants of the magnetic film, l_m is the thickness of the magnetic film and t accounts for the absorption of such film [51]. Thus, by placing a MO active layer within the Au film and measuring the variation of the complex reflectivity it is possible to probe the actual intensity of the SPP generated EM fields at the location of the magnetic layer. We used this method to study the intensity and spatial distribution of the SPP generated electromagnetic fields. For this study we prepared Au/Co/Au trilayers with critical thickness (25.8 nm) and with a 2.8 nm thick Co layer positioned at different distances from the upper air-Au interface as shown in Fig. 4.6. Reflectivity and MO measurements in different configurations were carried out in order to extract the change in the complex reflection coefficient Δr_{pp} when an external magnetic field is applied as shown in Ref [51]. For this we used p polarized light [Fig.4.6(a)], light rotated 45° from the p-axis and with a polarization analyzer oriented at 45° [Fig.4.6(b)], light rotated 45° from the p-axis and with a quarter wave plate with its fast axis along p followed by a polarization analyzer oriented at 45° [Fig.4.6(c)] and s-polarized light [Fig.4.6(d)]. Thus, the left column in Fig. 4.6 shows the reflectivity vs. incidence angle in the different configurations whereas the right column displays

the MO response in each case. No MO response is obtained with s polarized light. In spite of the fact that all the samples have the same total Au and Co thickness, slight variations in the reflectivity curves are found due to slight modification of the excitation conditions of the SPPs by inserting a Co film in different positions.

The variation of the complex reflection coefficient Δr_{pp} and thus the product of the TM electric field components (E_x and E_z) as a function of the position within the Au films can be obtained using the experimental data in Fig. 4.6, as described in Ref [51]. Figure 4.7(a), shows the measured $E_x E_z$ fields when positioning the Co film at different distances to the upper Au- air interface, normalized to the incident radiation. The results show the expected SPPs generated EM fields exponential decay as the distance to the upper Au-air interface increases. The EM field at the Au-air interface can be calculated using these results and taking into account the exponential decay of the $E_x E_z$ product and the difference between the dielectric constants of Au and Co that affect the E_z component. The calculated intensity of the EM field at the upper interface is shown with a dashed line in Fig.4.7(a), exhibiting a normalized $E_x E_z$ value around 0.43 at the critical angle when SPPs are excited, compared to a much lower value of 0.1 expected for single Co films of critical thickness. Our experimental results are in good agreement with the EM field intensity simulations for Co layers at different positions within the trilayers [Fig.4.7(b)]. Thus, we have demonstrated experimentally that for tailored trilayers with total critical thickness and a thin Co layer placed close to the air-metal interface, namely Au(3 nm)/Co (2.8 nm)/Au (20 nm)/glass, very high SPP-generated EM fields are achieved while keeping high sensitivity to externally applied magnetic fields.

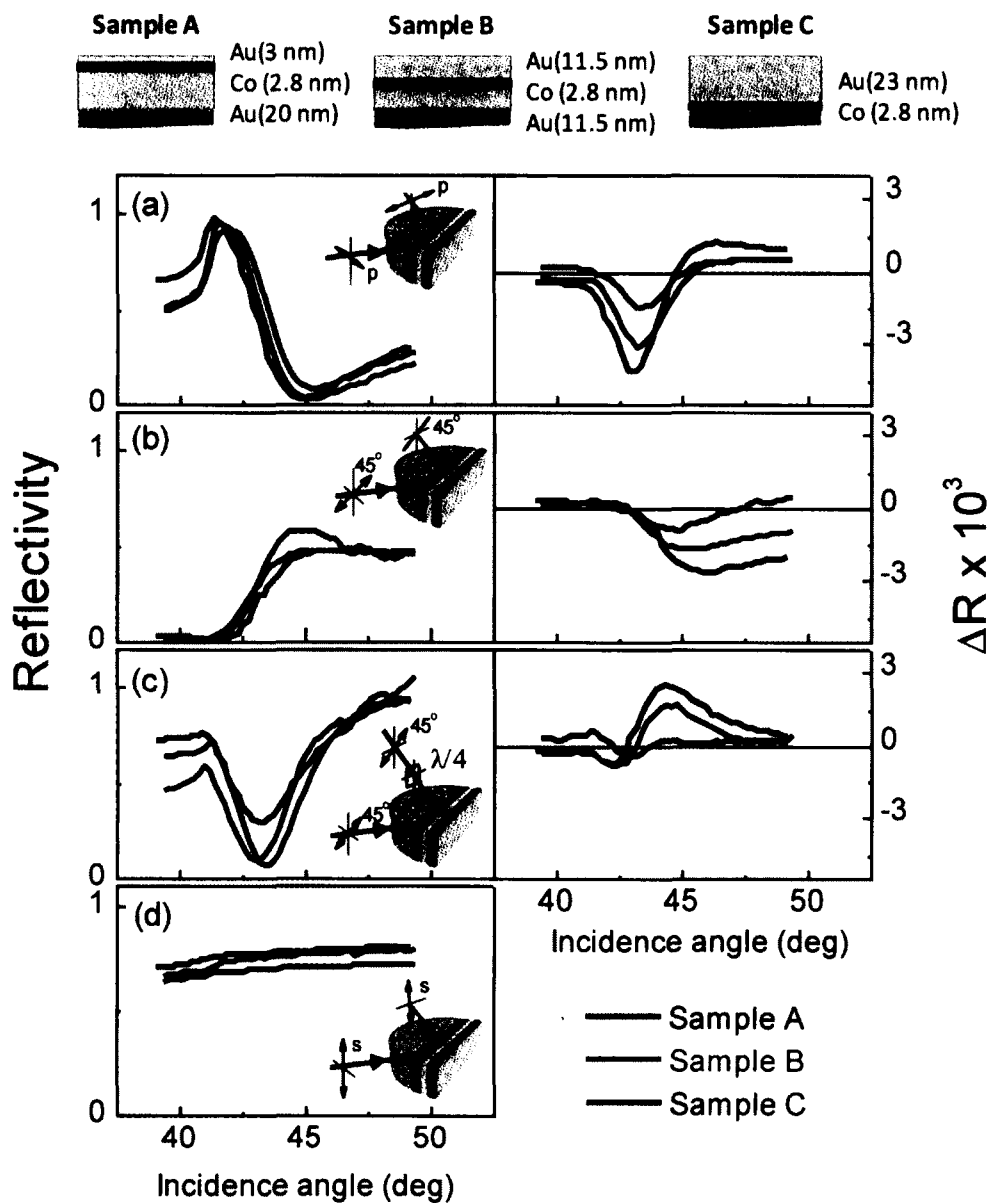


FIG. 4.6: Variation with the incidence angle of the reflectivity (left column) and MO response (right column) for the Au/Co/Au trilayers with Co positioned at 3 nm (up), 11.5 nm (middle) and 23 nm (down) to the upper air-Au interface using (a) p-polarized light, (b) light rotated 45° from the s (and p) axis and a polarization analyzer oriented at 45°, (c) same as (b) but inserting a quarter wave plate with its fast axis along p and (d) using s-polarized light.

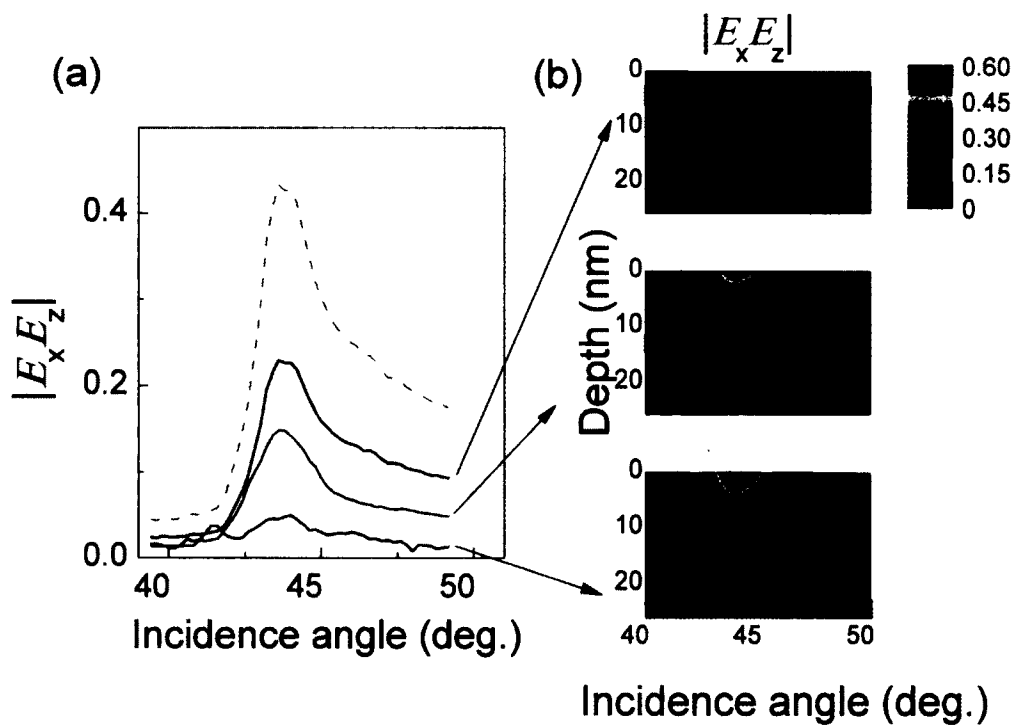


FIG. 4.7: (a) Modulus of the product of the TM electric components $E_x E_z$ normalized to the incident intensity at the position in which the ferromagnetic film is placed in each case for the Au/Co/Au trilayers with Co positioned at 3 nm (up), 11.5 nm (middle) and 23 nm (down) to the upper Au-air interface. The dashed line represents the estimated value of $E_x E_z$ at the air-metal interface. (b) $E_x E_z$ is represented as a function of incidence angle and distance to the upper Au-air interface.

4.4 Conclusions

We have demonstrated that it is experimentally possible to achieve SPP modes in tailored Au/Co/Au trilayers that exhibit large electromagnetic fields that can also be modulated by externally applied magnetic fields. The MO activity, associated with the modification of the k_{sp} , exhibits a strong dependence with the external magnetic fields. By using magneto-optics as a tool, we have analyzed the field-dependent optical response in tailored Au/Co/Au trilayers and have been able to probe the SPP generated electromagnetic fields within the structures, checking them against simulated values calculated using transfer matrix formalism. Our studies are useful for the design of magneto-plasmonic components for varied applications based on leaky modes in SPP excitation.

CHAPTER 5

Magneto-Optics and Magneto-Plasmonics on Au-Co Nanocomposite Thin Films

In this section, the main purpose is utilizing surface plasmon polaritons to generate large electric-magnetic fields of interest in sensor applications.

5.1 Introduction

Most current bio-sensing schemes based on Surface Plasmon Resonance (SPR) are “passive”, i.e. they are based on small changes in the optical properties at the sensor surface - typically gold - when a biological specimen to be detected is bound to it and SPPs are excited. In order to improve sensitivity, it would be highly desirable to develop “active” plasmonic systems such that some optical property can be varied under application of an external field. This design would allow highly sensitive bio-sensing using field modulated detection schemes[45]. We have

explored this option in sensing-elements that include magneto-optically active materials where their magneto-optical properties can be modified by the application of external magnetic fields. Transition metals alone such as Fe, Ni and Co exhibit magneto-optical effects accessible at relatively low fields, but their absorption coefficients are higher than those of Au and therefore their SPPs are over-damped. Thus, composite noble-metal/ferromagnetic-metal sensing elements can overcome the high absorption problem while exhibiting high magneto-optical activity. In fact, it has been observed that multilayer films of Co and Au[62][51] do exhibit enhanced magneto-optical activity related to SPP excitation that can be controlled by an externally applied magnetic field. We have previously studied such layered Co-Au systems and found that (i) the modulated magneto-optical signal is enhanced when the SPP are excited, and (ii) this phenomenon is extremely sensitive to the thickness of the intervening layers. Thus, in order to explore less stringent material designs, we have considered the possibility of using nano-composite AuCo films as magneto-plasmonic sensors. In fact, it is the first time that nano-composite materials have been used for such magneto-plasmonic applications. Since these materials do not form a binary alloy[63], the two metals can form different nanocluster-matrix aggregates depending on their relative concentration and the growth temperature, and thus their magneto-plasmonic properties can also be optimized.

In this work, Co-Au composite films with various Co:Au concentration ratios from 5:95 to 60:40 and grown at temperatures from RT to 600 °C but with fixed total thickness were prepared using magnetron sputtering co-deposition. Optical measurements including ellipsometry and reflectivity in the Krestchmann configuration along with magneto-optical measurements in the transverse Kerr configuration were performed. The optical properties of the films as a function of the microstructure were described using effective medium theory[64]. In addition, a strong enhancement of the magneto-optical activity was observed when SPPs were excited in the

nano-composite films.

5.2 Experiment

The Au-Co nano-composite films were prepared using DC magnetron sputtering co-deposition in an ultra-high vacuum chamber with base pressure in the low 10^{-9} Torr regime. Sputtering deposition was performed simultaneously from high purity (99.99%) Au and Co targets at 5×10^{-3} Torr Ar pressure. Soda lime glass substrates were ultrasonically cleaned in subsequent baths of acetone and methanol for 10 minutes each prior to introduction in the deposition chamber. Before growth, the substrates were UHV annealed at 600°C for 30 minutes to degas and planarize the surface[57]. To improve the deposited film homogeneity the substrates were rotated around the vertical axis at constant speed (12 rpm) during thin film growth. All films were 50 nm thick and were deposited at temperatures ranging from room temperature (RT) and 600°C in order to explore the dependence of the microstructure with the growth temperature. The Co concentration was varied from 5% to 60% by controlling the DC voltage applied to the Co and Au targets during co-deposition. All samples were capped with 3 nm Au films deposited at RT to prevent oxidation of Co.

The surface morphology of the samples was characterized with scanning electron microscopy (SEM, Hitachi 4700 Scanning Electron Microscope with Energy-Dispersive X-Ray Spectroscopy). The microstructure of the samples was investigated using scanning transmission electron microscopy (STEM)[65]. The specimens were observed with a VG Microscope HB501UX operated at 100 kV and equipped with a Nion 3rd-order aberration corrector and a Gatan Enfina electron energy loss spectrometer capable of providing atomic resolution in both imaging and spectroscopy[66][67][68]. Specimens for STEM observations were prepared by



FIG. 5.1: Illustration for Au:Co co-deposition

conventional thinning, grinding, dimpling and Ar ion milling. Principal component analysis (PCA) was applied to the EELS images to remove random noise[69].

Magnetic measurements carried out with a Superconducting Quantum Interference Device (SQUID) indicated in-plane anisotropy in all cases, and that the magnetic moment in the samples correlated with the full amount of Co present. Variable angle spectroscopic ellipsometry was measured using an M-44 VASE J. A. Woollam Co. instrument, to determine the actual optical constants for the Au-Co nano-composite films in the spectral range from 1.5 to 3 eV. The optical and MO response of the multilayers under SPP excitation were investigated in the Kretschmann[70] configuration using p-polarized He-Ne laser radiation ($\lambda = 632.8$ nm). In this configuration, the glass substrate is coupled to a semi-cylindrical glass prism by a matching refractive index liquid. In our experimental setup the prism was mounted on an automated goniometer allowing illumination in total internal reflection and variable incidence angle θ with a resolution of 10^{-4} degrees. A Si am-

plified photodetector preceded by a p-oriented polarizer was used to detect intensity variations in the reflected radiation. The transverse MOKE was also investigated by applying a magnetic field $H = 30$ mT alternating magnetic field (60 Hz) in the plane of the sample and perpendicular to the incidence plane, intense enough to saturate the Co films with in-plane magnetization. The MO signal, i.e. the intensity variation of the p-polarized reflected light at the modulation frequency, was investigated in transverse geometry, i.e. field applied in the plane of the sample but normal to the light incidence plane and detected and analyzed using lock-in techniques.

5.3 Results and Discussion

5.3.1 Morphology and Microstructure

As previously mentioned, Co and Au do not form a binary alloy and therefore two separate phases co-exist in the films[37], i.e. a matrix with a cluster distribution. The size distribution of the various clusters is critical to the optical and MO behavior. We have used SEM and STEM to investigate the surface morphology and film microstructure.

In Fig.5.2 the SEM images for films with Co:Au concentration ratio of 50:50 and deposited at temperatures ranging from RT to 600 °C are depicted. At RT, the surface exhibits low roughness, increasing gradually with the deposition temperature. At 600°C , the surface becomes significantly rougher, exhibiting separate three-dimensional grains with no specific orientation. The average diameter of the observed clusters is of 150 and 500 nm and 2.5 microns for the samples grown at RT, 300°C and 600°C respectively.

Fig.5.3 shows Z-contrast images along with Co compositional maps obtained from EELS for two of the samples, namely Co 5% Au 95% deposited at 300°C and Co

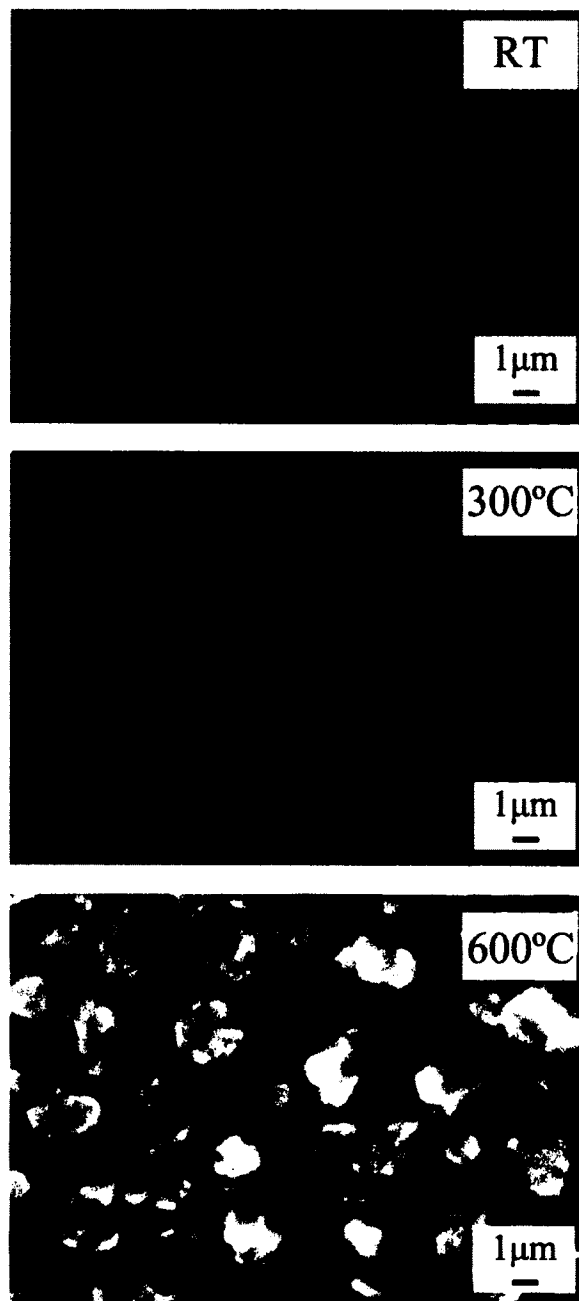


FIG. 5.2: SEM image for 50 nm thick Co:Au films with a concentration ratio of 50:50 and grown at RT, 300°C and 600°C respectively. This work was carried out at ORNL by our collaborator M. Varela.

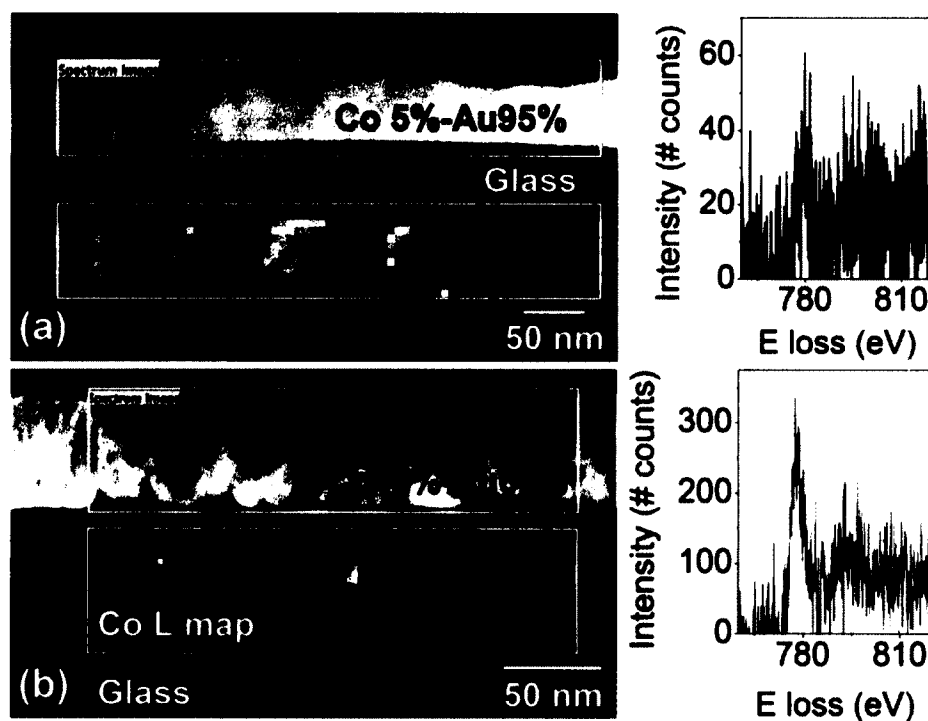


FIG. 5.3: STEM Z-contrast images, EEL spectra and Co composition maps based on EELS/STEM (insets) for two nano-composite samples. (a) Sample grown at 300 °C with Co 5% Au 95% and EELS spectrum. The white rectangle shows the region where an EELS spectrum image of 71 x 12 pixels in size was acquired. Inset: STEM Co compositional map. (b) STEM Z-contrast image of the sample grown at 600 °C with Co 40% Au 60% and EELS spectrum. The white rectangle shows the region where an EELS spectrum image of 80 x 20 pixels in size was acquired. Inset: Co compositional map. The right panels show single pixel EEL spectra corresponding to the Co $L_{2,3}$ edge after background subtraction for both samples (the acquisition time was 1 s per pixel). PCA was applied to remove random noise to the spectrum image in (a). The Co maps were obtained through spectrum imaging after subtracting the background using a power law fit and integrating a window 20 eV wide below the Co $L_{2,3}$ edge around 779 eV. Note: The grayscale on both Co maps are not the same.

40% Au 60% deposited at 600°C . Even for the diluted sample (5% Co), a clear Co signal is observed in the EEL spectra [see Fig.5.3(a)], allowing compositional maps to be produced. The image shows homogeneous distribution of Co in this film, so any clustering present occurs below the length scale of the STEM resolution. For the samples grown at 600°C , on the other hand, Au and Co segregate forming clear grains in both the perpendicular and lateral directions.

Our observations are compatible with those by Mader et al. on Co-Au thin films[63]. They observed that when heating the substrate at 200°C an irreversible transformation from amorphous to a metastable FCC crystalline phase occurred that subsequently decomposed into equilibrium phases above 277°C , leading clearly to segregated micro-structure. This can be understood considering that at lower temperature, the adatoms freeze in places close to their points of impingement on the surface, and form close packed “crystalline” particles, while as the surface mobility increases at higher temperatures, atoms’ diffuse for longer distances such that they can form separate phases. We note that the two randomly mixed components do not form clusters of the same size because of the different atoms diffusion energies. Thus, there is a balance between the random cluster distribution and their ability to fill the available space in the film. In our case, the SEM images and STEM maps also indicated that at RT, the lowest substrate temperature tried, an amorphous metastable structure can exist that separates into distinct aggregate phases at higher deposition temperature.

5.3.2 Optical and Magneto-Optical Characterization

In order to further understand the optical and magneto-optical response generated from the Au-Co nanocomposite thin films, we use the general transfer matrix formalism to simulate the ellipsometric properties[36].

Ellipsometric Measurement

The optical constants for the Au-Co composite films were measured with ellipsometry in the spectral range from 1.4 and 3 eV. Fig.5.4 shows the refractive index (n) and absorption coefficient (k) for the different films, along with the bulk values for Au and Co. In order to understand the evolution of the optical constants as a function of the Co concentration and morphology, effective medium calculations were carried out. Two fundamental approximations can be made depending on the reference tensor ϵ_0 used in the effective medium calculation: the Bruggeman and Maxwell-Garnett (MG) approximations[71]. In the Bruggeman approximation the reference dielectric tensor ϵ_0 is considered the final effective medium tensor and then, following a self-consistent computation process, no distinction is made between the matrix material and the nano-cluster material. Thus, this approximation should be used to treat systems where no clear assignment of which component is the matrix material and which the host can be done. On the other hand, in the Maxwell-Garnett approximation the matrix material determines the choice of the reference dielectric tensor as this one is taken equal to that of the matrix. Thus, it is more appropriate to treat systems using this formalism when adequate assignment of the matrix material is possible. As shown in Fig.5.4 at lower Co concentration, the MG method and Bruggeman methods yield similar results whereas larger discrepancies are found at higher Co concentration. Good agreement is found between the experimental values measured in Au-Co films grown at 300 °C and the Bruggeman model for all the temperatures studied, indicating a good segregation of Co and an homogeneous distribution in the Au matrix for this growth temperature. Neither model works for the samples grown 600 °C since, as previously shown, the size of the observed clusters exceeds the wavelength range investigated, and thus the effective medium approximation is not valid.

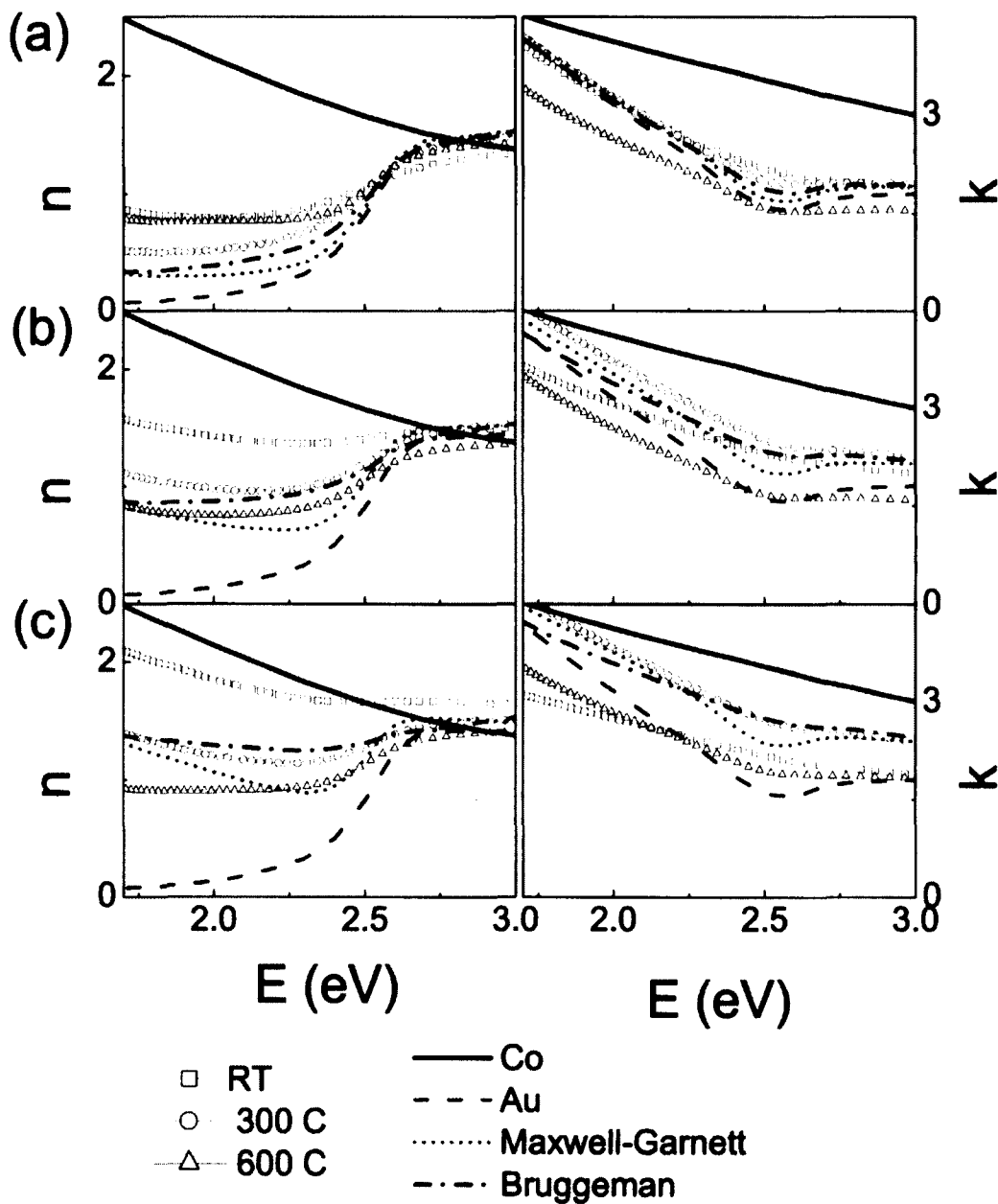


FIG. 5.4: Optical constants (left column: n , right column: k) for Co:Au nano-composite films with composition ratio of (a) 10:90, (b) 30:70 and (c) 50:50. The optical constants of bulk Co and Au are plotted for comparison, along with the optical constants for nano-composite films with identical concentrations calculated using Maxwell-Garnett and Bruggeman effective medium approximations.

In order to understand the dependence of the optical constants with the microstructure of the films we consider the electric behaviour of these materials. In general, an amorphous nano-composite film has a significant number of defects leading to higher electric resistivity than a denser film. Using the classical Drude model, the AC conductivity can be written as:

$$\sigma(\omega) = \frac{\sigma_0}{1 + i\omega\tau} \quad (5.1)$$

in which σ_0 is the DC conductivity, ω is the angular frequency of electric field, and τ is the average time between collisions. Thus, the dielectric constant can be written as:

$$\epsilon_r(\omega) = 1 + \frac{i\epsilon(\omega)}{\epsilon_0\omega} \quad (5.2)$$

when τ is smaller than the bulk value, which is achievable when the mean free path of the electron is small as would be the case for an amorphous film with many scattering centers[63], then the changes in the dielectric constant lead to an increased n value with respect to bulk as we observe.

Reflectivity measurements in the Krestchmann configuration as a function of incident angle for the various Au-Co films with different Co concentration and growth temperatures are shown in Fig.5.5 along with simulations using the transfer matrix formalism[36] and the experimental optical constants.

Both the theoretical calculations and the experimental data in Fig.5.5 show that as the Au concentration decreases the reflectivity minimum shifts to higher values of incident angle. As expected, the nano-composite films do not exhibit as sharp as reflectivity minimum compared to pure Au films due to the higher absorption of Co. Thus, we notice that the minimum in reflectivity broadens when the Co concentration is increased, consistent with the stronger absorption of Co.

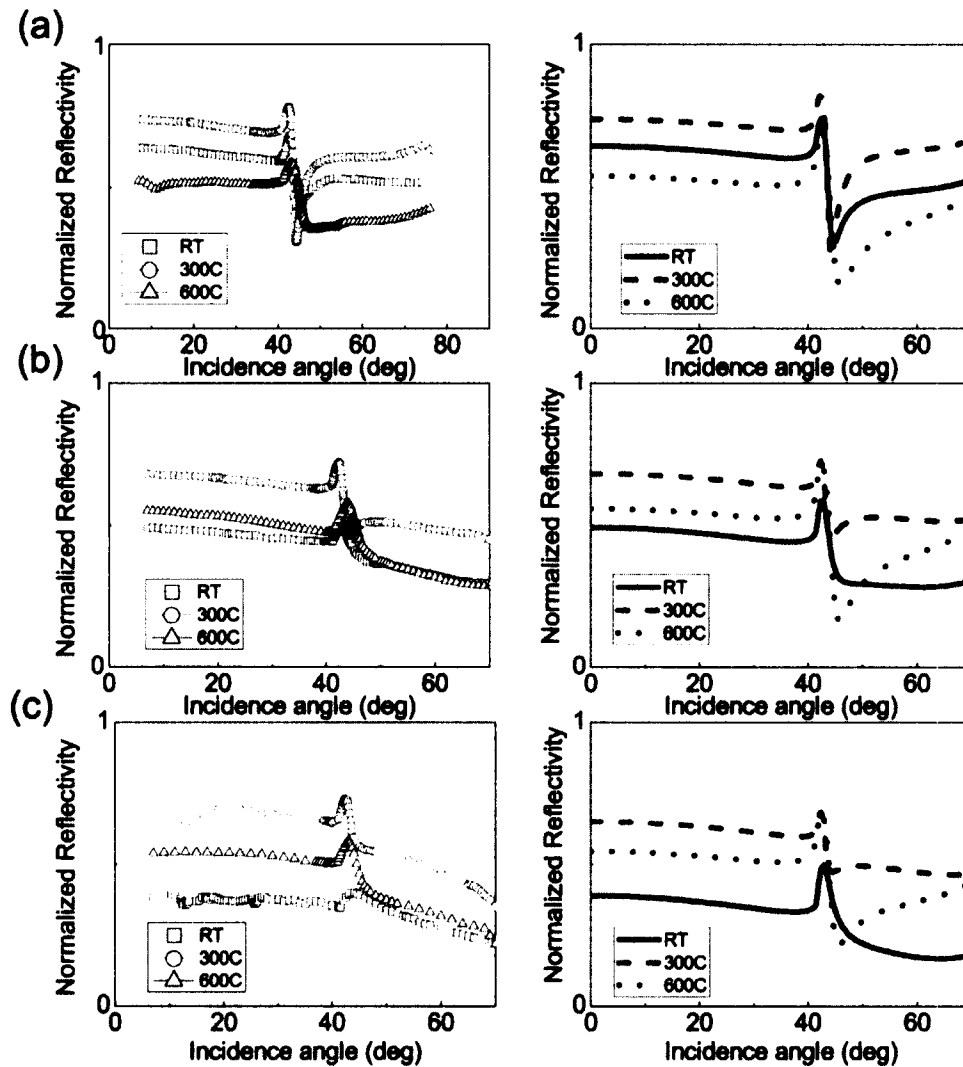


FIG. 5.5: Angular dependence of the reflectivity in the Kretschmann configuration for Co-Au nano-composite films grown at RT, 300°C and 600°C with concentration ratios of (a) 10:90, (b) 30:70 and (c) 50:50. Experimental data are shown in the left column whereas simulations are shown in the right column.

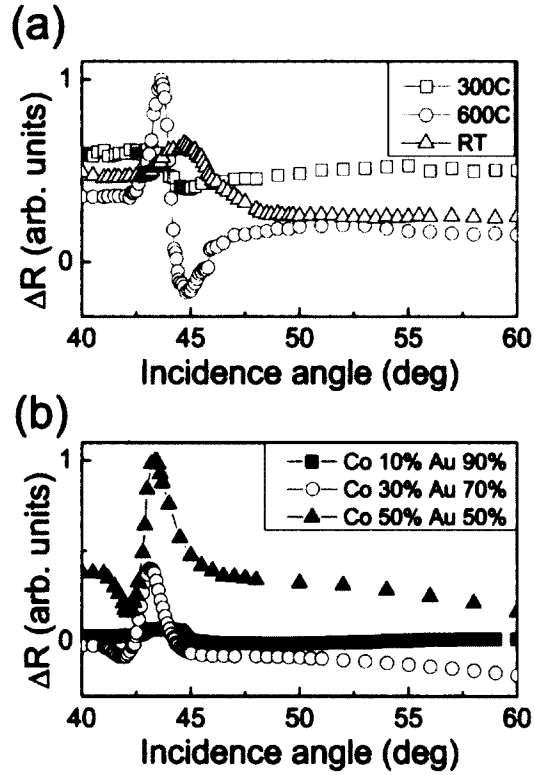


FIG. 5.6: Angular dependence of the Magneto-Optical Kerr Effect in the transversal configuration Eq.5.3 $\Delta R = R(H^+) - R(H^-)$ for (a) Co:Au nano-composite films with concentration ratio of 10:90 and grown at different temperatures and (b) nano-composite films grown at 300 °C with different Co concentrations.

We note that the experimental reflectivity curves and thus the SPP excitation in the nano-composite films also depends on their microstructures. Simulations carried out using experimental optical constants agree well with the experimental data for the samples deposited at RT and at 300°C. The distinct 3D microstructure observed in the 600°C sample hinders SPP propagation and thus makes any simulations meaningless in this case.

Magneto-Optical Measurement

We expect that optimal excitation of SPP in these nano-composite films should lead to enhanced magneto-optical effects, since these depend on the actual electromagnetic fields near the magnetic components[52][53]. The curves shown in Fig.5.6 illustrate the transverse Magneto-Optical Kerr Effect measured in the Kretschmann configuration for the composite films, given by the magnetic field induced change of the reflectivity between the two opposite external magnetic field orientations:

$$\Delta R = R(H^+) - R(H^-) \quad (5.3)$$

Fig.5.6 (a) shows ΔR for films with a Co:Au concentration ratio of 10:90 grown at RT, 300 and 600°C . We observe maximum magneto-optical effect in the samples grown at 300°C , for which optimum segregation of Co in the Au matrix was inferred by the optical measurements. Fig.5.6 (b) shows ΔR for the films grown at the optimum temperature 300°C and with different concentration ratios. Higher magneto-optical response is obtained for the films exhibiting a higher concentration of Co. We also notice that unlike the field-independent reflectivity, the field modulated reflectivity keeps a narrow angular resolution at resonance, which is of interest in the design of magneto-plasmonic sensors for field-modulated sensing schemes.

5.4 Conclusions

We find that the samples grown at 300°C , which exhibit segregate nano-cluster microstructure and smooth surfaces capable of SPP propagation, exhibit larger MO effects than the samples grown at lower and higher temperatures, as expected from our discussion on the correlation between SPR excitation and microstructure. We also note that the MO activity also increases with increasing Co concentration con-

sistent with the presence of more magnetic material in the films, while the angular resolution of the field-dependent change of the reflectivity at resonance is somewhat insensitive to the amount of Co present. Our studies open up new possibilities for optimizing nano-composite materials that combine suitable properties, i.e. optical and magnetic, for applications that benefit from modulated sensing schemes, such as novel sensors based on SPR technology.

CHAPTER 6

Magneto-Transport and Non-Linear Magneto-Optics Correlations

6.1 Introduction

Plasmon resonance can lead to the amplification of the local field within or close to plasmonic structures resulting in the enhancement of linear and nonlinear optical processes[72]. For example, it has recently been reported that the direction of magnetization can be tracked by surface plasmons through magnetization-induced second harmonic generation (SHG) in chiral nickel microstructures[73], due to the sensitivity of SHG to probe buried interfaces where inversion symmetry-breaking at the interfaces occurs. On the other hand, anomalous linear Magneto-Optic Kerr Effect (MOKE) due to excitation of localized and/or propagating plasmonic modes has been reported in various composite systems such as Au/Co/Au multilayers[74], core-shell Ag-Fe[75] and Au-maghemite nanoparticles[76], and Co or Au/Fe garnet

films perforated with holes[77][41], to name a few. Nanocomposite materials can also exhibit interesting magnetic and magneto-transport properties; for example Skumryev et al.[78] prepared a novel class of nanoparticle-matrix materials exhibiting novel exchange bias properties. Thus, it is important to investigate correlations between magneto-optical and magneto-transport properties on nanostructured materials.

Nonlinear Magneto-Optical Kerr Effect (NOMOKE) under optical second-harmonic generation (SHG) in the presence of a DC magnetic field has also been observed in various magnetic systems, such as atomically clean surfaces[79], thin films[80] and nanocomposite films also exhibiting giant magneto-resistance (GMR)[81][82]. These findings have inspired our present work on the correlation between non-linear magneto-optics/magneto-plasmonics, and magneto-transport properties on Au-Co nanocomposite thin films.

6.2 Experiments

6.2.1 Deposition Conditions

Since the Au-Co binary system is a typical phase-separation system[83], it enables deposition of nanocomposite films where the Co content as well as cluster size can be tailored via adequate deposition conditions[84]. Thus, Au-Co nanocomposite thin films were co-deposited from high purity (99.99%) Au and Co targets using DC magnetron sputtering in an ultra-high vacuum (UHV) chamber with base pressure in the low 10^{-9} Torr regime. Soda lime glass substrates were introduced into the UHV chamber after ultrasonic cleaning in subsequent baths of acetone and methanol for 10 minutes. Prior to deposition, the substrates were UHV annealed at 600°C . The substrates were rotated azimuthally at constant speed (12 rpm) to

optimize film homogeneity. All the samples in this study had a total thickness of 50 nm while the Au-Co composition was varied from 10% to 58% Co content. The deposition temperature was kept at 300°C since in our previous study[84] contrast images along with compositional maps obtained from EELS indicated that the Co and Au species segregate in films with higher Co concentration as well as higher deposition temperature, thus showing that 300°C is an optimal growth temperature for the present studies. All samples were capped with 3 nm Au films grown at RT to prevent Co oxidation after removal from the UHV chamber. The relative composition of Au and Co was achieved based upon well-calibrated Au and Co deposition rates.

6.2.2 Crystallinity Analysis—X-Ray Diffraction Measurement

The microstructure of the films was determined *ex-situ* by carrying X-ray diffraction (XRD) scans.

X-ray diffraction measurement data shown in Fig.6.1 illustrate the correlation between the Au-Co films' microstructure and the deposition temperature. We note that the Au (111) reflection exists in all samples regardless of concentration and growth temperature, but at room temperature (RT), we note a trend in the Au (111) reflection, since its full-width at half maximum (FWHM) decreases with Co content. This is in contrast with samples deposited at higher temperature, where the Au (111) peak does not change significantly with increased Co concentration. For the films grown at 600°C a weaker Au (200) peak can also be observed. In particular, the Co 50% Au 50% RT sample reveals a Co (100) peak with hexagonal close-pack (hcp) structure. These results can be qualitatively understood considering phase separation processes where the room temperature grown films tend to form a mixed

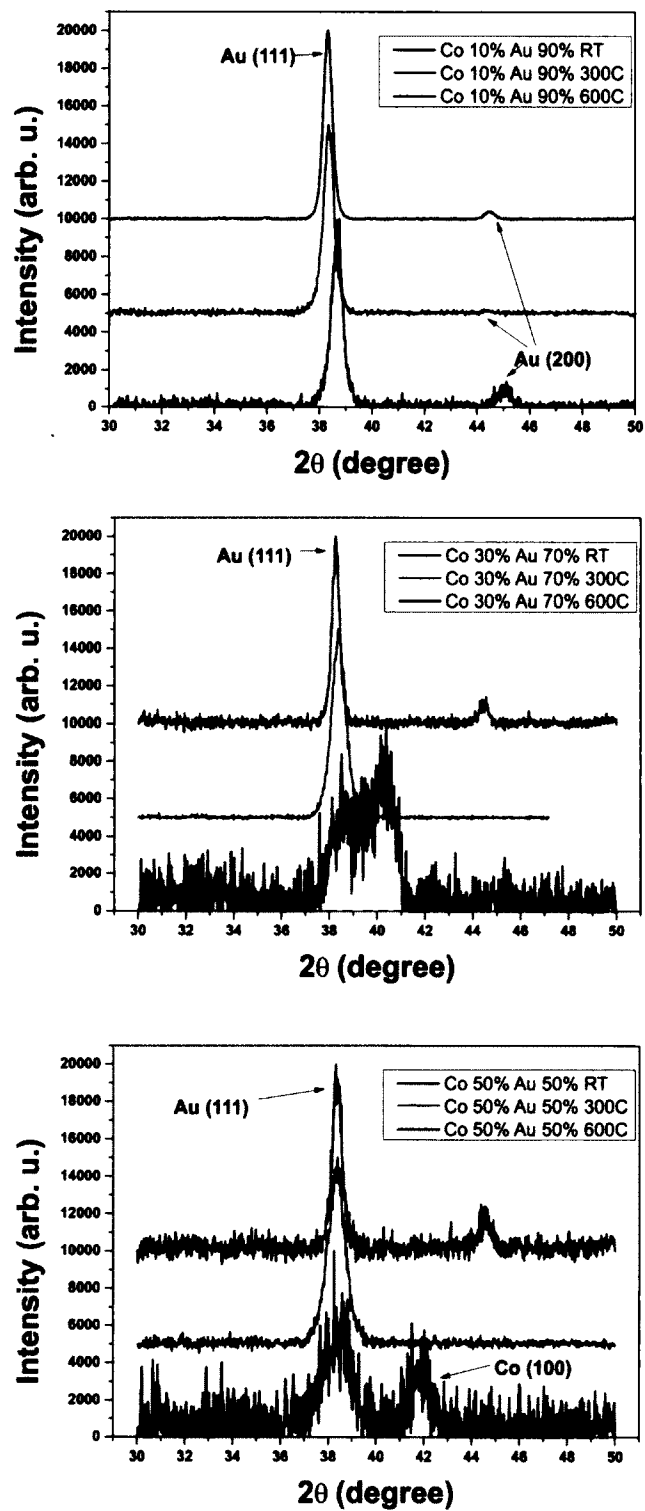


FIG. 6.1: Theta-2Theta XRD scans on composite Au-Co thin films with varied Co:Au composition; Top: Co 10% Au 90%; Center: Co 30% Au 70%; Bottom: Co 50% Au 50%

phase of Au and Co at atomic scale[84] since the Au-Co system does not tend to form a binary alloy[63].

In our previous study[84] on this same composite system, we observed that the Co and Au species segregate into grains in those films with higher Co concentration as well as higher deposition temperature. Our observations were based on contrast images along with chemical composition maps obtained from EELS. It should be noted that the Co 50% Au 50% deposited at room temperature sample is the only one exhibiting hcp Co (100) peak. For higher deposition temperatures, both Co and Au atoms have more energy to segregate and diffuse in both horizontal and vertical directions, which was also observed in the EELS chemical composition maps.

Lattice Constant and Domain Size

The bulk values of the lattice spacing of Co (111) is 2.16\AA while Au(111) and Au (200) is correspondingly 2.03\AA and 2.35\AA . For films grown at higher temperature, we notice a trend where the Au lattice relaxes bringing the lattice spacing closer to bulk value while we also note that samples grown at room temperature exhibit strain. Our XRD measurements suggest that Co, which has hcp structure in bulk form, acquires a meta-stable fcc structure at high Au concentration or high growth temperature. At room temperature, the Co 50% Au 50% thin film, which exhibits two distinct and separate Au fcc (111) peaks and Co hcp (100), also shows similar grain size as calculated from the Scherrer equation, namely 9.27 nm and 11.99 nm for Au and Co respectively. As the Co concentration decreases, the trend observed is that the Co peak approaches the Au (111) peak, due to strain arising from lattice mismatch. Fig.6.2 indicates that the average grain size decreases with the introduction of Co in the samples grown at lower temperature (RT and 300°C). This indicates that Co is inserted as an impurity in the Au matrix. For higher Co concentration, there is more strain due to lattice mismatch and heat treatments

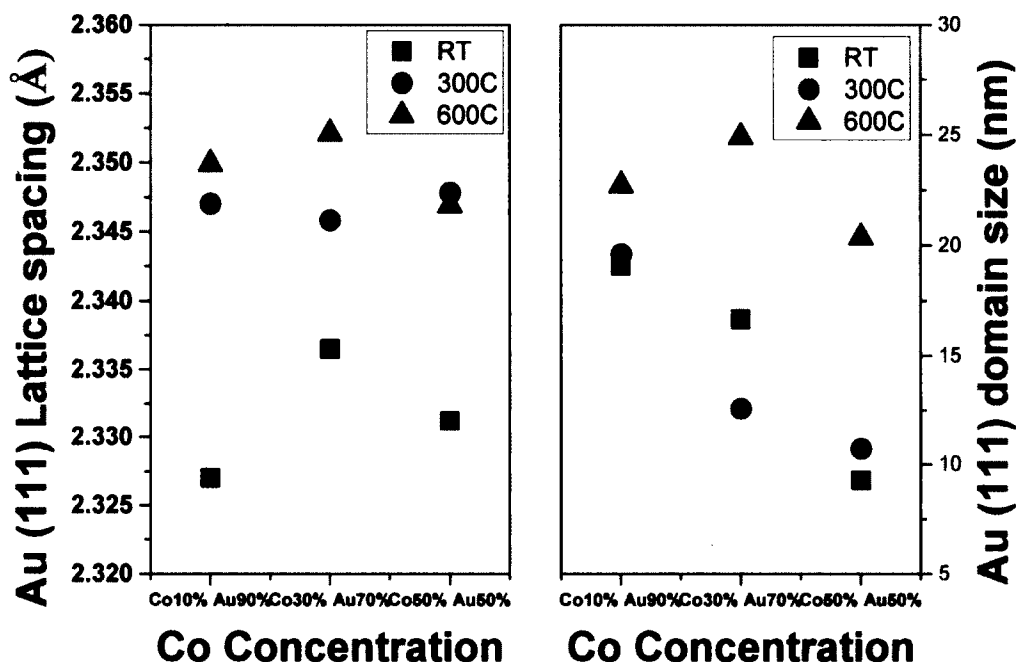


FIG. 6.2: Lattice constant and domain size analysis on composite Au-Co thin films

have a greater effect on grain size. We note that the average grain size enlargement is around 20% for a sample with 10% Co content compared with 100% for the sample with 50% Co content. We also note that the as-deposited Au-Co nanocomposite films with higher Co concentration retained cobalt's hcp structure.

We postulate that as the temperature is increased, interfacial stress is relieved and, combined with different diffusion rates for both species, leads to more diverse grain sizes. Thus, the higher temperature deposition Au-Co nanocomposite thin films have much different Au or Co grain size compared with the samples grown at lower temperature. These results also were observed in the EELS chemical map and SEM images[84]. It should be emphasized that the lattice spacing for the samples grown at 300°C and 600°C are very close, indicating that stress present might be relaxed but the domain sizes of 300°C samples are much smaller compared to 600°C samples due to diffusion processes. As a result, the 300°C grown samples yield considerably smoother surfaces.

6.2.3 Magnetic Hysteresis Measurements

Ferromagnetic thin film hysteresis loops were measured using a superconducting quantum interference device (SQUID) magnetometry. In Fig.6.3(Center), the 300°C grown thin film, the out-of-plane (easy axis) and in-plane (hard axis) M-H loops were measured. We note that the magnetization correlates well with Co concentration, x , and we also notice that the saturation field decreases with increased Co content, indicating that onset of percolation in samples with higher Co content occurs approximately around $x = 40\%$.

In Fig.6.3, except for the RT Co 10% Au 90% film, all films exhibit out-of-plane anisotropy. Co 10% Au 90% also shows paramagnetic behavior at room temperature as expected for small Co cluster size.

6.2.4 Magneto-Transport Measurements

As previously discussed in Page.44, magneto-transport measurements were carried out using the four-point probe method. The magneto-resistance was measured at room temperature with the current-in-plane configuration (CIP), applying an external DC magnetic field parallel to the surface of the samples while current was also applied in the plane of the samples and perpendicular to the external magnetic field. A programmable triggered function was used to minimize measurement errors by recording the corresponding voltage at a preselected time once the current was applied. In this section, all the magneto-transport properties are measured at Room Temperature (300K), in order to compare results obtained from the angular-dependent MOKE previously discussed on Page.78.

The magneto-resistance data for Au-Co nanocomposite films with varied Co composition is shown in Fig.6.4.

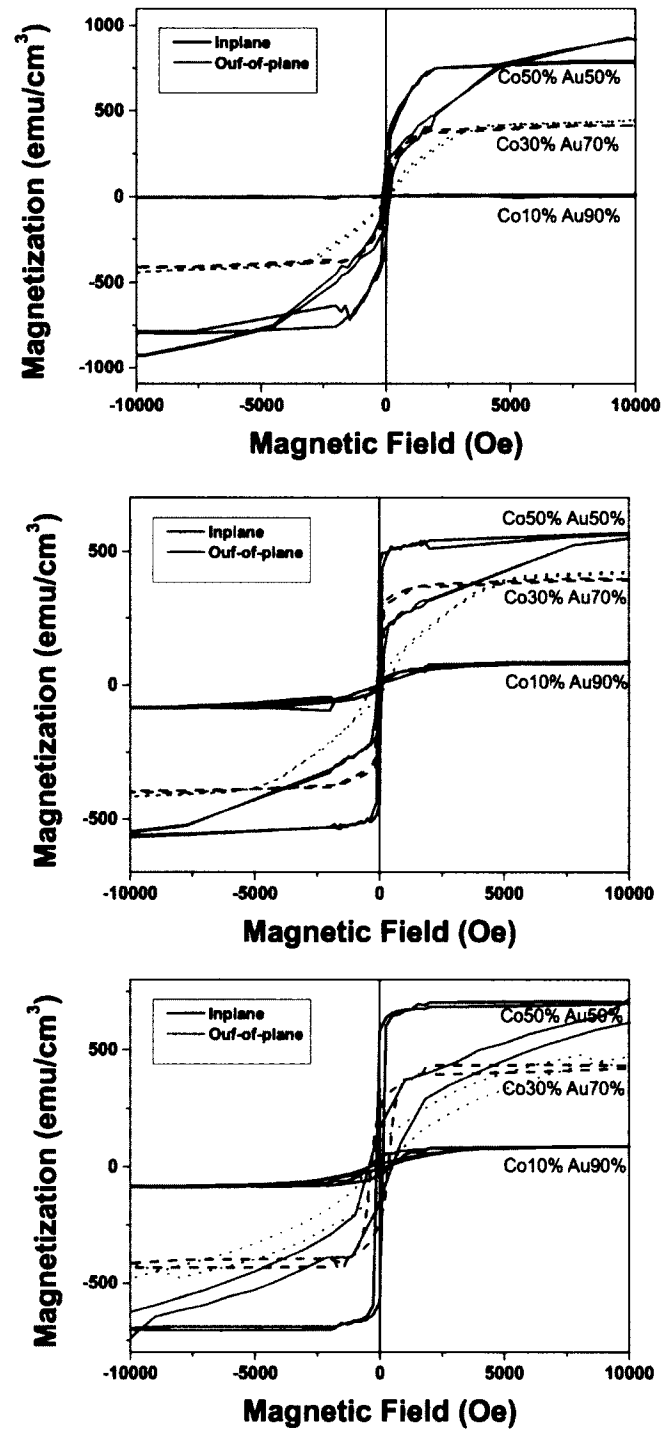


FIG. 6.3: Hysteresis loops obtained using SQUID magnetometry for selected nanocomposite films with different Co concentration and deposition temperatures; Top: Room Temperature; Center: 300°C ; Bottom: 600°C .

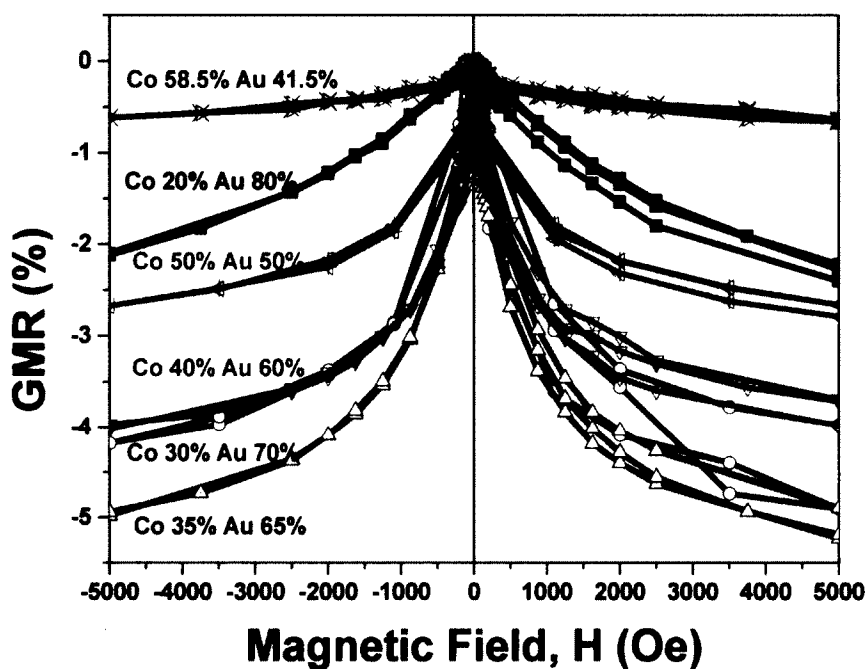


FIG. 6.4: RT magneto-resistance data vs applied magnetic field for nanocomposite thin films with the composition indicated

6.2.5 Non-Linear Magneto-Optical (NOMOKE) Measurement

We also carried out non-linear magneto-optical (NOMOKE) studies on these Au-Co nanocomposite samples in order to investigate the correlation between NOMOKE and GMR since such correlation has previously been reported in Co-Ag granular films[3].

SHG NOMOKE Experiment

The SHG nonlinear-optical studies were performed using a Ti:sapphire laser operating at a wavelength of 800 nm and average power of 200 mW at Dr. T. Murzina's laboratory at Moscow State University. A 45° incident beam illuminated the sample and the second harmonic (SH) signal generated in reflection from the films was selected by an appropriate set of filters and detected by a photon counter.

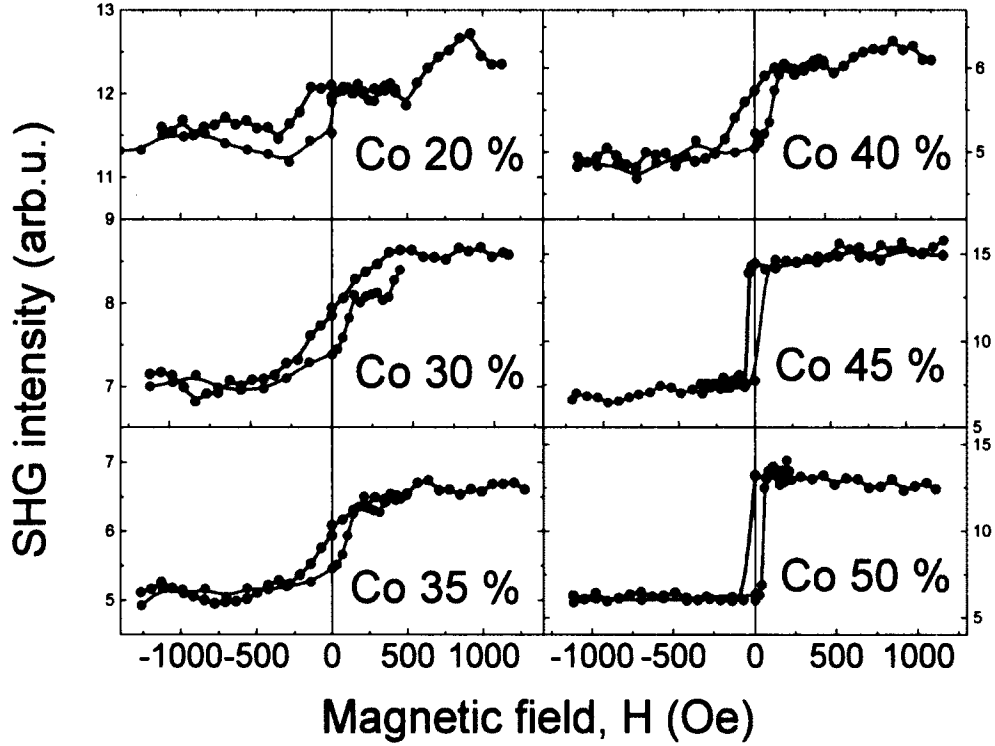


FIG. 6.5: SHG magnetic hysteresis loop as a function of Co concentration

The SH polarization configuration is p-in (for the pump beam) and p-out (for the SH beam). A transversal DC magnetic field up to 3 kOe was applied in the plane of the film for an arbitrary azimuthal orientation of the sample, since no in-plane anisotropy in the SHG signal was observed.

The NOMOKE magnetic contrast is defined as:

$$\frac{I_{2\omega}(+H) - I_{2\omega}(-H)}{I_{2\omega}(+H) + I_{2\omega}(-H)} \quad (6.1)$$

With the SHG intensities $I_{2\omega}(+H)$ measured at opposite directions of the DC magnetic field H .

The SHG magnetic properties are measured at room temperature (RT), to

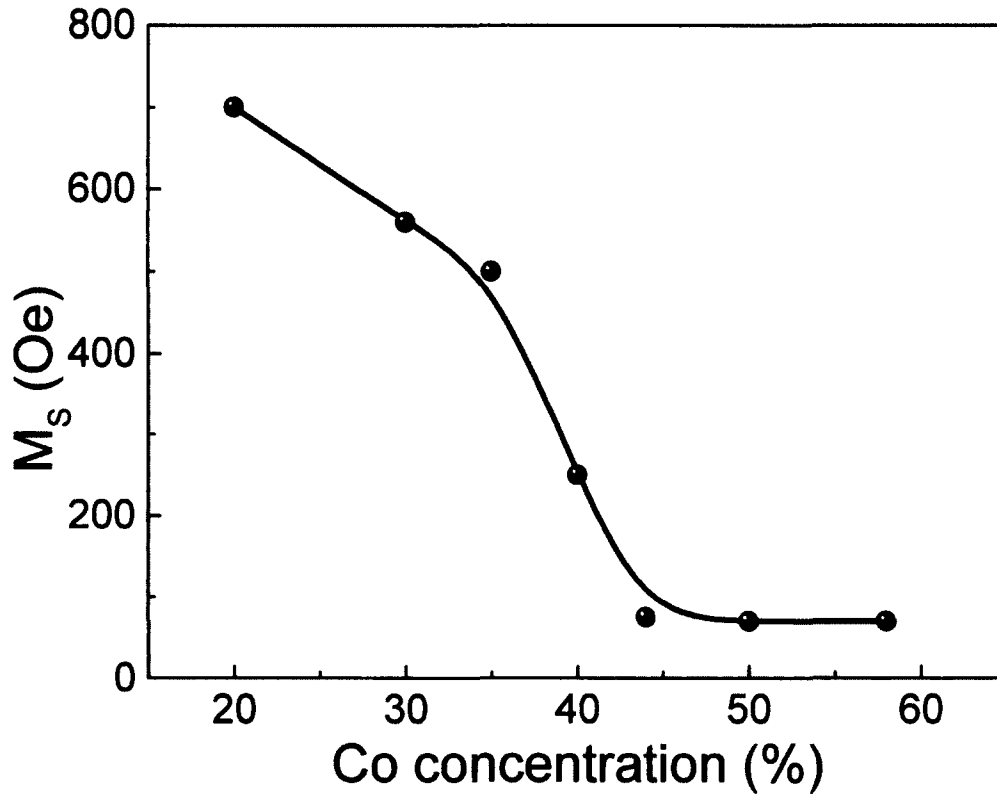


FIG. 6.6: The corresponding saturation magnetization obtained from the magnetic hysteresis loops as a function of Co content.

compared with MOKE signal.

SHG magnetic hysteresis loops as a function of Co concentration are shown in Figure.6.5. The magnetic hysteresis loops show the evolution from paramagnetic to ferromagnetic behavior as the Co content is increased.

The saturation magnetization extracted from the SHG loops is shown in Fig.6.6 where we note a drastic decrease in saturation magnetization and the onset of ferromagnetic behavior around 40-45% Co content, consistent with our SQUID data.

The second harmonic generation magnetic contrast, i.e. NOMOKE, as a function of Co concentration of our Au-Co nanocomposite thin film samples is compared with the magneto-resistance in Fig.6.7. We include selected SHG hysteresis loops as insets in Fig.6.7 to illustrate the different aggregation state of Co in such samples.

We also show previous reported results[3] on similar Co-Ag samples for comparison.

We note that while the overall SHG signal grows with Co content, a local maximum in the SHG magnetic contrast is observed around 35% of Co content, in agreement with the maximum observed in the magnetoresistance data in these same Au-Co nanocomposite thin films. From the SHG saturation magnetization data vs composition (Fig.6.5, Fig.6.6) we deduce that the composition of the films corresponds to granular-like type of structure for Co content below 40%, while the increase of the SHG magnetic contrast at $x \sim 35\%$ is attributed to percolation accompanied by ferromagnetic order, above 40% of Co content. We note that previous studies on Co-Ag nanocomposite films have shown that a local maximum in the SHG magnetic contrast also correlated well with the GMR maximum at somewhat lower Co content ($\sim 27\%$). In such studies it was also shown that calculated localized Surface Plasmon Resonances (SPRs) associated with this SHG maximum exist within the spectral region of interest thus suggesting their role in the observed enhanced SHG magnetic contrast.

6.3 Discussion

In granular systems with small single-domain entities, the size of the ferromagnetic domains remain unchanged and the external field only rotates the magnetic axes of the particles. In such systems, the rotation towards a complete alignment of all magnetic axes upon application of an external field gradually reduces the magneto-resistance. Previous reports indicate that the size of the magneto-resistive effect in such granular materials depends on spin-dependent scattering as well as the number and size of ferromagnetic entities within the probed volume[85]. In our case, the maximum in GMR near 35% Co content corresponds to the optimum cluster size and inter-granular separation[86][87]. Further, previous results on

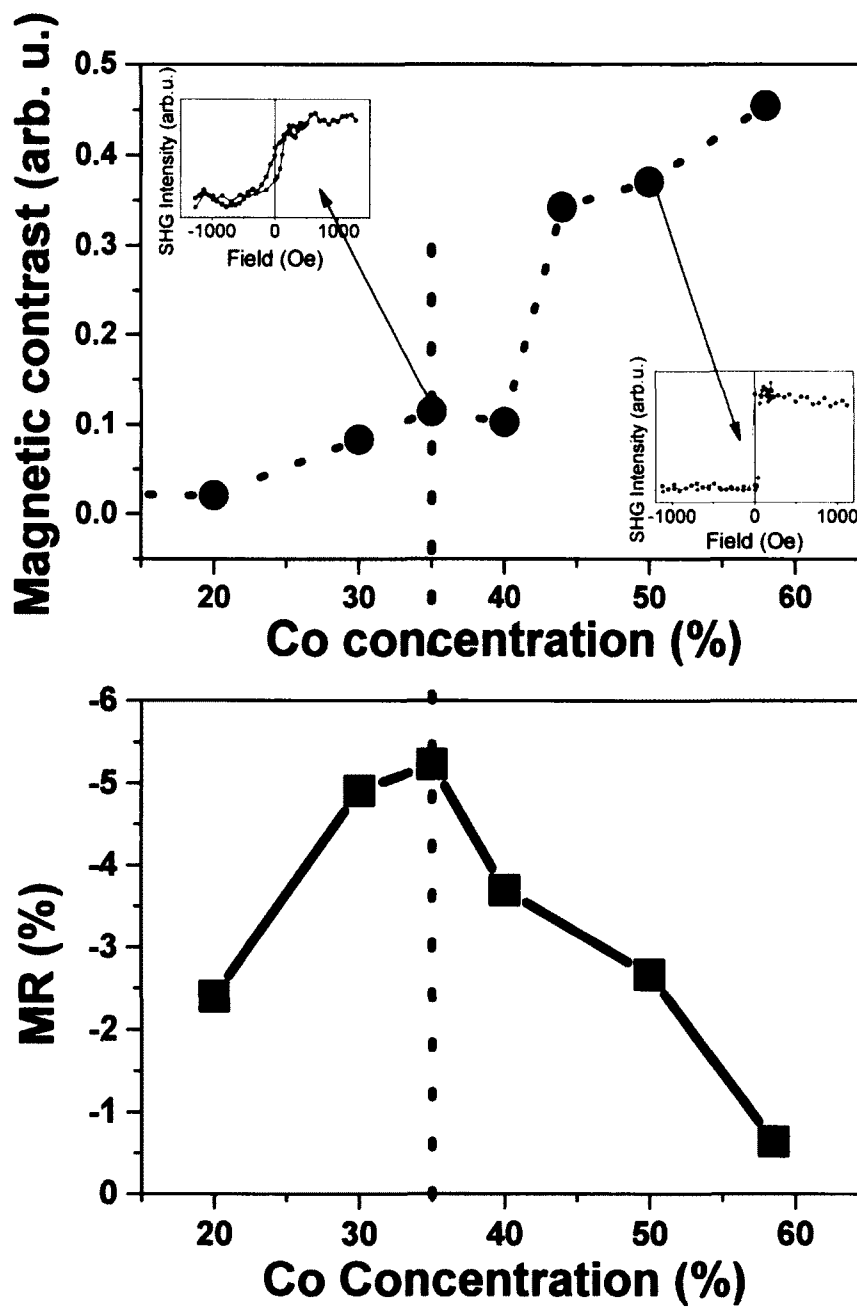


FIG. 6.7: SHG Magnetic contrast (top); magnetoresistance (bottom) vs Co content. The dashed line indicates that the local maximum in NOMOKE correlates well with the GMR maximum. Inset. SHG hysteresis loops for selected samples

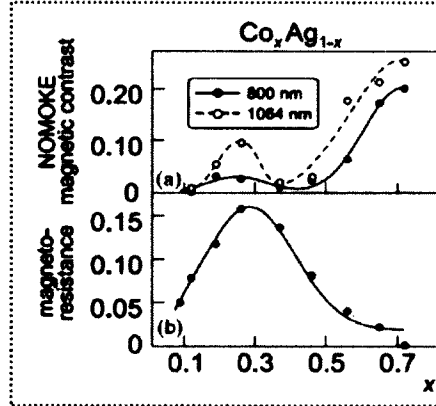


FIG. 6.8: Similar results to those in Fig.6.7 previously reported for Co-Ag granular thin films in Ref.[3]

multilayered Au-Co and Ag-Co films show that optimized GMR values were obtained for similar thickness of the non-magnetic metal (Ag or Au) but lower Co thickness in the Co-Ag case than in the Co-Au case, consistent with the observed dependence on Co concentration in the granular films studied here, compared to the Ag-Co films reported elsewhere[3][88]. We note that our GMR values are also consistent with recent reports where similar nanocomposite thin film samples were prepared using electrochemical methods. In our granular films, the low MR values below 30% Co content can be ascribed to a relatively low concentration of ferromagnetic nanograins, leading to fewer magnetic and non-magnetic interfacial scattering sites, while the decrease in MR values above 45% Co content, above the percolation threshold, seems to be due to the decrease in spin-dependent scattering, which is mainly responsible for the GMR effect[89][90][91].

To understand the correlation between our GMR and NOMOKE data, we note that within the dipole approximation, the optical second harmonic and NOMOKE can originate only from regions of broken symmetry, for example, the surfaces and the interfaces of a centro-symmetric material. Consequently, NOMOKE can probe the local magnetization at surfaces and interfaces[92] where plasmons can

also be present. More specifically, a contrast in the NOMOKE intensity depends on the relative local magnetization in the material[93][94] and on the particular inner structure of the nanocomposite. SHG magnetic contrast enhancements ascribed to localized surface plasmons have been reported in ferromagnetic gratings[95] and granular films[96][3]. Clearly our Au/Co granular nanocomposite films exhibit different interfaces between the magnetic Co clusters and the Au matrix where the coupling between Co nanoclusters depends on their size and separation within the Au matrix[97]. Therefore at 35% Co, just prior to the percolation threshold, we achieved optimized size and inter-granular Co cluster separation, leading to larger magnetic contrast and also larger GMR.

6.4 Conclusion

The microstructure and composition of nanocomposite AuCo thin film samples can be tailored with adequate choice of deposition conditions. We have observed that the ensuing composition of the films affects their non-linear magneto-optical properties as well as the magneto-transport behavior in a correlated manner. The SHG values are affected by interaction between magnetic clusters in granular films and depend on the average distance between clusters. Therefore it is reasonable to expect a correlation between the SHG magnetic contrast and the magneto-resistance, since both the spin-dependent electron scattering that determines the magnitude of the magneto-resistance, and the magnetization induced SHG are driven by the local value of the magnetization. On the other hand, above the percolation threshold, the behavior of the NOMOKE magnetic contrast and that of the magnetoresistance are quite different because the ensuing ferromagnetic ordering leads to a significant increase in the NOMOKE magnetic contrast but suppresses the spin-dependent electron scattering and hence also the magneto-resistance. The detailed nature of this

correlation must be further investigated, combining theoretical approaches previously developed for each of these phenomena in order to provide a more quantitative model for the Co content dependence in our reported experimental GMR and NOMOKE data[98].

CHAPTER 7

Magnetic Sensor Applications

7.1 Co/Pd Ultrathin Multilayer

Introduction

MgO-based magnetic tunnel junctions (MTJs) with perpendicularly magnetized electrodes are key to achieving better spin-transfer-torque (STT)-type random access memories (STT-RAM or spin-RAM). Several candidate materials with perpendicularly magnetized (PM) free-layer structures[99][100] could reduce the switching current I_c and also reach large perpendicular magnetic anisotropy energy K_u with thinner free layer (thickness lower than 2 nm)[100].

In previous reports, Co-based multilayer films have been shown to exhibit large magnetic anisotropy[101]. A promising candidate for the free layer of MgO-based MTJs with perpendicularly magnetized electrodes (p-MgO-MTJs) is Co-based multilayer film, such as $[\text{Co}/\text{Pt}]_n$ and $[\text{Co}/\text{Pd}]_n$ alternating multilayers. In a previous work on Co-based PM multilayers, Co layers with 0.1 nm thickness and Pt or Pd layers with approximately 1 nm thickness were alternately deposited[100][102][103][104]. These Co-based multilayer films exhibited large K_u (up to 10^7 ergs/cm³) due to large

interfacial magnetic anisotropy. However, relatively thick Pt (or Pd) layers made it almost impossible to reduce the free-layer thickness to about 2 nm. From the theoretical calculation, the switching current I_c is proportional to the free layer thickness[105] and the free layer should be very thin to allow small switching current I_c . Thus, a relatively large Pt (or Pd) thickness hindered further application. An alternating Co/Pd multilayer with monoatomic-thickness is a preferred candidate because, in principle, post-annealing may favor the formation of ordered phases with adequate magnetic anisotropy[106]. In fact the idea here is to mimic these ordered phases on substrates and seed layers compatible with industrial STT-RAM fabrication processes.

In a recent study[107], researchers have explored such Co/Pt and Co/Pd multilayers. These multilayers could be regarded as artificial superlattices due to extremely thin thickness. The precise thickness control in these Co/Pd multilayers enable the analysis with atomic thickness(0.2 nm). They observed significant K_u for samples with 3 and 6 Co/Pd repeats. The foreseeable technical problem is that, despite the possibility of self-assembled $L1_0$ superlattices[108][109], during the fabrication of Co/Pd monoatomic artificial superlattices, the thin film deposition process may develop interfacial roughness during growth in the same length-scale range as the sub-monolayer thickness. Defects at interfaces can propagate, strongly affecting the roughness of subsequent interfaces and thus the overall magnetic behavior.

Ultrathin Co/Pd multilayer's interfaces can thus pose a problem since the thickness of the Co and Pd layers are tailored to be about monoatomic or smaller. A well-defined and atomically flat interface may not be possible if increased roughness develops and therefore the integrity of the multilayer is compromised. Thus, our study on the correlation between nanostructure and magnetic properties for multiple surface/interface related parameters for samples grown on realistic substrates and seed layers is presented.

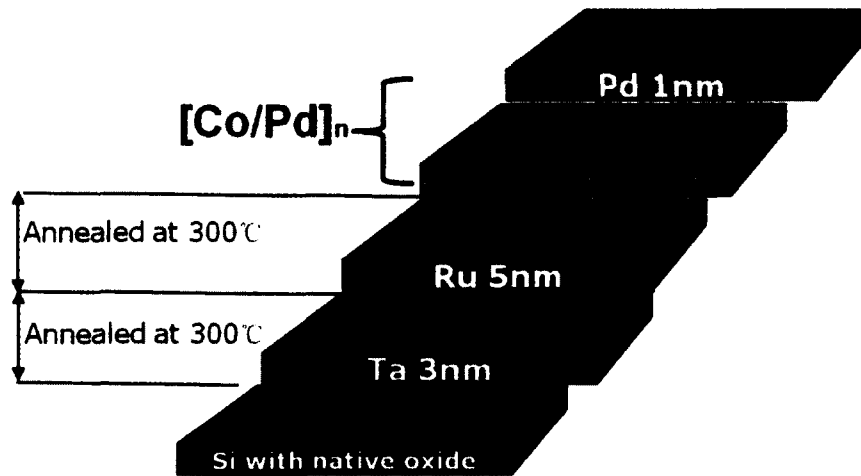


FIG. 7.1: Thin film structure of $[\text{Co/Pd}]_n$ multilayer on Ru 5 nm/Ta 3 nm buffer/seed layer.

7.1.1 Experiments and Methods

In this section, we discuss the experiment and methods used in this study.

In order to work with samples relevant to industrial applications, the thin films were deposited on non-pretreated Si wafers with natural oxide layers on the surface. The deposition method used was DC magnetron sputtering with Argon gas in a modified Perkin-Elmer MBE system with five sources. We carried out the entire film growth and annealing process *in-situ*. The base pressure was in the mid 10^{-10} Torr range. We also used RHEED to assess *in-situ* the crystalline structure/character of the surface.

A seed/buffer layer consisting of Ta(3nm)/Ru(5nm) was first deposited on commercial Si wafers with their native oxide layer as shown in Fig.7.1. In order to achieve atomically smooth interfaces, a systematic analysis of thermal treatment effects on the surface roughness of the seed layers after suitable post-annealing treatments enabled the optimization of the surface roughness up to 0.17 nm. Afterwards, $[\text{Co/Pd}]_n$ superlattice layers were grown by alternate deposition of Co and Pd.

The main surface characterization method was atomic force microscopy (AFM)

using a commercial Nanotec AFM and associated software. We utilized a Quantum Design MPMS SQUID instrument for magnetic characterization.

7.1.2 Results

Surface Roughness Analysis by Thermal Treatment of Buffer Layer

The root-mean-square (RMS) average roughness value is used to quantify the average surface roughness analyzing the surface morphology measurement by AFM.

Fig.7.2(a) shows AFM images of an ‘as grown’ Ta (3 nm) layer on a commercial Si wafer with its natural oxide layer. The growth was carried out at room temperature. Fig.7.2(b) shows another sample with the same Ta deposition temperature and thickness but after post-annealing treatment at 300°C for 30 minutes. Fig.7.2(c) shows the surface of a subsequently deposited Ru (5 nm) layer at room temperature on the top of structure described in Fig.7.2(b).

Ta 3 nm	
Before annealing	0.13 nm
After annealing	0.21 nm
Ru 5 nm	
Before annealing	0.52 nm
After annealing	0.17 nm

TABLE 7.1: RMS roughness analysis of buffer/seed layer Ru (5 nm)/Ta (3 nm)/Si.

Table.7.1 summarizes these results. The surface of the final Ru (5 nm) became smoother than the surface with non-annealing treatments. The annealing process at 300°C for 30 minutes created a better than atomically smooth surface for further growth of $[\text{Co/Pd}]_n$ multilayers. Thus, the optimization process, compatible with industrial processes, that was developed here led to a suitable surface for subsequent ultrathin layer deposition.

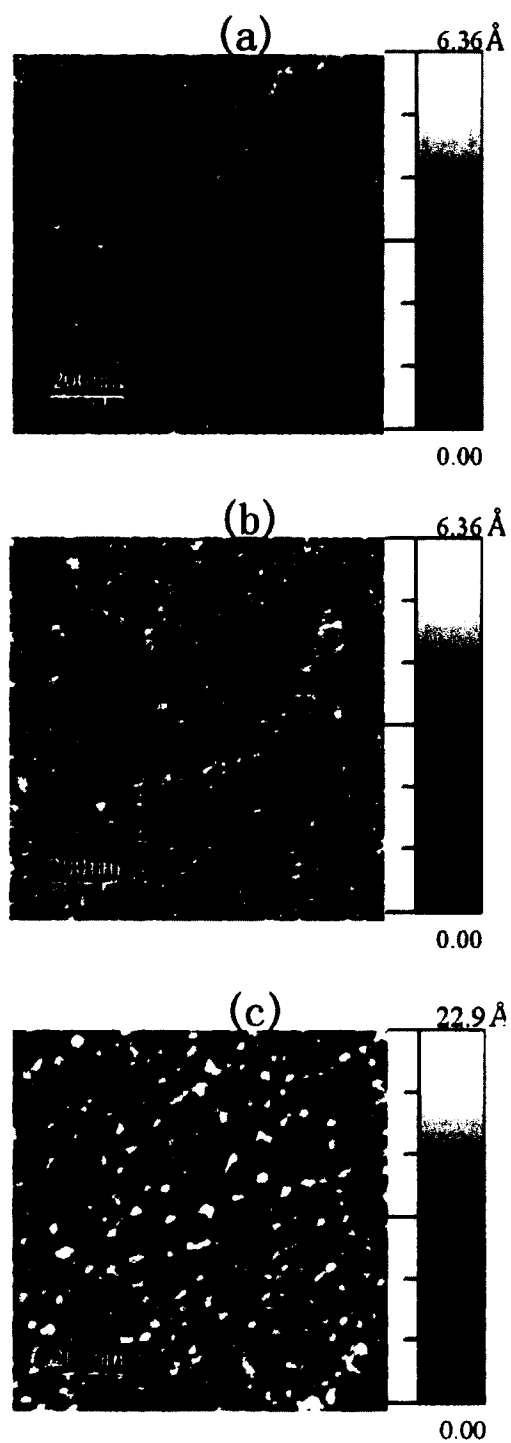


FIG. 7.2: AFM images of annealing treatment effects on the buffer layer: (a) Ta 3 nm on Si, (b) annealing Ta 3 nm at 300°C for 30 min, (c) Ru 5 nm on annealed Ta 3 nm.

In order to compare the effects of magnetic behavior in the artificial Co/Pd superlattices induced by interfacial roughness, we designed two types of $[\text{Co}/\text{Pd}]_n$ multilayers deposited on the optimized Ru/Ta buffer/seed layer based on RMS surface roughness analysis and optimization:

Type I: $[\text{Co (0.2 nm)}/\text{Pd (0.2 nm)}]_n$

Type II: $[\text{Co (0.4 nm)}/\text{Pd (0.4 nm)}]_n$

We note that the lattice constant is of bulk fcc Co 3.54\AA while the lattice constant of bulk fcc Pd is 3.89\AA [109], and the lattice constant of bulk $\text{Co}_{50}\text{Pd}_{50}$ is 3.81\AA [109], and the structure of the ideal (001) $[\text{Co}/\text{Pd}]_n$ multilayer is a stacking of (001) planes of an fcc lattice. The multilayer has tetragonal symmetry and of 1.71\AA between Co and Pd planes[110]. Thus, a nominal 0.2 nm thickness was selected so that it is just less than or very close to monoatomic layer thickness and a nominal 0.4 nm thickness is slightly larger than one monoatomic layer. All Co/Pd multilayers were deposited at room temperature and no further thermal treatment was carried out after deposition.

Number of bilayer (n)	RMS roughness (nm)
3	0.28
6	0.29
10	0.36
20	0.44

TABLE 7.2: RMS roughness analysis of $[\text{Co (0.2 nm)}/\text{Pd (0.2 nm)}]_n$

Table.7.2 summarizes the RMS roughness of 0.2 nm thick intervening Co and Pd layers with different repetition numbers. We noticed that the roughness deteriorates after increased number of Co/Pd bilayer repeats. Thus we notice that the surface roughness could achieve values comparable or larger than the single Co/Pd bilayers thickness (0.4 nm). The final surface roughness is very likely due to the accumulation

of interface deterioration after each Co/Pd bilayer. The RMS surface roughness exceeds the 0.2 nm nominal thickness of Co/Pd even after 3 bilayer repeats with the smallest repetition in this study. Hence, we strongly suspect that the interface roughness will dominate the structure of the entire stack with such ultrathin bilayers and, due to the interface roughness and associated defects, the individual Co and Pd layers may not form complete layers. To corroborate this statement we carried out magnetic hysteresis measurements.

Magnetic Hysteresis Measurements

Magnetic hysteresis measurements using a SQUID MPS magnetometer were conducted on both types of samples. Our instrument was recently upgraded with a horizontal sample rotator to enable accurate in-plane and perpendicular configurations for the applied magnetic field with respect to the plane of the sample surface. We conducted the magnetic hysteresis measurement at low temperature (20K) in order to reduce the thermal and electric noise. Because the total thickness (namely) of the ferromagnetic thin film was ~ 4 nm, the magnetic signal will be small and easily dominated by thermal/electrical noise. The magnetic signal is the statistical average of 20 measurements of the magnetic moment at each data point.

[Co (0.2 nm)/Pd (0.2 nm)]₂₀ Fig.7.3 shows representative loops with the applied magnetic field perpendicular and parallel to the plane of a sample obtained for the 20 bilayer repeats multilayer. It is worth noting here that the final surface roughness of this sample was ~ 0.4 nm. The magnetic hysteresis loop shows that the in-plane and out of plane both have similar saturation fields and very small coercivity (100 Oe) compared to those in previous studies (coercivity around 1000 Oe) with smoother interface and more repetition of bilayers. The shape of the in-plane and out of plane loops is also very similar. It is worth mentioning that magnetic

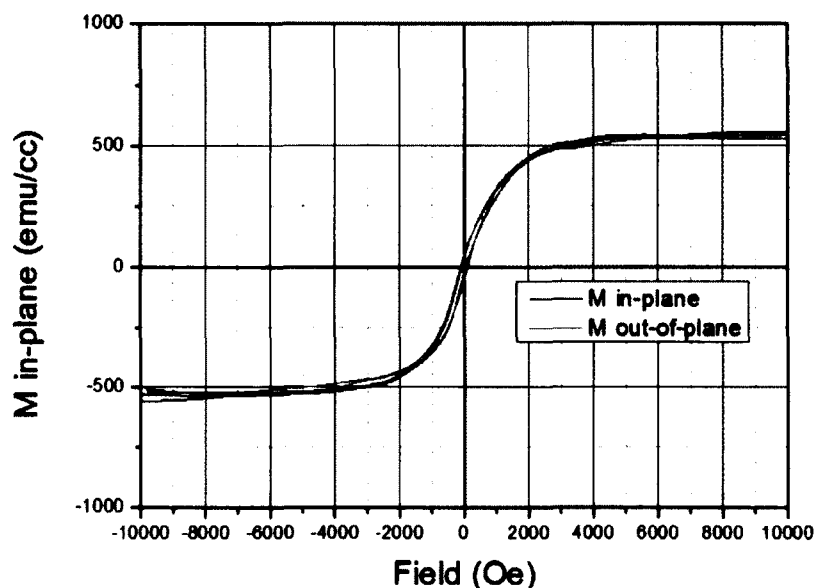


FIG. 7.3: Magnetic hysteresis measurement of $[\text{Co (0.2 nm)/Pd (0.2 nm)}]_{20}$ on Ru (5 nm) /Ta (3 nm)/Si sample with in-plane and out of plane configuration.

hysteresis loops with lower numbers of bilayer repeats (6 and 10) also had similar behavior compared to the 20 repeats multilayer but exhibited a higher noise level.

These magnetic loops indicate that there may not be complete magnetic layers in these multilayers, as expected since the surface roughness is larger than the nominal layer thickness. The level of intermixing in the $[\text{Co (0.2 nm)/Pd (0.2 nm)}]_n$ samples is so severe compared to the nominal layers thickness, that it can lead to formation of Co clusters instead of larger zones where magnetic domains can develop, hence the very low coercivity observed. Thus, we believe that the interfacial roughness hindered formations of complete Co layers as postulated earlier, and the magnetic behavior is not ferromagnetic but rather super-paramagnetic due to Co nano-clusters. We note here that the loops obtained for samples with fewer of repeats were very noisy and are therefore not shown in this dissertation.

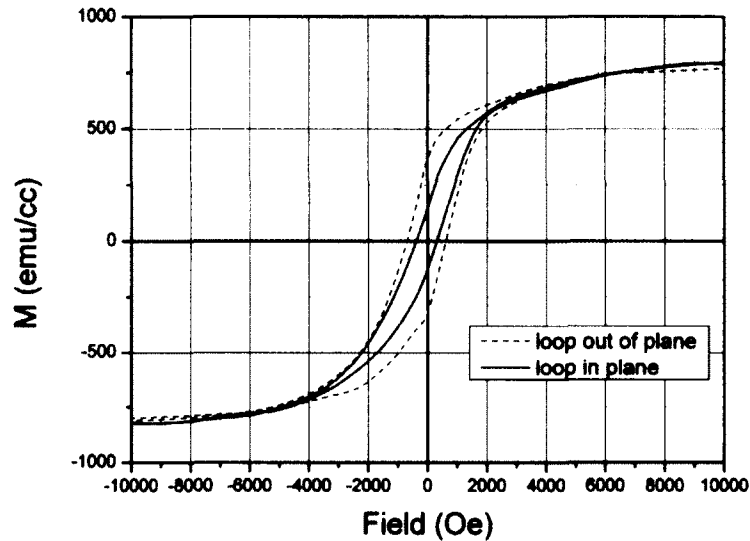


FIG. 7.4: Magnetic hysteresis measurement of $[\text{Co (0.4 nm)/Pd (0.4 nm)}]_{10}$ on Ru (5 nm) /Ta (3 nm)/Si sample with in-plane and out of plane configuration.

$[\text{Co (0.4 nm)/Pd (0.4 nm)}]_n$ On the other hand, for the $[\text{Co (0.4 nm)/Pd (0.4 nm)}]_n$ multilayers, intermixing may not be so significant[111] compared to the layer thickness, and formation of a complete ferromagnetic Co layer may be possible, thus leading to ferromagnetic behavior. Thus, we postulate that the 0.4 nm Co and Pd layers have adequate thickness to enable formation of effective monoatomic layers on average for the entire stack.

In Fig.7.4, hysteresis loops obtained with the field parallel and perpendicular to the plane of the sample are shown. It is worth noting that the total amount of ferromagnetic material (Co) is the same in the 0.2 nm sample shown in Fig.7.3 as in the 0.4 nm sample shown in Fig.4 enabling useful comparison regarding structural effects on the magnetic behavior.

The magnetic hysteresis loops in Fig.7.4 show clear ferromagnetic behavior. Also, the in-plane loop has a larger saturation field, and the perpendicular loop shows a larger coercive field as well as remanence, or remanent magnetization when

the applied field is zero. Hence, this sample has very weak but noticeable perpendicular magnetic anisotropy. This corroborates our initial guess about the dominant effect of the interface in ultrathin multiple Co/Pd layers on the overall magnetic behavior. A rough interface may not allow formation of complete and therefore ferromagnetically active layers due to intermixing of Co and Pd at the interface. However, if a thickness threshold for the individual layer thickness is achieved just above the intrinsic interfacial roughness, a complete ferromagnetic layer can be formed allowing formation of effective monoatomic thickness with the expected out-of-plane anisotropy.

7.1.3 Conclusion

The Ru/Ta seed layer surface roughness can be optimized by post-annealing treatments within suitable parameter ranges for STT-RAM industrial applications, leading to adequate surface roughness for subsequent multilayer growth. The layer thickness of the multilayers needs to be fine-tuned to overcome accumulated effective interfacial roughness. This is particularly important in order to obtain complete effective ferromagnetic monoatomic Co layers. We attempted such an approach for a [Co (0.4 nm)/Pd (0.4 nm)]₁₀ multilayer sample and achieved very weak but noticeable perpendicular magnetic anisotropy. Our studies are relevant for STT-RAM applications since industrial processes may pose constraints regarding thin film growth and processing parameters, which we attempted to follow in this study. Aspects of this work were part a collaboration with Grandis (now part of Samsung under a grant from DARPA).

CHAPTER 8

Conclusion

Investigations into the structure-property correlations in ferromagnetic thin films that exhibit surface plasmon excitations have been discussed in this dissertation. Experiments related to magnetic, optical, linear magneto-optical, non-linear magneto-optical and also magneto-transport properties were studied.

The sensitivity of conventional SPR sensors can be strongly enhanced by adding magnetic elements that give rise to magneto-optical signals. Tailored Au/Co/Au trilayer structures were shown to be able to achieve SPP modes that exhibit large electromagnetic fields due to surface plasmon excitation. The magneto-optical(MO) signal can be modulated by externally applied magnetic fields. The MO activity exhibits a strong dependence with the external magnetic fields. By using magneto-optics as a tool, we have analyzed the field-dependent optical response in tailored Au/Co/Au trilayers and have been able to probe the SPP generated electromagnetic fields within the structures, checking them against simulated values calculated using transfer matrix formalism.

In addition to tailoring the Au/Co/Au trilayer structure with precisely controlled thickness, it was also shown Au-Co nanocomposites as a easier preparation

mode with remarkable sensitivities. Au-Co segregation in nano-clusters and smooth surface, with SPP propagation enabled, exhibit largest MO effects. The MO activity also increases with increasing Co concentration consistent with the presence of more magnetic material in the films, while the angular resolution of the field-dependent change of the reflectivity at resonance is insensitive to the amount of Co present.

The composition of Au-Co nanocomposite thin films affects their non-linear magneto-optical properties as well as the magneto-transport behavior in a correlated manner. The interaction between magnetic clusters in granular films depending on the average distance between clusters affects the NOMOKE properties. Au-Co nanocomposites NOMOKE indicates when the onset of percolation occurs. Above percolation threshold, ferromagnetic ordering leads to a significant increase in the NOMOKE magnetic contrast but suppresses the spin-dependent electron scattering and also the magneto-resistance. The NOMOKE also suggests possible localized surface plasmon excitation leading to localized non-linear magneto-optical enhancements.

We have also investigated post-deposition processing treatments applied to magnetic multilayers for STT-MRAM applications to optimize their magnetic anisotropy properties. We studied the optimization of the layer thickness of the multilayers to overcome accumulated effective interfacial roughness, particularly important in order to obtain complete effective ferromagnetic monoatomic Co layers and we achieved very weak but noticeable perpendicular magnetic anisotropy.

BIBLIOGRAPHY

- [1] J. R. Skuza, Ph.D. thesis, The College of William and Mary (2011), thin Film and Chemical Ordering Effects on the Magnetic Anisotropy in Binary Alloys.
- [2] S. Hayashi and T. Okamoto, *Journal of Physics D: Applied Physics* **45**, 433001 (2012), URL <http://stacks.iop.org/0022-3727/45/i=43/a=433001>.
- [3] T. Murzina, T. Misuryaev, A. Nikulin, O. Aktsipetrov, and J. Gdde, *Journal of Magnetism and Magnetic Materials* **258259**, 99 (2003), ISSN 0304-8853, second Moscow International Symposium on Magnetism, URL <http://www.sciencedirect.com/science/article/pii/S0304885302010740>.
- [4] M. N. Baibich, J. M. Broto, A. Fert, F. N. Van Dau, F. Petroff, P. Etienne, G. Creuzet, A. Friederich, and J. Chazelas, *Phys. Rev. Lett.* **61**, 2472 (1988), URL <http://link.aps.org/doi/10.1103/PhysRevLett.61.2472>.
- [5] G. Binasch, P. Grünberg, F. Saurenbach, and W. Zinn, *Phys. Rev. B* **39**, 4828 (1989), URL <http://link.aps.org/doi/10.1103/PhysRevB.39.4828>.
- [6] U. Hartmann and R. Coehoorn, *Magnetic Multilayers and Giant Magnetoresistance: Fundamentals and Industrial Applications*, Springer Series in Surface Sciences (Springer, 2000), ISBN 9783540655688.
- [7] T. Valet and A. Fert, *Phys. Rev. B* **48**, 7099 (1993), URL <http://link.aps.org/doi/10.1103/PhysRevB.48.7099>.
- [8] T. Valet and A. Fert, *Journal of Magnetism and Magnetic Materials* **121**, 378 (1993), ISSN 0304-8853, proceedings of the International

Symposium on Magnetic Ultrathin Films, Multilayers and Surfaces, URL <http://www.sciencedirect.com/science/article/pii/S030488539391225V>.

- [9] C. Chappert, A. Fert, and F. N. Van Dau, *Nat Mater* **6**, 813 (2007), ISSN 1476-1122, 10.1038/nmat2024, URL <http://dx.doi.org/10.1038/nmat2024>.
- [10] J. Katine and E. E. Fullerton, *Journal of Magnetism and Magnetic Materials* **320**, 1217 (2008), ISSN 0304-8853, URL <http://www.sciencedirect.com/science/article/pii/S0304885307010189>.
- [11] M. Julliere, *Physics Letters A* **54**, 225 (1975), ISSN 0375-9601, URL <http://www.sciencedirect.com/science/article/pii/0375960175901747>.
- [12] T. Miyazaki and N. Tezuka, *Journal of Magnetism and Magnetic Materials* **139**, L231 (1995), ISSN 0304-8853, URL <http://www.sciencedirect.com/science/article/pii/S0304885395900012>.
- [13] J. S. Moodera, L. R. Kinder, T. M. Wong, and R. Meservey, *Phys. Rev. Lett.* **74**, 3273 (1995), URL <http://link.aps.org/doi/10.1103/PhysRevLett.74.3273>.
- [14] W. H. Butler, X.-G. Zhang, T. C. Schulthess, and J. M. MacLaren, *Phys. Rev. B* **63**, 054416 (2001), URL <http://link.aps.org/doi/10.1103/PhysRevB.63.054416>.
- [15] J. Mathon and A. Umerski, *Phys. Rev. B* **63**, 220403 (2001), URL <http://link.aps.org/doi/10.1103/PhysRevB.63.220403>.
- [16] M. Bowen, V. Cros, F. Petroff, A. Fert, C. Martinez Boubeta, J. L. Costa-Kramer, J. V. Anguita, A. Cebollada, F. Briones, J. M. de Teresa, et al., *Applied Physics Letters* **79** (2001).

- [17] S. Yuasa, T. Nagahama, A. Fukushima, Y. Suzuki, and K. Ando, *Nat Mater* **3**, 868 (2004), ISSN 1476-1122, 10.1038/nmat1257, URL <http://dx.doi.org/10.1038/nmat1257>.
- [18] S. S. P. Parkin, C. Kaiser, A. Panchula, P. M. Rice, B. Hughes, M. Samant, and S.-H. Yang, *Nat Mater* **3**, 862 (2004), ISSN 1476-1122, 10.1038/nmat1256, URL <http://dx.doi.org/10.1038/nmat1256>.
- [19] D. D. Djayaprawira, K. Tsunekawa, M. Nagai, H. Maehara, S. Yamagata, N. Watanabe, S. Yuasa, Y. Suzuki, and K. Ando, *Applied Physics Letters* **86** (2005).
- [20] S. Ikeda, K. Miura, H. Yamamoto, K. Mizunuma, H. D. Gan, M. Endo, S. Kanai, J. Hayakawa, F. Matsukura, and H. Ohno, *Nat Mater* **9**, 721 (2010), ISSN 1476-1122, 10.1038/nmat2804, URL <http://dx.doi.org/10.1038/nmat2804>.
- [21] D. C. Worledge, G. Hu, D. W. Abraham, J. Z. Sun, P. L. Trouiloud, J. Nowak, S. Brown, M. C. Gaidis, E. J. OSullivan, and R. P. Robertazzi, *Applied Physics Letters* **98**, 022501 (2011), URL <http://scitation.aip.org/content/aip/journal/apl/98/2/10.1063/1.3536482>.
- [22] P. M. Tedrow and R. Meservey, *Phys. Rev. B* **7**, 318 (1973), URL <http://link.aps.org/doi/10.1103/PhysRevB.7.318>.
- [23] J. Kerr, *Philosophical Magazine* **3**, 321 (1877).
- [24] Z. Q. Qiu and S. D. Bader, *Review of Scientific Instruments* **71** (2000).
- [25] J. Zak, E. Moog, C. Liu, and S. Bader, *Journal of Magnetism and Magnetic Materials* **89**, 107 (1990), ISSN 0304-8853, URL <http://www.sciencedirect.com/science/article/pii/030488539090713Z>.

- [26] J. Zak, E. R. Moog, C. Liu, and S. D. Bader, *Phys. Rev. B* **43**, 6423 (1991), URL <http://link.aps.org/doi/10.1103/PhysRevB.43.6423>.
- [27] S. Maier, *Plasmonics: Fundamentals and Applications: Fundamentals and Applications* (Springer, 2007), ISBN 9780387378251.
- [28] H. Raether, in *Surface Plasmons on Smooth and Rough Surfaces and on Gratings* (Springer Berlin Heidelberg, 1988), vol. 111 of *Springer Tracts in Modern Physics*, pp. 4–39, ISBN 978-3-540-17363-2, URL <http://dx.doi.org/10.1007/BFb0048319>.
- [29] A. D. Boardman, ed., *Electromagnetic Surface Modes* (Wiley, Chichester, ???).
- [30] U. Kreibig and M. Vollmer, *Optical properties of metal clusters*, no. v. 25 in Springer series in materials science (Springer, 1995), ISBN 9780387578361.
- [31] L. Novotny and B. Hecht, *Principles of Nano-Optics* (Cambridge University Press, 2006), ISBN 9781139452052.
- [32] K. A. Willets and R. P. Van Duyne, *Annual Review of Physical Chemistry* **58**, 267 (2007), pMID: 17067281, <http://www.annualreviews.org/doi/pdf/10.1146/annurev.physchem.58.032806.10460>
URL <http://www.annualreviews.org/doi/abs/10.1146/annurev.physchem.58.032806.1>
- [33] I. Pockrand, *Journal of Physics D: Applied Physics* **9**, 2423 (1976), URL <http://stacks.iop.org/0022-3727/9/i=17/a=003>.
- [34] M. Hutley and D. Maystre, *Optics Communications* **19**, 431 (1976), ISSN 0030-4018, URL <http://www.sciencedirect.com/science/article/pii/0030401876901164>.

- [35] J. Homola, S. S. Yee, and G. Gauglitz, *Sensors and Actuators B: Chemical* **54**, 3 (1999), ISSN 0925-4005, URL <http://www.sciencedirect.com/science/article/pii/S0925400598003219>.
- [36] M. Schubert, *Phys. Rev. B* **53**, 4265 (1996), URL <http://link.aps.org/doi/10.1103/PhysRevB.53.4265>.
- [37] M. Ohring, *Materials Science of Thin Films* (Elsevier Science, 2001), ISBN 9780080491783.
- [38] T. Nikolajsen, K. Leosson, and S. I. Bozhevolnyi, *Applied Physics Letters* **85** (2004).
- [39] W. L. Barnes, A. Dereux, and T. W. Ebbesen, *Nature* **424**, 824 (2003), ISSN 0028-0836, 10.1038/nature01937, URL <http://dx.doi.org/10.1038/nature01937>.
- [40] Y. M. Strelniker and D. J. Bergman, *Phys. Rev. B* **59**, R12763 (1999), URL <http://link.aps.org/doi/10.1103/PhysRevB.59.R12763>.
- [41] G. A. Wurtz, W. Hendren, R. Pollard, R. Atkinson, L. L. Guyader, A. Kirilyuk, T. Rasing, I. I. Smolyaninov, and A. V. Zayats, *New Journal of Physics* **10**, 105012 (2008), URL <http://stacks.iop.org/1367-2630/10/i=10/a=105012>.
- [42] Y.-C. Lan, Y.-C. Chang, and P.-H. Lee, *Applied Physics Letters* **90**, 171114 (2007), URL <http://scitation.aip.org/content/aip/journal/apl/90/17/10.1063/1.2732827>.
- [43] K. Chau, S. Irvine, and A. Elezzabi, *Quantum Electronics, IEEE Journal of* **40**, 571 (2004), ISSN 0018-9197.

- [44] J. B. Khurgin, *Applied Physics Letters* **89**, 251115 (2006), URL <http://scitation.aip.org/content/aip/journal/apl/89/25/10.1063/1.2422885>.
- [45] B. Sepulveda, A. Calle, L. Lechuga, and G. Armelles, *OPTICS LETTERS* **31**, 1085 (2006), ISSN 0146-9592.
- [46] M. S. Kushwaha and P. Halevi, *Phys. Rev. B* **36**, 5960 (1987), URL <http://link.aps.org/doi/10.1103/PhysRevB.36.5960>.
- [47] P. Ferguson, O. Stafsudd, and R. Wallis, *Physica B+C* **89**, 91 (1977), ISSN 0378-4363, URL <http://www.sciencedirect.com/science/article/pii/0378436377900596>.
- [48] R. K. Hickernell and D. Sarid, *Opt. Lett.* **12**, 570 (1987), URL <http://ol.osa.org/abstract.cfm?URI=ol-12-8-570>.
- [49] J. J. Burke, G. I. Stegeman, and T. Tamir, *Phys. Rev. B* **33**, 5186 (1986), URL <http://link.aps.org/doi/10.1103/PhysRevB.33.5186>.
- [50] R. Zia, M. D. Selker, and M. L. Brongersma, *Phys. Rev. B* **71**, 165431 (2005), URL <http://link.aps.org/doi/10.1103/PhysRevB.71.165431>.
- [51] C. Hermann, V. A. Kosobukin, G. Lampel, J. Peretti, V. I. Safarov, and P. Bertrand, *Phys. Rev. B* **64**, 235422 (2001), URL <http://link.aps.org/doi/10.1103/PhysRevB.64.235422>.
- [52] J. B. Gonzalez-Diaz, A. Garcia-Martin, G. Armelles, J. M. Garcia-Martin, C. Clavero, A. Cebollada, R. A. Lukaszew, J. R. Skuza, D. P. Kumah, and R. Clarke, *Phys. Rev. B* **76**, 153402 (2007), URL <http://link.aps.org/doi/10.1103/PhysRevB.76.153402>.

- [53] V. I. Safarov, V. A. Kosobukin, C. Hermann, G. Lampel, J. Peretti, and C. Marlière, *Phys. Rev. Lett.* **73**, 3584 (1994), URL <http://link.aps.org/doi/10.1103/PhysRevLett.73.3584>.
- [54] N. Bonod, R. Reinisch, E. Popov, and M. Nevière, *J. Opt. Soc. Am. B* **21**, 791 (2004), URL <http://josab.osa.org/abstract.cfm?URI=josab-21-4-791>.
- [55] M. Schubert, T. E. Tiwald, and J. A. Woollam, *Appl. Opt.* **38**, 177 (1999), URL <http://ao.osa.org/abstract.cfm?URI=ao-38-1-177>.
- [56] E. D. Palik, *Handbook of optical constants of solids* (Academic Press, Orlando, 1985), ISBN 0125444206 9780125444200.
- [57] D. P. Kumah, A. Cebollada, C. Clavero, J. M. Garca-Martn, J. R. Skuza, R. A. Lukaszew, and R. Clarke, *Journal of Physics D: Applied Physics* **40**, 2699 (2007), URL <http://stacks.iop.org/0022-3727/40/i=9/a=003>.
- [58] S. Park, X. Zhang, A. Misra, J. D. Thompson, M. R. Fitzsimmons, S. Lee, and C. M. Falco, *Applied Physics Letters* **86**, 042504 (2005), URL <http://scitation.aip.org/content/aip/journal/apl/86/4/10.1063/1.1850592>.
- [59] D. Weller, J. Stöhr, R. Nakajima, A. Carl, M. G. Samant, C. Chappert, R. Mégy, P. Beauvillain, P. Veillet, and G. A. Held, *Phys. Rev. Lett.* **75**, 3752 (1995), URL <http://link.aps.org/doi/10.1103/PhysRevLett.75.3752>.
- [60] T. Koide, H. Miyauchi, J. Okamoto, T. Shidara, A. Fujimori, H. Fukutani, K. Amemiya, H. Takeshita, S. Yuasa, T. Katayama, et al., *Phys. Rev. Lett.* **87**, 257201 (2001), URL <http://link.aps.org/doi/10.1103/PhysRevLett.87.257201>.
- [61] P. Bertrand, C. Hermann, G. Lampel, J. Peretti, and

- V. I. Safarov, Phys. Rev. B **64**, 235421 (2001), URL <http://link.aps.org/doi/10.1103/PhysRevB.64.235421>.
- [62] N. Richard, A. Dereux, T. David, E. Bourillot, J. P. Goudonnet, F. Scheurer, E. Beaurepaire, and G. Garreau, Phys. Rev. B **59**, 5936 (1999), URL <http://link.aps.org/doi/10.1103/PhysRevB.59.5936>.
- [63] S. Mader, *The use of thin films in physical investigations: a NATO Advanced Study Institute held at the Imperial College of Science and Technology, University of London, 19-24 July, 1965* (Academic Press, 1966).
- [64] T. Choy, *Effective Medium Theory: Principles and Applications*, International series of monographs on physics (Clarendon Press, 1999), ISBN 9780198518921.
- [65] R. Egerton, *Electron Energy-Loss Spectroscopy in the Electron Microscope*, Language of science (Plenum Press, 1996), ISBN 9780306452239.
- [66] N. D. Browning, M. F. Chisholm, and S. J. Pennycook, Nature **444**, 235 (2006), ISSN 0028-0836, 10.1038/nature05262, URL <http://dx.doi.org/10.1038/nature05262>.
- [67] M. Varela, A. Lupini, K. v. Benthem, A. Borisevich, M. Chisholm, N. Shibata, E. Abe, and S. Pennycook, Annual Review of Materials Research **35**, 539 (2005), <http://www.annualreviews.org/doi/pdf/10.1146/annurev.matsci.35.102103.090513>, URL <http://www.annualreviews.org/doi/abs/10.1146/annurev.matsci.35.102103.090513>.
- [68] S. C. Simon, B. Schmaltz, A. Rouhanipour, H. J. Rder, and K. Millen, Advanced Materials **21**, 83 (2009), ISSN 1521-4095, URL <http://dx.doi.org/10.1002/adma.200802019>.

- [69] M. Bosman, M. Watanabe, D. Alexander, and V. Keast, *Ultramicroscopy* **106**, 1024 (2006), ISSN 0304-3991, proceedings of the International Workshop on Enhanced Data Generated by Electrons Proceedings of the International Workshop on Enhanced Data Generated by Electrons, URL <http://www.sciencedirect.com/science/article/pii/S0304399106001021>.
- [70] E. Kretschmann, *Zeitschrift fr Physik* **241**, 313 (1971), ISSN 0044-3328, URL <http://dx.doi.org/10.1007/BF01395428>.
- [71] C. Clavero, A. Cebollada, G. Armelles, Y. Huttel, J. Arbiol, F. Peiró, and A. Cornet, *Phys. Rev. B* **72**, 024441 (2005), URL <http://link.aps.org/doi/10.1103/PhysRevB.72.024441>.
- [72] A. Wokaun, J. G. Bergman, J. P. Heritage, A. M. Glass, P. F. Liao, and D. H. Olson, *Phys. Rev. B* **24**, 849 (1981), URL <http://link.aps.org/doi/10.1103/PhysRevB.24.849>.
- [73] V. K. Valev, A. V. Silhanek, W. Gillijns, Y. Jeyaram, H. Paddubrouskaya, A. Volodin, C. G. Biris, N. C. Panoiu, B. De Clercq, M. Ameloot, et al., *ACS NANO* **5**, 91 (2011), ISSN 1936-0851.
- [74] C. Clavero, K. Yang, J. R. Skuza, and R. A. Lukaszew, *OPTICS EXPRESS* **18**, 7743 (2010), ISSN 1094-4087.
- [75] L. Wang, C. Clavero, Z. Huba, K. J. Carroll, E. E. Carpenter, D. Gu, and R. A. Lukaszew, *NANO LETTERS* **11**, 1237 (2011), ISSN 1530-6984.
- [76] P. K. Jain, Y. Xiao, R. Walsworth, and A. E. Cohen, *NANO LETTERS* **9**, 1644 (2009), ISSN 1530-6984.
- [77] G. Ctistis, E. Papaioannou, P. Patoka, J. Gutek, P. Fumagalli, and M. Giersig, *NANO LETTERS* **9**, 1 (2009), ISSN 1530-6984.

- [78] V. Skumryev, S. Stoyanov, Y. Zhang, G. Hadjipanayis, D. Givord, and J. Nogues, *Nature* **423**, 850 (2003), ISSN 0028-0836, 10.1038/nature01687, URL <http://dx.doi.org/10.1038/nature01687>.
- [79] J. Reif, C. Rau, and E. Matthias, *Phys. Rev. Lett.* **71**, 1931 (1993), URL <http://link.aps.org/doi/10.1103/PhysRevLett.71.1931>.
- [80] O. A. Aktsipetrov, O. V. Braginski, and D. A. Esikov, *Soviet Journal of Quantum Electronics* **20**, 259 (1990), URL <http://stacks.iop.org/0049-1748/20/i=3/a=A16>.
- [81] T. V. Murzina, E. A. Ganshina, S. V. Guschin, T. V. Misuryaev, and O. A. Aktsipetrov, *Applied Physics Letters* **73** (1998).
- [82] T. Murzina, T. Misuryaev, A. Kravets, J. Gdde, D. Schuhmacher, G. Marowsky, A. Nikulin, and O. Aktsipetrov, *Surface Science* **482485**, Part 2, 1101 (2001), ISSN 0039-6028, URL <http://www.sciencedirect.com/science/article/pii/S0039602801010226>.
- [83] H. Okamoto, T. B. Massalski, and A. International, *Phase diagrams of binary gold alloys*, Monograph series on alloy phase diagrams (ASM International, 1987), ISBN 9780871702494.
- [84] K. Yang, C. Clavero, J. R. Skuza, M. Varela, and R. A. Lukaszew, *Journal of Applied Physics* **107**, 103924 (2010), URL <http://scitation.aip.org/content/aip/journal/jap/107/10/10.1063/1.3428470>.
- [85] J. Q. Xiao, J. S. Jiang, and C. L. Chien, *Phys. Rev. Lett.* **68**, 3749 (1992), URL <http://link.aps.org/doi/10.1103/PhysRevLett.68.3749>.
- [86] M. Pan, H. Liu, J. Wang, J. Jia, Q. Xue, J. Li, S. Qin, U. Mirsaidov, X. Wang, J. Markert, et al., *NANO LETTERS* **5**, 87 (2005), ISSN 1530-6984.

- [87] C. L. S. Rizal, A. Yamada, Y. Hori, S. Ishida, M. Matsuda, and Y. Ueda, *physica status solidi (c)* **1**, 1756 (2004), ISSN 1610-1642, URL <http://dx.doi.org/10.1002/pssc.200304415>.
- [88] Y. U. Conrad Rizal and R. K. Pokharel, *International Journal of Applied Physics and Mathematics* **1**, 161 (2011).
- [89] J.-i. Inoue, A. Oguri, and S. Maekawa, *Journal of the Physical Society of Japan* **60**, 376 (1991), <http://journals.jps.jp/doi/pdf/10.1143/JPSJ.60.376>, URL <http://journals.jps.jp/doi/abs/10.1143/JPSJ.60.376>.
- [90] R. F. Soohoo, *Magnetic Thin Films* (Harper and Row, New York, 1965).
- [91] R. Bozorth, *Ferromagnetism*, An IEEE Press Classic Reissue (Wiley, 1993), ISBN 9780780310322.
- [92] V. K. Valev, A. Kirilyuk, F. Dalla Longa, J. T. Kohlhepp, B. Koopmans, and T. Rasing, *Phys. Rev. B* **75**, 012401 (2007), URL <http://link.aps.org/doi/10.1103/PhysRevB.75.012401>.
- [93] G. Tessier, C. Malouin, P. Georges, A. Brun, D. Renard, V. Pavlov, P. Meyer, J. Ferr, and P. Beauvillain, *Applied Physics B* **68**, 545 (1999), ISSN 0946-2171, URL <http://dx.doi.org/10.1007/s003400050663>.
- [94] V. V. Pavlov, G. Tessier, C. Malouin, P. Georges, A. Brun, D. Renard, P. Meyer, J. Ferr, and P. Beauvillain, *Applied Physics Letters* **75** (1999).
- [95] D. M. Newman, M. L. Wears, R. J. Matelon, and I. R. Hooper, *Journal of Physics: Condensed Matter* **20**, 345230 (2008), URL <http://stacks.iop.org/0953-8984/20/i=34/a=345230>.

- [96] O. A. Aktsipetrov, T. V. Murzina, E. M. Kim, R. V. Kapra, A. A. Fedyanin, M. Inoue, A. F. Kravets, S. V. Kuznetsova, M. V. Ivanchenko, and V. G. Lifshits, *J. Opt. Soc. Am. B* **22**, 138 (2005), URL <http://josab.osa.org/abstract.cfm?URI=josab-22-1-138>.
- [97] X. Wang, K. ping Chen, M. Zhao, and D. D. Nolte, *Opt. Express* **18**, 24859 (2010), URL <http://www.opticsexpress.org/abstract.cfm?URI=oe-18-24-24859>.
- [98] Y. G. Pogorelov, M. M. P. d. Azevedo, and J. B. Sousa, *Phys. Rev. B* **58**, 425 (1998), URL <http://link.aps.org/doi/10.1103/PhysRevB.58.425>.
- [99] H. J. G. Draaisma and W. J. M. de Jonge, *Journal of Applied Physics* **62** (1987).
- [100] L.-X. Ye, C.-M. Lee, J.-W. Syu, Y.-R. Wang, K.-W. Lin, Y.-H. Chang, and T.-h. Wu, *IEEE TRANSACTIONS ON MAGNETICS* **44**, 3601 (2008), ISSN 0018-9464, international Magnetism Conference (Intermag), Madrid, SPAIN, MAY 04-08, 2008.
- [101] F. J. A. den Broeder, D. Kuiper, A. P. van de Mosse-laer, and W. Hoving, *Phys. Rev. Lett.* **60**, 2769 (1988), URL <http://link.aps.org/doi/10.1103/PhysRevLett.60.2769>.
- [102] K. Mizunuma, S. Ikeda, J. H. Park, H. Yamamoto, H. Gan, K. Miura, H. Hasegawa, J. Hayakawa, F. Matsukura, and H. Ohno, *Applied Physics Letters* **95**, 232516 (2009), URL <http://scitation.aip.org/content/aip/journal/apl/95/23/10.1063/1.3265740>.
- [103] S. Mangin, D. Ravelosona, J. A. Katine, M. J. Carey, B. D. Terris, and E. E.

- Fullerton, *Nat Mater* **5**, 210 (2006), ISSN 1476-1122, 10.1038/nmat1595, URL <http://dx.doi.org/10.1038/nmat1595>.
- [104] H. Meng and J.-P. Wang, *Applied Physics Letters* **88**, 172506 (2006), URL <http://scitation.aip.org/content/aip/journal/apl/88/17/10.1063/1.2198797>.
- [105] J. Slonczewski, *Journal of Magnetism and Magnetic Materials* **159**, L1 (1996), ISSN 0304-8853, URL <http://www.sciencedirect.com/science/article/pii/0304885396000625>.
- [106] M. O. (), S. O. (), F. K. (), and M. F. (), *Journal of Applied Physics* **111**, 07 (2012).
- [107] K. Yakushiji, T. Saruya, H. Kubota, A. Fukushima, T. Nagahama, S. Yuasa, and K. Ando, *Applied Physics Letters* **97**, 232508 (2010), URL <http://scitation.aip.org/content/aip/journal/apl/97/23/10.1063/1.3524230>.
- [108] J. R. Skuza, C. Clavero, K. Yang, B. Wincheski, and R. A. Lukaszew, *IEEE TRANSACTIONS ON MAGNETICS* **46**, 1886 (2010), ISSN 0018-9464.
- [109] R. H. Victora and J. M. MacLaren, *Journal of Applied Physics* **69** (1991).
- [110] J. Bland and B. Heinrich, *Ultrathin Magnetic Structures I: An Introduction to the Electronic, Magnetic and Structural Properties*, *Ultrathin Magnetic Structures* (Springer, 2005), ISBN 9783540219552.
- [111] A. Zarefy, L. Lechevallier, R. Lard, H. Chiron, J.-M. L. Breton, V. Baltz, B. Rodmacq, and B. Dieny, *Journal of Physics D: Applied Physics* **43**, 215004 (2010), URL <http://stacks.iop.org/0022-3727/43/i=21/a=215004>.

VITA

Kaida Yang

Kaida Yang was born in Shanghai, China on November 18, 1984. He went to Fudan University and got his bachelor's degree in 2007. After graduation, she continued his study in the Department of Applied Science in the College of William and Mary, and got his master's degree in 2010. Currently he is a PhD graduate student, pursuing his PhD degree in the Department of Applied Science.

Journal Publications

1. **K. Yang**, V. Kryutyanskiy, I. Kolmychek, T. V. Murzina, and R. A. Lukaszew “Au-Co nanocomposite films: non-linear SHG magnetoplasmonics and magneto-transport studies”, 2013. Submitted.
2. **K. Yang**, Z. Li, A. Lukaszew, “Film Roughness Analysis and Magnetic Properties in Ultrathin Co/Pd Multilayers ”, *Journal of the Magnetism Society of Japan* Vol. 37 (2013) No. 3-2 SELECTED PAPERS FROM ICAUMS 2012 p. 190-193.
3. L. Wang, C. Clavero, **K. Yang**, E. Radue, M. T. Simons, I. Novikova, and R. A. Lukaszew, “Bulk and surface plasmon polariton excitation in RuO₂ for low-loss plasmonic applications in NIR”, *Optics Express* **20** 2 8618-8628 (2012).
4. C. Clavero, **K. Yang**, J. R. Skuza and R. A. Lukaszew, “Magnetic field modification of Surface Plasmon Polaritons on gratings”, *Optics Letters* **35**, 1557 (2010).
5. J. R. Skuza, C. Clavero, **K. Yang**, B. Wincheski, and R. A. Lukaszew, “Microstructural, magnetic anisotropy, and magnetic domain structure correlations in epitaxial FePd thin films with perpendicular magnetic anisotropy”, *IEEE Trans. Magnetism* **46**, 1886 (2010).
6. **K. Yang**, C. Clavero, J. R. Skuza, M. Varela and R. A. Lukaszew, “Surface plasmon resonance and magneto-optical enhancement on Au-Co nanocomposite thin films”, *Journal of Applied Physics* **107**, 103924 (2010).

7. L. Wang, **K. Yang**, C. Clavero, A. J. Nelson, K. J. Carroll, E. E. Carpenter, and R. A. Lukaszew, "Localized Surface Plasmon Resonance enhanced magneto-optical activity in core-shell Ag-Fe nanoparticles", *Journal of Applied Physics* **107**, 09B303 (2010)

8. C. Clavero, **K. Yang**, J. R. Skuza, and R. A. Lukaszew, "Magnetic field modification of intense Surface Plasmon Polaritons", *Optics Express* **18**, 7743 (2010).

Awards

1. The **Leo Falicov Student Award** for best presentation of graduate research in Magnetic Interfaces and Nanostructures Division of American Vacuum Society, 2013.
2. **AVS Dorothy M. and Earl S. Hoffman Travel Grant**, 2013.
3. **Awarded Student Poster Competition** AVS Mid-Atlantic Chapter Regional Meeting at NIST, Gaithersburg, MD (May 2013).

Selected Meetings Presentations/Participations

- (Talk) **K. Yang**, V. Kryutyanskiy, I Kolmychek, T. V. Murzina, and R. A. Lukaszew, “Non-Linear Magnetic SHG and Magneto-Transport in Au-Co Nanocomposite Thin Films”, 58th Magnetism and Magnetic Materials Conference, Denver, CO (Nov 2013).
- (Talk) **K. Yang**, V. Kryutyanskiy, I Kolmychek, T. V. Murzina, and R. A. Lukaszew, “Nanocluster Size Effects in Au-Co Nanocomposite Thin Films: Correlated Non-Linear Magneto-Optics and Magneto-Transport Studies”, AVS 60th International Symposium and Exhibition, Long Beach, CA (Oct 2013).
- (Poster Award Winner) **K. Yang**, V. Kryutyanskiy, I Kolmychek, T. V. Murzina, and R. A. Lukaszew, “Non-Linear Magnetic SHG and Magneto-Transport Study of Au-Co Nanocomposite Films”, AVS Mid-Atlantic Chapter Regional Meeting at NIST, Gaithersburg, MD (May 2013).
- (Poster) **K. Yang**, V. Kryutyanskiy, I Kolmychek, T. V. Murzina, and R. A. Lukaszew, “Au-Co Nanocomposite Films: Non-Linear SHG Magnetoplasmonics and Magneto-Transport Studies”, AVS Mid-Atlantic Chapter Regional Meeting in Newport News, VA (April 2013).
- (Talk) **K. Yang**, T. Murzina and R. A. Lukaszew “Nanocluster Effects on Magneto-Resistance and Optical Second-Harmonic Generation in Au-Co Composite Films”, APS March Meeting 2013, Baltimore, MD (March 18-22, 2013).
- (Talk) **K. Yang**, Z. Li and R. A. Lukaszew, “Surface and Interface Roughness Analysis of Ultrathin Co/Pd Multilayer for Magnetic Tunnel Junctions”, International Conference of the Asian Union of Magnetic Societies (ICAUMS 2012), Nara, Japan (October 2-5, 2012).

- (Poster) **K. Yang**, C. Clavero, J. Skuza, M. Varela and R. A. Lukaszew, “Enhancement of the Magneto-Optical Activity via Surface Plasmon Resonance on Au-Co Nanocomposite Thin Films”, AVS Mid-Atlantic Chapter Regional Meeting in Newport News, VA (April 2012).
- (Talk) **K. Yang**, C. Clavero, J. Skuza and A. Lukaszew, “Magneto-plasmonics and magneto-transport in Au-Co nanocomposite film”, 56th Magnetism and Magnetic Materials Conference, Scottsdale, AZ (October 30-Nov. 3, 2011).
- (Poster) **K. Yang**, C. Clavero, J. Skuza, M. Varela and R. A. Lukaszew, “Enhancement of the Magneto-Optical Activity via Surface Plasmon Resonance on Au-Co Nanocomposite Thin Films”, AVS Mid-Atlantic Chapter Regional Meeting in Gaithersburg, MD (October 2011).
- (Talk) **K. Yang**, Csar Clavero, Jonathan Skuza and R. A. Lukaszew, “Enhancement of the magneto-optical activity via surface plasmon resonance on Au-Co nanocomposite thin films”, TechConnect World Conference and Expo 2011, Hynes Convention Center, Boston, MA (June 13-16, 2011).
- (Poster) **K. Yang**, C. Clavero, J. Skuza, M. Varela and R. A. Lukaszew, “Enhancement of the Magneto-Optical Activity via Surface Plasmon Resonance on Au-Co Nanocomposite Thin Films”, AVS Mid-Atlantic Chapter Regional Meeting in Newport News, VA (April 2011).
- (Poster) **K. Yang**, C. Clavero, J. Skuza and R. A. Lukaszew, “Enhancement of the Magneto-Optical Activity via Surface Plasmon Resonance on Au-Co Nanocomposite Thin Film”, North Carolina Nanotechnology Commercialization Conference, UNC Charlotte, NC (March 2011).
- (Talk) **K. Yang**, L. Wang, C. Clavero, K. Carroll, E. Carpenter and R.A. Lukaszew, “Surface plasmon resonance enhanced magneto-optical activity in

core-shell Ag-Fe nanoparticles”,. 11th Joint MMM-Intermag conference, Washington DC (January 2010).

- (Talk) **K. Yang**, C. Clavero, J. Skuza, R. A. Lukaszew, “Enhancement of the magneto-optical activity in thin films via surface Plasmon resonance excitation”, The 76th Annual Meeting of the Southeastern Section of the American Physical Society (SESAPS), Atlanta, GA (Nov 11-14, 2009)